DEVELOPMENT OF HIGH-BRIGHTNESS ELECTRON SOURCES FOR FREE-ELECTRON LASERS

By

Jonathan D. Jarvis

Dissertation

Submitted to the Faculty of the

Graduate School of Vanderbilt University

in partial fulfillment of the requirements

for the degree of

DOCTOR OF PHILOSOPHY

in

Physics

May, 2009

Nashville, Tennessee

Approved:

Charles A. Brau

Jimmy L. Davidson

William E. Gabella

M. Shane Hutson

Norman H. Tolk

To Hillary Ann, there is no me without you!

ACKNOWLEDGEMENTS

As my advisor has always said, “Science is greater than the sum of its parts.” I made it this far because many hard working individuals invested countless hours in my development as a scientist. I can’t offer an exhaustive list but I can certainly cover the star players! Dr. Conner and Mr. Helf, my high school physics teachers, introduced me to the subject and always made certain that the presentation was engaging. Perry Tompkins, my undergraduate advisor, gave me an excitement for instrumentation, data acquisition, control, and automation nearly a decade ago. It was a time when I was preoccupied with many of the social aspects of college and when I thought my future was in graphic arts. Perry truly gave me the tools I would need to become a successful experimentalist and a critical thinker. My friendship with Perry also resulted in the birth of my dream to join the astronaut corps.

Thanks go to Professor Steve Durbin at Purdue and Professor Royal Albridge at Vanderbilt. Both ran excellent NSF REU programs that crystallized my interest in experimental physics. Chase Boulware, a former graduate student at Vanderbilt, was my lab mate for many years. I’m sure Chase’s contributions are too numerous to mention. I think I picked up my habit of rocking up on my toes during an explanation from him! Heather Andrews has been a great colleague and has always had the misfortune of being a sounding board for my many half-cooked ideas. Thanks Heather! Kelvin Wong has toiled endlessly to produce high quality cathodes, and without him the data presented here wouldn’t exist.

Thanks are due to my thesis committee. They have always been exceedingly accommodating with regards to scheduling and they have offered important advice and criticism (constructive of course!). Thanks to all the administrative and support staff in the physics department at Vanderbilt. You made my stay here a very smooth one. A special note of thanks goes to John and Bob in the machine shop. Their advice, expertise, skill and friendship was invaluable. That’s another thank you that I owe to Perry. He told me

to make sure I became friends with the machinists and the people in financial! John, Bob, Eric, Martha, Sheila, Melissa, Jane, and Libby made that part easy. Peggy, Don, Barbara, and Sandy have helped me with everything from registration and paychecks to mysterious smells in the lab. Thanks guys!

Lastly, on the academic side, I want to recognize my advisor, Charlie. I know I've probably done and said some exceedingly nonsensical things in the past six years. Charlie never gave up on me. Besides a conducive environment for research and interesting topics to work on, I think the most important thing that Charlie gave me was the intuition for approximation. Charlie has a wonderful way of approaching problems, simply. Over the course of many years I shed the fetters of quantitative precision for precision's sake and developed the ability to very quickly estimate effects in a given situation. This saved me untold days of work in more ways than I can count. I certainly owe the bulk of my maturity as a physicist to Charlie's investments in me. Thanks, Charlie. It has been and continues to be a wonderful collaboration!

My poor wife, a thesis widow for these many months! Hillary, I never could have made it this far without your love and support. Your constant belief in my ability and my dreams has been the fuel for my efforts on so many occasions. I can never repay you! I'm so happy about our new beginning. You complete me in every sense of the word!

TABLE OF CONTENTS

LIST OF TABLES

LIST OF FIGURES

CHAPTER I

INTRODUCTION

I.1 Beam-driven radiation sources and electron-beam brightness

Free electron beams have been used as the basis for radiation sources over a large extent of the electromagnetic spectrum from the GHz to the x-ray. These sources have the important property of wavelength tunability through both the electron beam energy and the device geometry and operational characteristics. Devices such as the klystron and cavity magnetron provide high power levels in the GHz range. Backward wave oscillators (BWO), traveling-wave tubes (TWT), and similar devices have excellent coverage of the centimeter and millimeter wave range [1]. Traditional undulator based free-electron lasers (FEL) have been, or are being, constructed in virtually every part of the spectrum from the THz [2] to the x-ray [3]. Additionally, tabletop THz devices based on Cerenkov [4] or Smith-Purcell radiation [5] have been developed and are beginning to fill an important gap where few other sources exist.

The challenge of extracting kinetic energy from an electron beam in the form of electromagnetic radiation is one that hinges principally on beam quality. Generally speaking, in a beam-driven radiation source the electron beam must be confined to a certain transverse area for sustained interaction. This interaction region is set by the geometry of the source's radiation modes and sets the principal requirements for electron beam intensity and focusability. These qualities include, above all, the electron beam's transverse brightness, i.e. the beam ensemble's current density in so-called trace space, which is given by

$$B = \frac{d^4 I\left(x, x', y, y'\right)}{dx dx' dy dy'}, \tag{1.1}$$

where $I\left(x, x', y, y'\right)$ is the current density, x and y are the transverse position coordinates,

and $x' = dx/dz$ and $y' = dy/dz$ are the x and y divergence relative to the electron-beam axis (z). A large brightness indicates an intense beam that may be well collimated while having a small transverse spatial extent. This brightness can be normalized as $B_N = B/\left(\beta^2\gamma^2\right)$, where β and γ have the usual relativistic meaning, so that it is invariant under accelerations. Another useful quantity is the electron beam's normalized transverse emittance, which is

$$\epsilon_{N_x} = \beta\gamma\sigma_x\sigma_{x'}, \tag{1.2}$$

where σ_x and $\sigma_{x'}$ are the rms radius and rms divergence of the beam respectively. The emittance and its relevance in describing beam ensembles is discussed in further detail in Chapter 4. The typical requirement on the emittance of a beam in an FEL is that it be smaller than the emittance of the photon beam, i.e.

$$\frac{\epsilon_{N_x}}{\beta\gamma} \leq \frac{\lambda_{fel}}{4\pi}, \tag{1.3}$$

where λ_{fel} is the resonant wavelength of the FEL interaction.

Presently, there are two main frontiers in FEL development, both depending on the use of bright electron beams: x-ray FELs such as the Linear Coherent Light Source (LCLS), and high-average power FELs (HAPFEL) in excess of the 14 kW average power record set at Thomas Jefferson National Accelerator Facility (TJNAF, J-Lab). While the beams required for x-ray devices are higher brightness than those of high-power IR FELs, they do not require large average currents. The LCLS gun has already achieved bunch charges of $\sim$ 1 nC at normalized transverse emittances of $\sim$ 1.2 μm-rad, however the average current of this injector is only $\sim$ 100 nA. Among the most important development areas in the field of HAPFELs is that of high-brightness, high average current electron injectors. It can be argued that injector development is the last opportunity for order-of-magnitude improvements in FEL performance as the extension to higher average power operation is made. There are presently several different approaches for developing such injectors.

These include the normal conducting (NC) RF photo-injector at Los Alamos National Laboratory (LANL), the high voltage DC photo-injector at J-Lab, and the superconducting (SC) RF photo-injector being jointly developed by Advanced Energy Systems (AES) and Brookhaven National Laboratory (BNL).

I.2 **Existing cathode technology**

Figure 1.1 presents the normalized brightness and peak operating current for various cathode and injector technologies; the current spans ten orders of magnitude and brightness spans nine orders of magnitude. There are three primary cathode technologies: thermionic, photocathodes, and field emitters. There are also intermediate varieties such as photo-field emitters and photo-thermal cathodes (not plotted) [6]. While field and photo-field emitters have been recently tested in a high-voltage DC gun (100 kV) [7, 8], feasibility has not yet been demonstrated in RF injectors. Thermionic sources provide beams with moderate current and emittance, but the emission is not easily gated. Without gating, the cathode emits into RF phases that result in electron back bombardment and excessive cathode heating. This is prohibitive in the context of a high-average-current injector.

By far, the dominant cathode technology in modern FEL development is the photocathode. The nature of the emission mechanism allows gating with the drive laser at the proper RF phase, avoiding the problem of electron back bombardment. Photocathodes are divided into two main subtypes: metal, and semiconductor. Metal photocathodes require higher photon energy for emission and have lower quantum efficiency (QE), but are rugged and have extremely fast response times. The semiconductor variety, while having high QE and requiring low photon energy, have slower response times, are very fragile, easily contaminated, have shorter operational lifetimes, and must be produced and stored in vacuum. The use of photocathode technology is complicated, especially for high-average-power operation, by the need for complex mode-locked-laser systems. The laser systems required for 100 kW class FELs are currently being developed, however, those required for

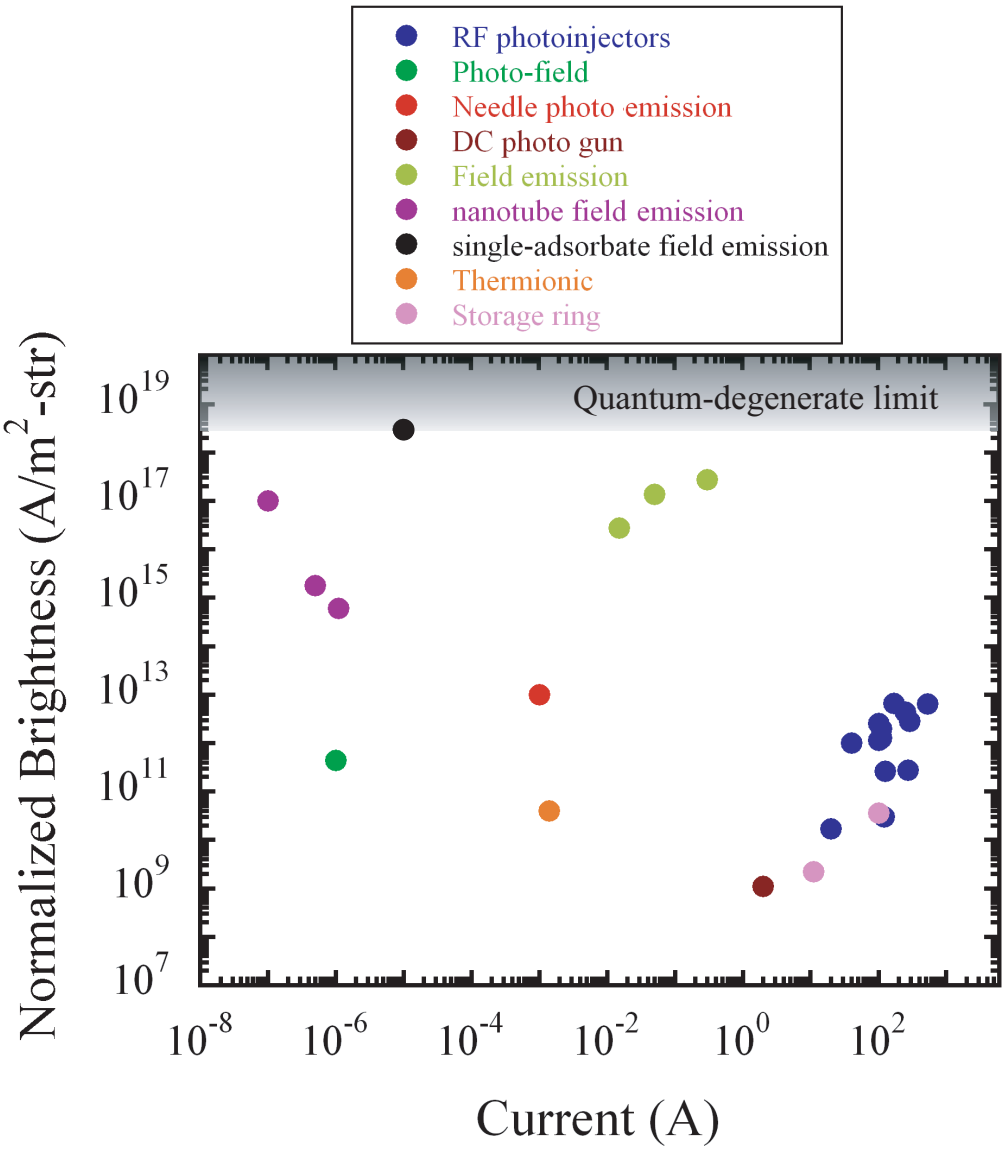

Figure 1.1: The brightness of various cathode and injector technologies span ten orders of magnitude in current and nine orders of magnitude in normalized transverse brightness.

MW class FELs are far beyond the state of the art. Presently, all of the high-average-current injector designs are based on the use of photocathodes.

Field emitters offer an interesting alternative to photocathodes in future injector systems. Field emission is exquisitely sensitive to the applied electric field at the cathode surface. This can be used to gate the emission at the proper RF phase using various techniques discussed in Chapter 2. Perhaps the most important feature of field emitter cathodes is the elimination of the drive laser. This removes the need for a laser window on the injector and avoids the laser heating present with photocathodes. This is especially important when considering the thermal constraints placed on SCRF injectors. The only waste heat produced by field emitters is the self-joule heating from conducting electrons to the emitter surface. While the pulsed-field-emission current demonstrated with single needle cathodes is too low for use in high-average current injectors, high-brightness, moderate current beams have recently been produced by pulsed photo-assisted field emission from ZrC needle cathodes. A more promising cathode utilizing field emission is the so-called field-emitter array (FEA), a planar array of micro-fabricated field emitters. These devices can be manufactured with and without self-aligned gating electrodes. Additional gating electrodes can be added for focusing or beam collimation to minimize transverse emittance. Of principal interest in this thesis are diamond field emitter arrays (DFEA).

I.3 **Diamond Field Emitter Arrays**

DFEAs, shown in Figure 1.2, were developed at Vanderbilt in the Department of Electrical and Computer Engineering more than a decade ago. Originally investigated for a variety of uses involving high-power vacuum electronics, high-current switching, and thermal-electric conversion, only recently have DFEAs been considered and developed for use in beam-driven radiation sources. DFEAs have demonstrated their rugged nature by providing high per-tip currents, excellent temporal stability, and significant resistance to

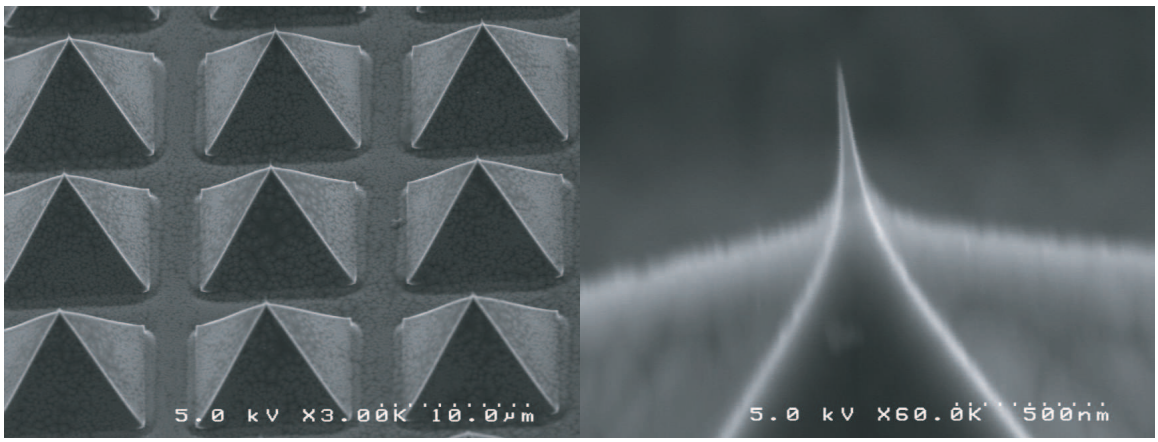

Figure 1.2: SEM micrographs of a DFEA; wide view (left) and tip detail (right).

back-bombardment damage during poor vacuum, close-diode DC operation. The material properties of diamond have allowed DFEA operation in regimes inaccessible to traditional metal field emitters. The performance of DFEAs is rapidly increasing and under picosecond pulsing will likely reach kA/cm^2 current densities at the cathode. DFEAs are currently slated for testing in the 250 kV DC injector at the Naval Postgraduate School (NPS), and collaborative testing in SCRF and NCRF injector systems is being planned at NPS and other institutions. While much work remains involving their integration into RF injectors, DFEAs have demonstrated exciting potential for greatly simplifying the injector system for HAPFELs.

I.4 The Quantum-Degenerate Limit of Brightness

The potential inside a solid defines certain allowed energy states which the conduction electrons occupy with a spectral density of one spin pair per state. These states are filled up to the so-called Fermi energy, and the ensemble is quantum degenerate. This degeneracy, a consequence of the anti-symmetry of fermionic wave functions, suppresses electron-electron scattering and is the source of the high electrical conductivity of metals. The effects of degeneracy also exist in an ensemble of free electrons, however, with most cathode types the degeneracy is so low that it is of no practical consequence. Field

emission is the only emission mechanism that approaches the brightness required to produce significant levels of quantum degeneracy [9–11]. A weak degeneracy signature has been successfully measured for a tungsten field emitter in recent years [12]. These experiments observed clear deviations from Poissonian arrival statistics of electrons at the detector system, an unmistakable signature of quantum degeneracy. A simpler technique for estimating a source's quantum degeneracy is the use of low-energy point-projection microscopy [9]. As the electron waves pass a hard edge, they scatter and interfere with themselves at a downstream detector. The Fresnel fringes produced by this interference can be used to measure the transverse coherence length for the beam, which can in turn be used to estimate the quantum degeneracy. As the brightness of an electron beam is increased, the phase space volume occupied by the beam is packed more and more densely. Eventually one reaches a quantum degenerate limit, where the geometric symmetry of the electron wave functions prohibits denser packing. For a given spread in electron energy, the transverse brightness is restricted by degeneracy. The degenerate limit corresponding to an energy spread $\Delta E \approx 0.3$ eV (typical of field emitters) is displayed in Figure 1.1. Calculations demonstrate that recent experiments at Vanderbilt involving multi-wall carbon nanotubes (MWCNT) and adsorbed species have approached this quantum limit. While these sources are not well suited for use in FELs, there are exciting effects and techniques to be explored in the use of degenerate beams as a new imaging modality.

I.5 **Thesis Outline**

The primary purpose of this thesis is to detail recent progress in the development of high-brightness cathodes for use in beam driven radiation sources. In Chapter 2, DFEAs are introduced, details of their fabrication are given, and their application to conventional free-electron lasers is considered. Chapter 3 details the successful development of uniformity conditioning techniques, which address differences in contamination and morphology between emitters in DFEAs. Chapter 4 presents measurements and simulations of the

transverse emittance of beams from DFEAs. Chapter 5 discusses the design, construction, and testing of a high-resolution energy analyzer and measurements of the emitted energy spectrum from DFEAs. Chapter 6 considers the Smith-Purcell free-electron laser (SPFEL), a compact terahertz device, as an application of DFEA cathodes. The SPFEL is covered in extensive theoretical detail, including three-dimensional, and three-dimensional confined-mode variations. This theory is used to guide the design of a DFEA driven SPFEL. Chapter 7 discusses the concept of quantum degeneracy in a free-electron beam and presents recent progress in our development of a carbon nanotube based quantum-degenerate electron beam source. In the conclusions, the results of this thesis are summarized and details of future DFEA development are discussed.

CHAPTER II

DIAMOND FIELD-EMITTER ARRAYS

II.1 Introduction

Field-emitter arrays were first developed by Spindt at SRI in the mid 1960's [13] marking the birth of what is now known as vacuum microelectronics. These devices are based on the physical process known as field emission, where a metal or semiconductor immersed in an electric field of order 1-10 V/nm will begin to emit electrons from its surface. The emission depends fundamentally on the quantum mechanical principle of tunneling whereby the wave function of electrons inside the solid penetrates through the local surface energy barrier into the vacuum. This penetration provides a nonzero probability that electrons will spontaneously appear on the vacuum side of the interface where they are subsequently swept away under the influence of the applied electric field. The rate of electron emission from metals based on this principle was first derived by Fowler and Nordheim in 1928 [14], and subsequently refined by Murphy and Good in 1955 [15]. At low temperature (even up to room temperature) the emitted current density, J_{FN}, is shown to have the form

$$J_{FN}(F) = a_{fn} F^2 e^{-b_{fn}/F} \tag{2.1}$$

where a_{fn} and b_{fn} are constants depending on the work function, and F is the electric field at the emitter surface. Field emisison may typically be identified as such by plotting the I-V data with $\ln(I/V^2)$ as the ordinate and $1/V$ as the abscissa. Fowler-Nordheim-like emission will appear as a straight line where the slope and y-intercept depend on the constants b_{fn} and a_{fn} respectively. When the emitter is a semiconductor, the emission is Fowler-Nordheim like for low current operation. However, at high enough current the

electron supply from the bulk semiconductor is mobility limited and the I-V response becomes Ohmic in character. The theory of field emission from semiconductors was first reported by Stratton in 1955 [16, 17], an analysis which included the effects of surface states, field penetration and the resulting band bending.

More interesting field-emission effects occur when atoms or molecules are adsorbed onto the emitter surface. The electronic states of an adsorbate immersed in the applied field have certain allowed energy levels. When these energies are resonant with an occupied region of the emitter's density of states, large enhancements of the field-emitted current occur. Moreover, because the adsorbate's electronic states are confined to a small spatial extent, the emission enhancement is highly localized. Resonant tunneling also causes significant changes in emitted electron energy distribution, both in structure and in position relative to the Fermi energy. Resonant tunneling enhancement and angular collimation of electron beams from single adsorbates has been described in detail by Gadzuk [18, 19].

II.2 **Fabrication of DFEAs**

II.2.1 **Ungated devices**

Ungated diamond field-emitter arrays are produced using a mold-transfer process pioneered by researchers in the Department of Electrical and Computer Engineering at Vanderbilt [20]. This eight step process is presented in detail in Figure 2.1. Oxidized Si wafers are patterned in preparation for an anisotropic KOH etch that produces pyramidal molds with an opening angle of $70.6\,^{\circ}$. These molds are sharpened by oxidation in preparation for diamond deposition. The oxide grows preferentially on the walls of the mold, avoiding the corners (Figure 2.2). The result is a sharp recess in the tip of the mold where the faces of the pyramid converge. By using mask holes that are slightly rectangular we can produce two sharp tips rather than a single. Over or under etching of the mold prior to oxidation allows production of quad-tip emitters.

After sharpening, the mold is pretreated by ultrasonication in a diamond slurry, a step

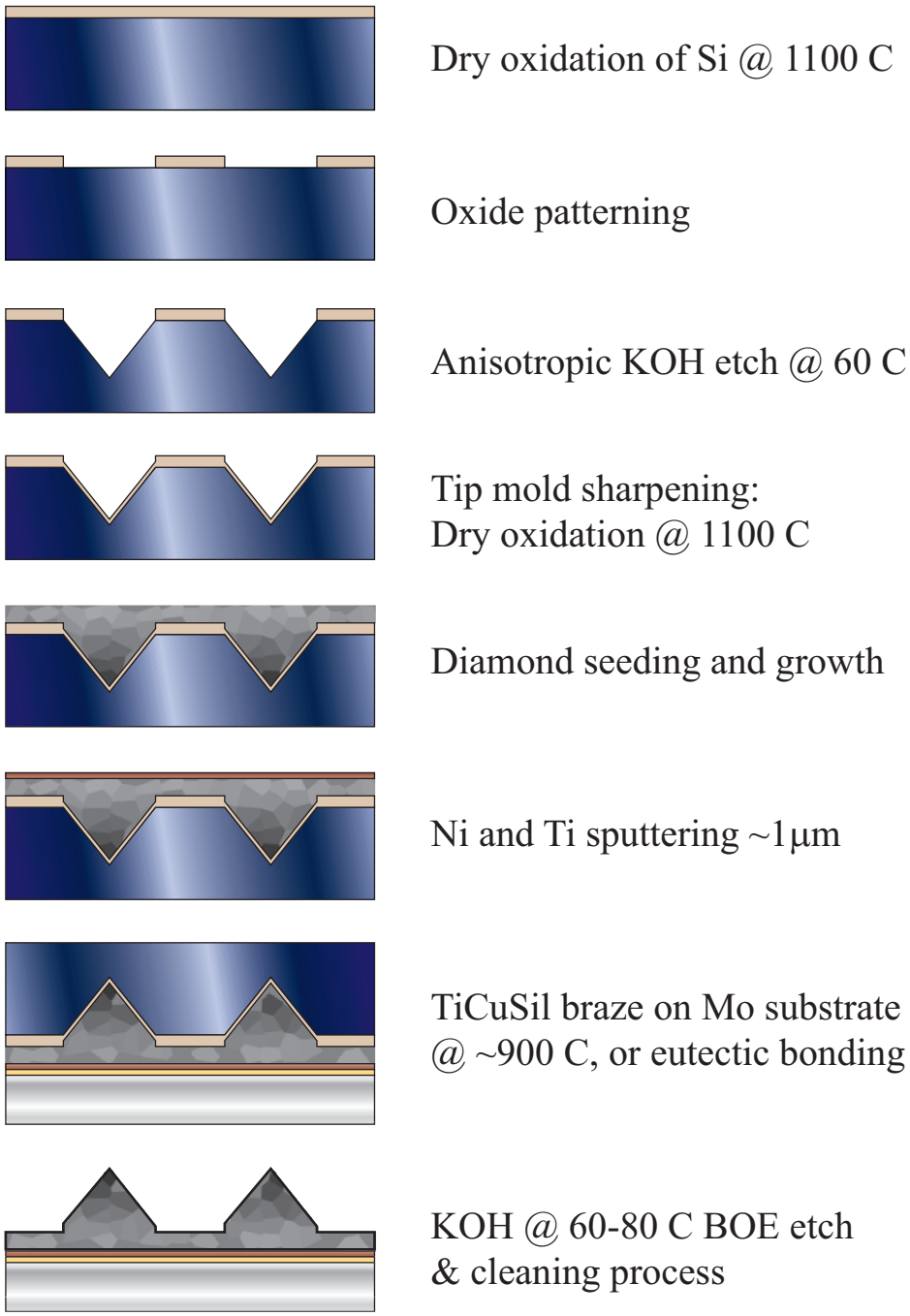

Figure 2.1: DFEA fabrication process flow

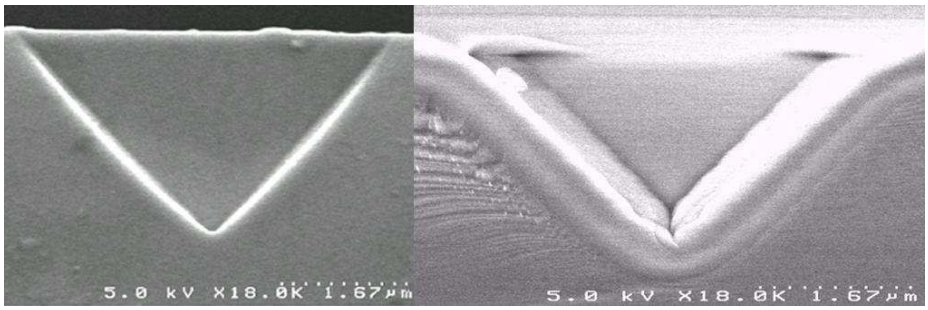

Figure 2.2: Si mold before (left) and after (right) oxide sharpening

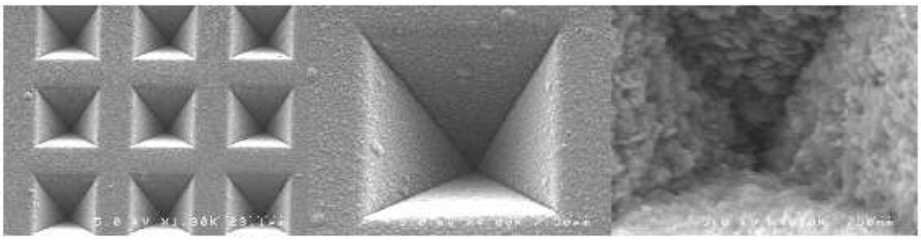

Figure 2.3: Conformal nanodiamond layer on Si mold prior to microdiamond deposition

which provides nucleation sites for diamond growth. Diamond is then grown in the mold by microwave-plasma chemical-vapor deposition (MPCVD). A variety of growth recipes are used to achieve a desired combination of sp^2 and sp^3 carbon, dopant concentration, and nitrogen content. A thin, conformal, nanodiamond layer is deposited first (Figure 2.3), while microdiamond is used to back fill the bulk of the structure. The diamond is then sputtered with a Ni/Ti coating that serves as a buffer/adhesion layer during substrate brazing. TiCuSil braze is used to attach the cathode-mold structure to a polished Mo substrate. After brazing, the protective Si mold is removed with a KOH etch, and the sharpening oxide is removed with a buffered oxide etch (BOE). Following standard cleaning procedures, the cathode is ready for testing. A completed diamond field-emitter array is seen in Figure 2.4.

II.2.2 **Gated devices**

In gated device development it is important to use a process which guarantees self alignment of the gate electrodes to the emitter tips. This reduces the number of required

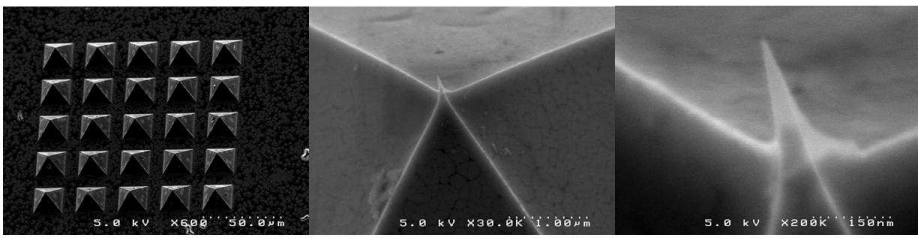

Figure 2.4: Completed diamond FEA with tip detail

steps and the required precision of the process. The gated DFEA fabrication process, shown in Figure 2.5, is identical to that of the ungated device up through the brazing procedure. However, an SOI wafer with a buried oxide layer (BOX) is used in place of the plain Silicon wafer of the ungated process. After brazing, the handle Si is etched with the BOX serving as an etch stop. After BOX removal, the remaining Si is thinned using an isotropic etch. This etch is terminated shortly after the Si level passes the buried emitter tips. The gate oxide is then removed from the tip area and the completed device is ready for testing. An example of a gated DFEA is shown in Figure 2.6. One of the primary challenges with gated device development thus far has been the presence of conductive leakage pathways in the gate oxide. Presently it is believed that the plasma exposure during diamond growth may result in loss of electrical standoff capabiilty. Other possible explanations include cracking of the oxide layer during fabrication and contamination of the exposed oxide near the emitter tip. Several experiments are underway to determine the source of this leakage. Procedures are also being developed for the addition of a second self-aligned-gate electrode which can be used to collimate the individual beamlets emerging from the array as seen in Figure 2.7. This will provide a substantial reduction in the array's transverse emittance.

II.2.3 **Diamond coated Silicon devices**

A parallel FEA development program involves deposition of various types of CVD diamond on silicon microtip arrays. Silicon microtip arrays are produced by isotropic etching of a silicon wafer with a patterned surface oxide. Tips may be subsequently sharpened by a dry oxidation technique. The smooth silicon surface must be prepared

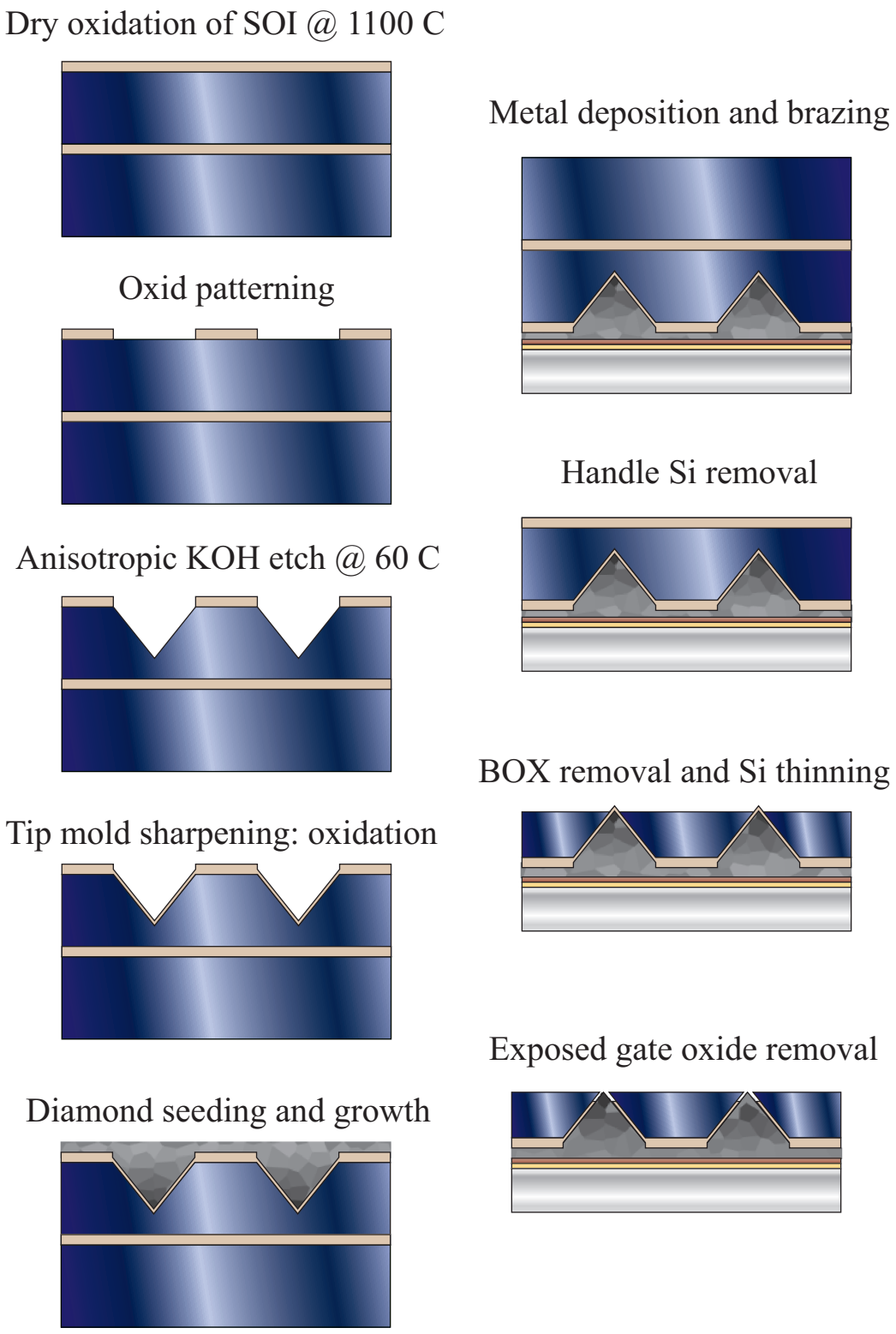

Figure 2.5: Gated DFEA process flow.

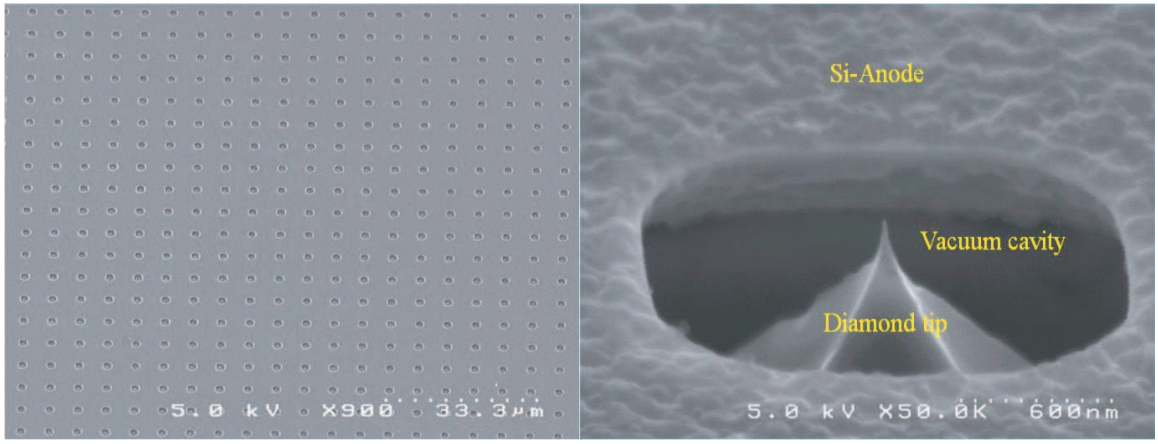

Figure 2.6: Completed gated DFEA with tip detail.

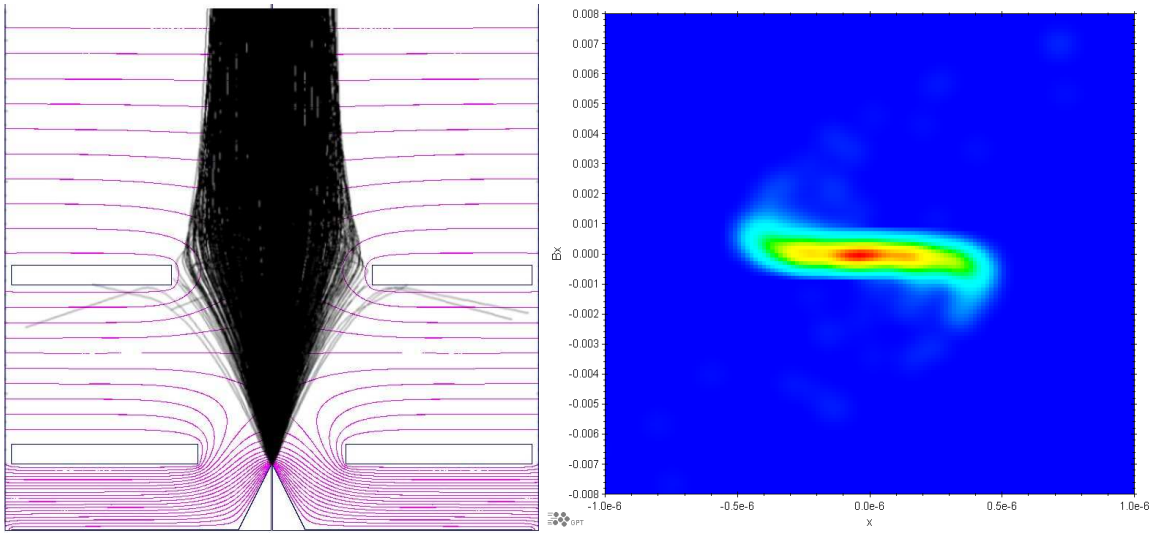

Figure 2.7: Simulation of beamlet propagation through a double-gated FEA cell. The current density plot to the right shows the (x, β_x) phase space projection of the beam ensemble at end of the simulation.

for diamond growth by sonication in a diamond slurry. Prior to sonication, photoresist is spun on the array such that only the very tips are exposed. This ensures enhanced diamond nucleation on the tips during the growth process. Multiple diamond growth recipes have been used resulting in the different diamond structures in Figure 2.8.

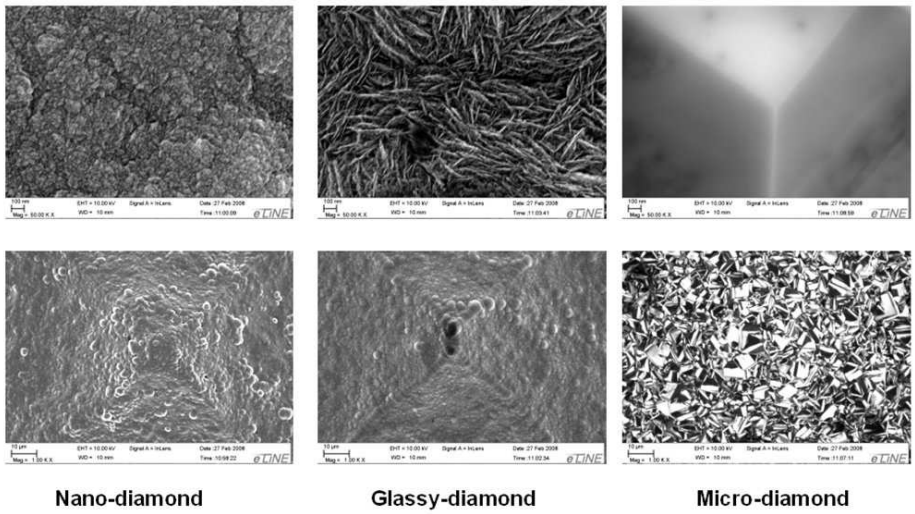

Figure 2.8: Various types of CVD diamond deposited on a single Si tip. The top row presents a detailed view of the microstructure of each diamond type.

Thus far, it has proven difficult to grow thin conformal layers of diamond that maintain a small tip radius. Accordingly, field enhancement at the tip has been small and the required macrofields are prohibitively large for convenient testing in existing DC teststands. A coated Si tip is pictured in Figure 2.9. Once growth procedures are improved, the performance of different types of diamond can be examined.

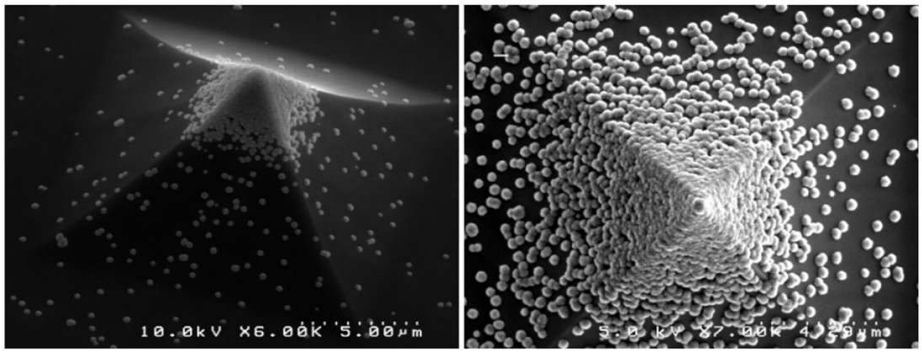

Figure 2.9: Nanodiamond coated Si tip

II.3 **Integration of DFEAs with Electron Guns**

There are three different injector types into which DFEAs must be integrated: high-voltage DC, NCRF, and SCRF. The transverse-emittance measurements detailed in Chapter 4 demonstrate that ungated DFEAs possess sufficient beam quality for driving HPFELs. While ungated devices are very rugged, control of the emission level and timing is not very flexible and depends on geometric enhancement of the electron gun's applied field. In contrast, for a gated device the emission timing and tip field are controlled by the potential applied to the nearby gate electrode, and the gun's field serves only for extraction. However, generally speaking, gated devices are more susceptible to catastrophic failure. If the gate electrode and cathode are shorted together at even a single point, either by damage or contamination, the ability to apply the requisite fields is lost. We consider first the general integration strategies for DC guns.

Integration of an ungated cathode with a high-voltage DC system is rather straightforward. As an example, we consider the 250 kV DC gun at NPS. In its present configuration the NPS gun can provide fields on the order of 1.5 V/μm at the cathode surface. Currently DFEAs require $\sim$ 10 V/μm for moderate current operation. To increase the electric field, the cathode can be secured to the end of a stalk that is extended towards the anode. Early simulations by Lewellen [21] demonstrate available fields on the order of $\sim$ 7 V/μm in this configuration. This will be sufficient for preliminary investigation of the long-term emission stability of DFEAs in the presence of high-energy ion back bombardment. If the stalk is actuated, then the emission level may be controlled without changing the total beam energy. However, the variable geometry will change the beam propagation through the gun optics. Care must be taken to avoid excessive beam scraping or beam quality degradation. For gated devices, it is only required that an electrical feedthrough be provided to energize the gate electrode. Simple schematics of gated and ungated device integration in the existing NPS gun are shown in Figure 2.10.

The primary challenge of DFEA integration with RF injectors is that of timing the

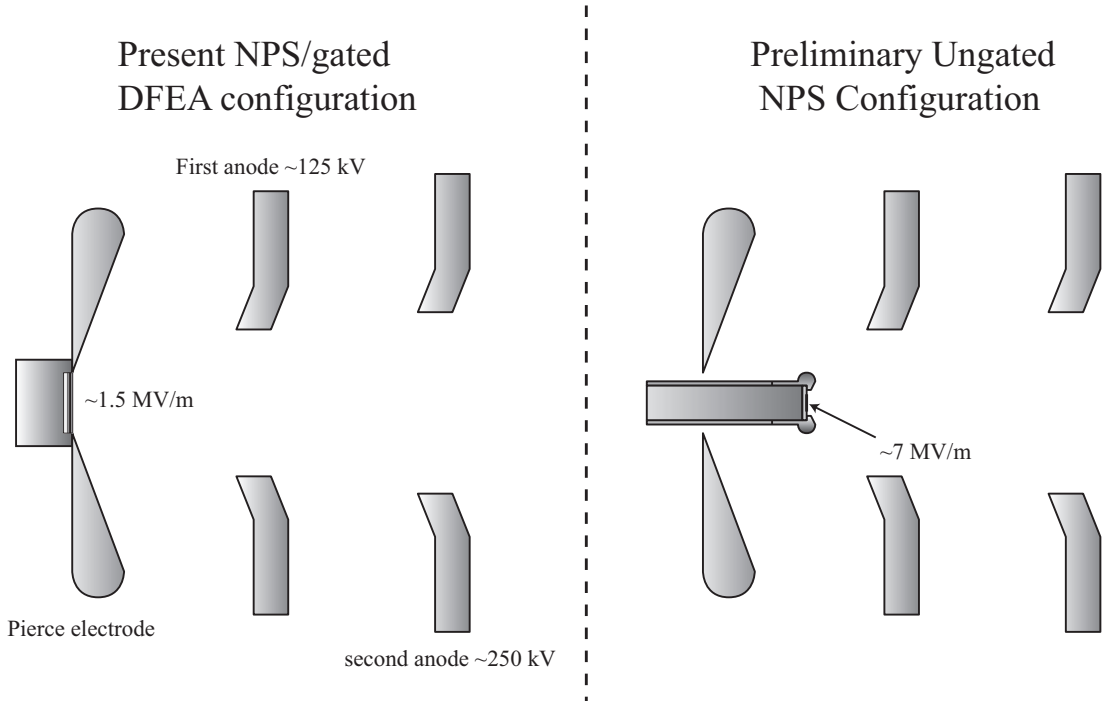

Figure 2.10: Integration of gated and ungated DFEAs into the present configuration of the NPS DC gun.

electron emission relative to the RF phase. From (2.1) we see that the emission current is exponentially sensitive to the applied electric field. As a result, the emission current from a DFEA in an RF injector would be strongly peaked at the peak of the RF phase. Emitting at this late phase may prevent the electron beam from exiting the first cell before the fields reverse polarity. This leads to large degradations in beam quality and should be avoided. One technique for decreasing the transit time in the first cell is the extension of the cathode into the cavity on a stalk. Another solution is to design a cavity which permits mixing of the RF fundamental with a higher harmonic as suggested by Lewellen [22]. The peak of the total RF field can be moved to an earlier time than the peak of the RF fundamental. Ideally, the third harmonic component is strong only near the cathode surface. This could possibly be achieved by recession of the cathode into the back wall of the gun [23]. As with DC guns, gated devices have more flexibility regarding time gating of the electron emission. The gate electrode may be driven by a low power coaxial feed with either harmonics of

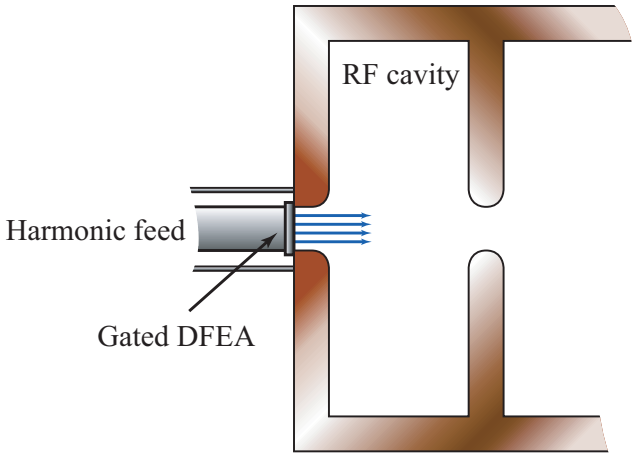

Figure 2.11: Integration of a gated DFEA with an rf cavity using a low-power harmonic feed to gate the emission.

the RF fundamental or a phase-shifted fundamental. Such an arrangement is shown in Figure 2.11. To date, the high frequency response of gated DFEAs has not bean measured. Also, the level of Ohmic and dielectric losses in the gate electrode and gate oxide must be measured, and their consequences for high frequency operation in both NC and SC guns must be considered. These measurements may be taken once the aforementioned gate oxide leakage has been eliminated.

CHAPTER III

EMISSION UNIFORMITY OF DFEAS

III.1 FEA Non-uniformity and its Origins

Historically, one of the most significant barriers to the adoption of FEA technology has been the difficulty of providing uniform emission current over a large spatial extent. Consider a single field emission source; The emitted current is extremely sensitive to properties such as geometry, work function, and surface contamination. Small fabrication variations in emitter tip radius, height, chemical composition, and crystalline orientation can result in order of magnitude differences in the emission current between tips in an FEA. Additionally, the strong electric field gradient near the cathode attracts polarizable species from the vacuum to the cathode surface. The induced dipole moment of an adsorbate can significantly lower the local-surface energy barrier for emission. Additionally, adsorbate effects such as resonant tunneling may produce order-of-magnitude enhancements in the local emission current. The configuration of adsorbates on the cathode surface is in a state of constant flux. There are three primary effects involved, each leading to changes in temporal and spatial emission uniformity: adsorption, surface diffusion, and desorption. The adsorption dynamics are driven primarily by background gas levels, binding site availability, and the probability of successful binding when an attempt is made. Once an adsorbate is bound to the cathode surface it undergoes a pseudo-random walk, hopping between binding sites toward the region of highest field, with an approximate rate given by [24]

$$R_{diff} = \nu\, e^{-\Delta E/k_B T}, \tag{3.1}$$

where ν is the attempt frequency (typically the vibrational frequency of the adsorbate on the surface), ΔE is the approximate energy barrier for the transition, k_B is the

Boltzmann constant, and T is the local surface temperature. Similarly, the desorption rate is approximately

$$R_{des} = \nu \, e^{-\Delta G / k_B T}, \tag{3.2}$$

where ΔG is the difference in the free energy of the adsorbed and desorbed states. The most important feature of these processes is their exponential sensitivity to the local surface temperature. Non-uniform emission produces different levels of self Joule heating from tip to tip, which in turn leads to fundamentally different contamination states. The population of adsorbates on tips with high emission levels should consist of a higher fraction of tightly bound species compared with weakly bound species. Simply put, when the tips heat up due to emission, the equilibrium concentration and composition of the adsorbates shifts. This can lead to tip-to-tip variations in temporal stability and emission level. There are also adsorbate effects such as resonant tunneling that can cause significant deviations from standard Fowler-Nordheim-like field-emission behavior, and change both the total current and the emitted energy spectrum markedly.

While non-uniformity due to contamination effects may be addressed by techniques such as UHV operation, global annealing of the cathode, or plasma treatment, the underlying morphological differences must be addressed to achieve a high degree of emission uniformity. As an example, consider the arrangement shown in Figure 3.1. Using the hyperbolic model of Jensen et al [25], the anode-tip separation is

$$d = r \, \cot^2 (\theta) \, , \tag{3.3}$$

where r is the tip radius and θ is the emitter-cone half angle. Assuming a grounded cathode, the approximate electric field at the emitter tip is given by

$$F_{tip} = \frac{2 \, V_{anode}}{r \cos(\theta) \, \ln\left(\frac{1+\cos(\theta)}{1-\cos(\theta)}\right)} = \frac{2 \, V_{anode}}{r \ln (4d/r)_{\theta \to 0}}, \tag{3.4}$$

where V_{anode} is the applied anode potential. The current density as a function of the local

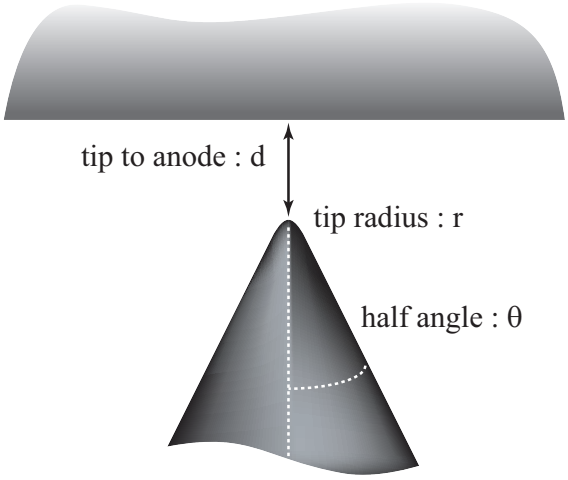

Figure 3.1: A single field emitter with cone half angle θ, tip radius r, and anode-tip separation d.

electric field is approximated by the Fowler-Nordheim equation (2.1). Integrating over the entire emitter surface provides an estimate of the emitted current given by

$$I\left(V_{anode}\right) = 2\pi r^2 \left[\frac{F_{tip}\cos^2\left(\theta\right)}{b_{fn} + F_{tip}\sin^2\left(\theta\right)}\right] J_{FN}\left(F_{tip}\right). \tag{3.5}$$

In Figure 3.2, equation (3.5) is used to calculate the emission current from each individual tip in a 100×100 array. The 10,000 tips in the ensemble are given the same work function, but have a Gaussian distribution of tip radii with a 10% rms spread. Figure 3.3 presents a histogram of the resulting emission. The difference between the highest and lowest emission level is an order of magnitude. The effect is even more pronounced when the tip radius is uniform across the array and the same 10% rms spread is applied to the work function. The highest and lowest emission levels differ by a factor of 50. Clearly, what we require are conditioning techniques that discriminate based on a tip's emission level. An excellent example of such a technique is described by Schwoebel et al [26,27] using Spindt-type Molybdenum cathodes. Nearly identical I-V response was attained for two initially dissimilar emitters by high-current pulsed conditioning, as seen in Figure 3.5 (borrowed from [27]). In this technique the combination of self Joule heating and field stress drives

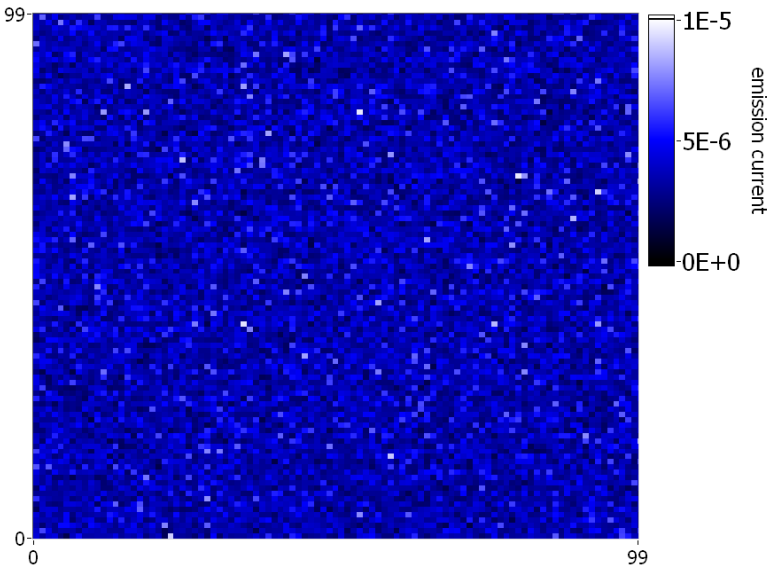

Figure 3.2: Emission distribution from an array of 10,000 tips, with an rms Gaussian spread in tip radii of 10%. $r = 10$ nm, $\phi = 5$ eV, $\theta = 35.3°$, $V_{anode} = 66.5$ V, z-scale is given in Amps

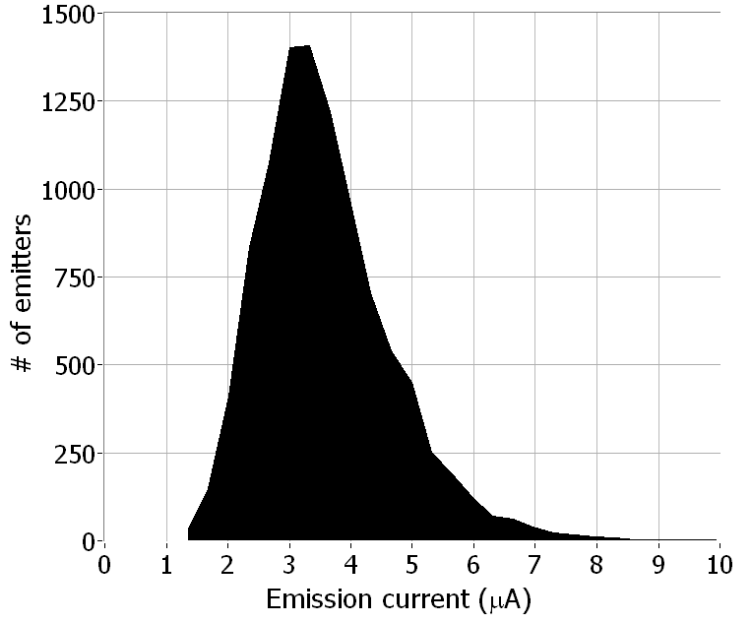

Figure 3.3: Emission histogram from results of Figure 3.2. Tip currents range from 1 μA to 10 μA

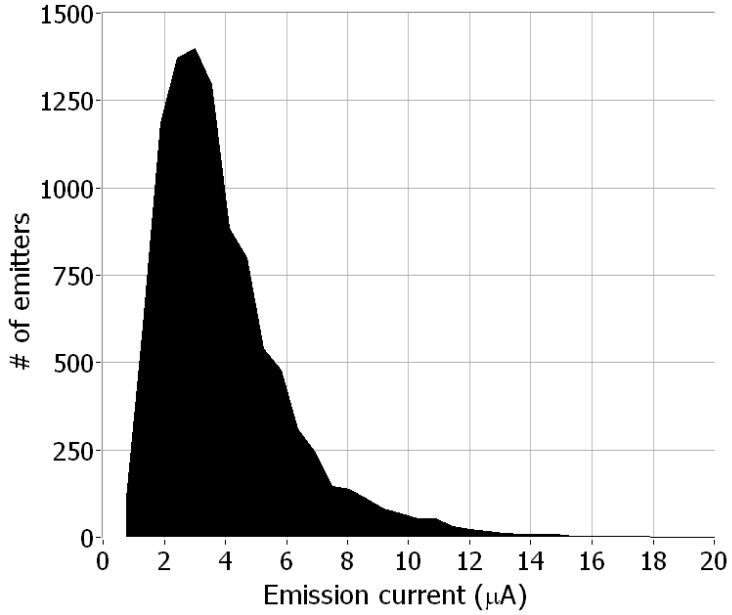

Figure 3.4: Emission histogram when using a uniform tip radius of 10 nm and a 10% rms gaussian spread in work function, centered at $\phi = 5$ eV. Tip currents range from 0.5 μA to 25 μA

geometrically similar emitters toward uniformity through surface diffusion. Such self-limiting conditioning techniques improve spatial uniformity by dulling the sharpest tips, effectively increasing the required applied field for a given current.

III.2 **Uniformity Conditioning Techniques**

III.2.1 **Vacuum-Thermal-Electric Conditioning**

When a newly fabricated DFEA is initially turned on, the emission is highly non-uniform and the observed beamlets undergo rapid flickering due to the diffusion of weakly bound adsorbates. The emitted beam from an individual tip comprises multiple small beamlets from these adsorbed species as demonstrated in Figure 3.6. Annealing the cathode at a few hundred °C while emission level fields are applied has been found to increase temporal stability and spatial uniformity significantly. We refer to this process as Vacuum-Thermal-Electric Conditioning (VTEC) [28]. A qualitative understanding can be described as follows: Elevating the temperature in equations (3.1) and (3.2) increases desorption

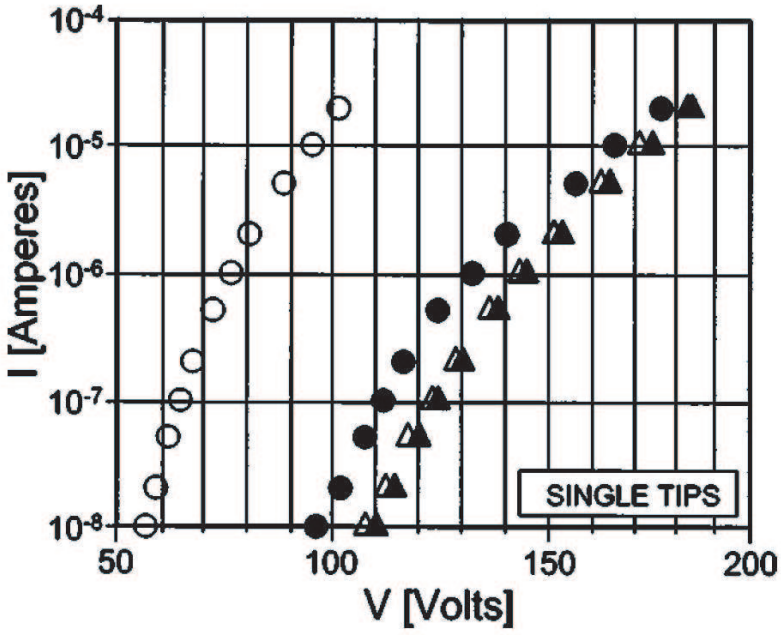

Figure 3.5: Circles show I-V response from two as-fabricated Spindt-type field emitters, and the triangles correspond to the I-V response after pulsed conditioning. The I-V behavior of the emitters after conditioning is nearly identical [27].

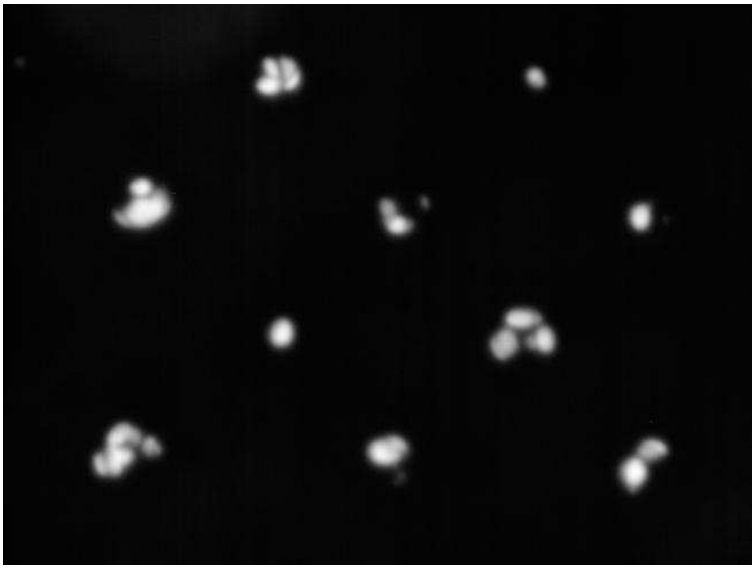

Figure 3.6: Detail of beams from individual DFEA tips. Each beam comprises multiple beamlets from adsorbed species which fluctuate due to adsorbate migration. The tips are laid out on a square grid with a 300 μm pitch.

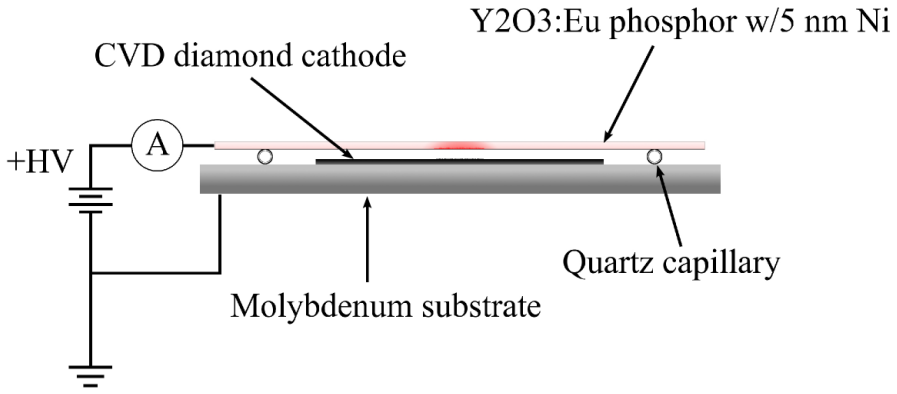

Figure 3.7: Schematic of close-diode conditioning arrangement. Anode-cathode gap is typically 120 - 300 μm, applied potential 0 - 5 kV.

and diffusion rates dramatically. Weakly bound adsorbates are rapidly driven off while tightly bound species are mobilized by the enhanced diffusion rate, migrating preferentially along the field gradient toward the emitter tips. Returning the cathode to room temperature restores the slow diffusion rates for tightly bound adsorbates and results in extremely stable field emission. Additionally, the presence of these adsorbates on the active emitting area typically results in significant reductions of the array's turn-on field.

Figure 3.7 presents the experimental configuration for conditioning studies. The cathode is set in a close-diode arrangement with a phosphor anode; Planarity and spacing are guaranteed by using precision quartz capillaries. The anode is charged to +HV and field-emitted current is measured using a logarithmic ammeter that is fiber-optically coupled to a computer data-acquisition system. The logarithmic ammeter provides good resolution over a wide dynamic range of input currents ($\sim$ 1 nA-1 mA). The conditioning apparatus used in these experiments is seen in Figure 3.8. The system is capable of providing electric fields up to $\sim$ 30 V/μm, substrate heating to $\sim$ 350 °C, and controlled gaseous environments at pressures of 10^{-3}-10^{-8} Torr.

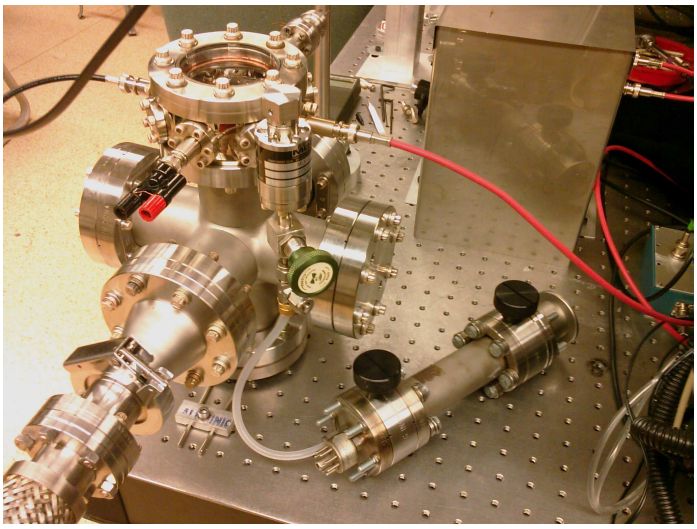

Figure 3.8: VTEC apparatus: provides 30 $\mathrm{V}/\mu\mathrm{m}$, 350 °C substrate heating, and 10^{-3} - 10^{-8} Torr controlled gaseous environment.

Figure 3.9 shows typical current data from a VTEC treatment. While the turn-on field is significantly reduced by VTEC, the effects are not permanent and decay over the course of several hours. This implies that the effects are adsorbate based rather than morphological in nature. An example of uniformity enhancement due to VTEC is shown in Figure 3.10. The apparent asymmetry in the emission intensity is due to a systematic gradient in the anode-cathode spacing for this particular run. The same 16×16 array is pictured before (left) and after (right) a 300 °C VTEC treatment. The same electric field was applied for both images, however, the current increased from 10 μA to 50 μA during VTEC. The total active fraction of emitters was increased from $\sim$ 30% to $\sim$ 60%.

III.2.2 **High-Current Conditioning**

While the ability to control adsorbed species through VTEC or similar techniques may be useful, relying on a surface-contamination effect for uniformity enhancement is not ideal. The potential target environments for DFEAs range from UHV superconducting RF guns to close-diode arrangements in field-emission displays. Conditioning techniques that

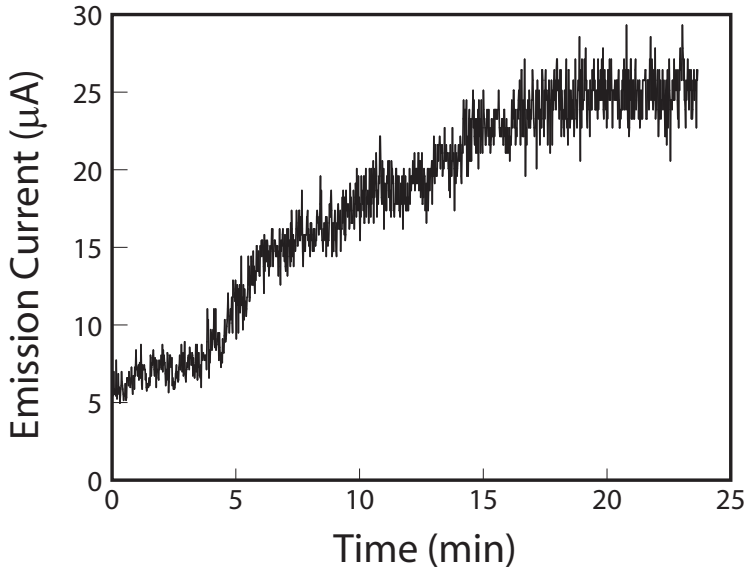

Figure 3.9: Increase in the emitted current for a fixed electric field strength during VTEC.

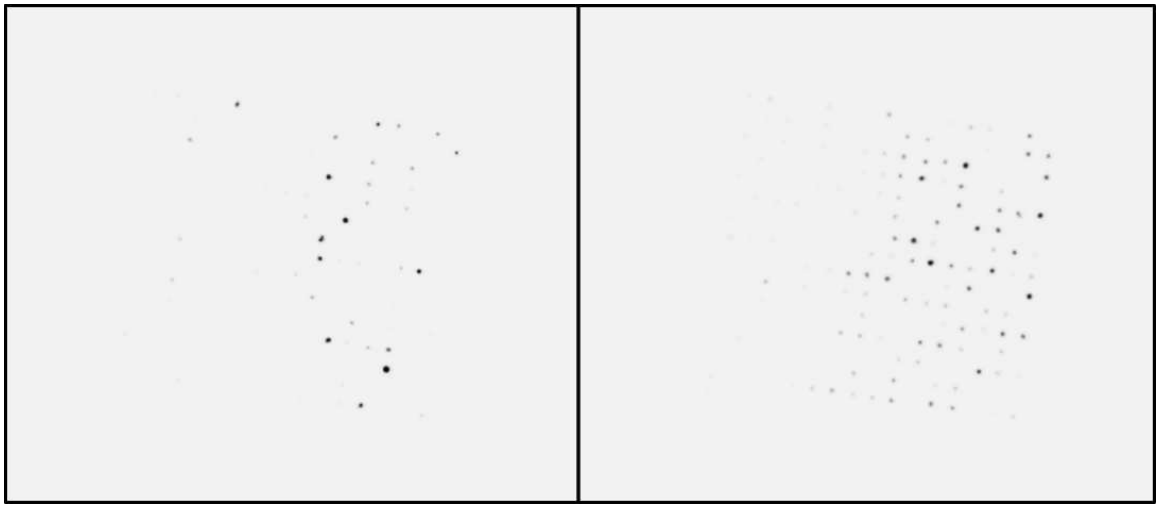

Figure 3.10: Uniformity improvement following a 300 °C VTEC treatment. The active emitter fraction increased from $\sim$ 30% (left) to $\sim$ 60% (right). Intensity values have been inverted for clarity.

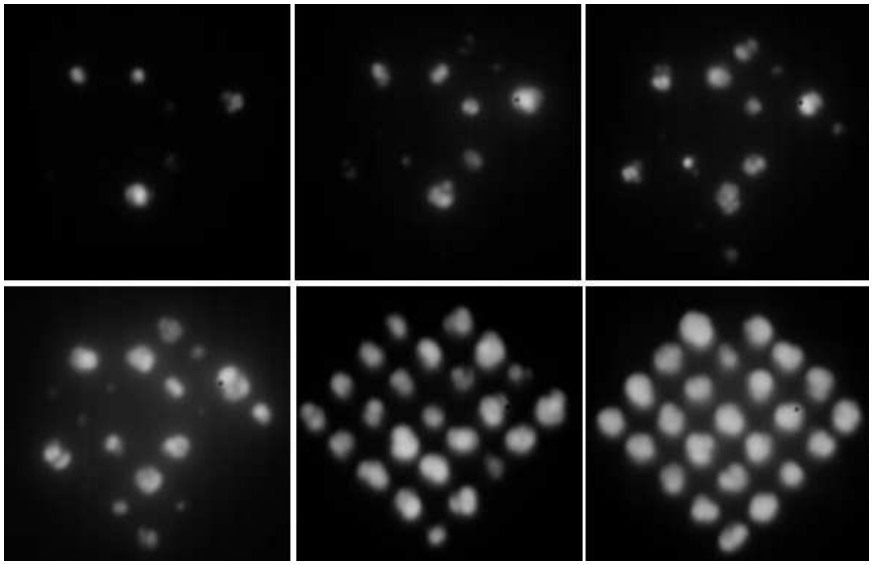

Figure 3.11: Emission uniformity progression during HCC of a 5×5 DFEA. Images were taken at progressively higher fields, ending at 15 $\mathrm{V}/\mu\mathrm{m}$. The uppermost tip was malformed during fabrication and not expected to emit

remove or compensate for variations in morphology and emitter composition are required to ensure uniform operation in this wide range of parameters.

DFEAs possess an inherent self-limiting conditioning mechanism which results in highly uniform emission after operation at moderate per-tip current levels. We observe no morphological or emission uniformity changes below currents of ~ 1 $\mu\mathrm{A}$ per tip. Driving the emitters past this level induces emission uniformity enhancement, possibly through thermal-assisted field evaporation. This phenomenon has been observed in experiments with carbon nanotube field emitters [29–31]. Self-Joule heating and the large field stresses at the emitter surface result in the evaporation of carbon clusters into the vacuum. An example of the effect of this high-current conditioning (HCC) on a 5×5 ungated DFEA is shown in Figure 3.11. The emitter base size is 10 $\mu\mathrm{m}$ and the array pitch is 100 $\mu\mathrm{m}$. During the investigation of conditioning procedures the array pitch was typically large so that the evolution of individual emitters could be studied. The uppermost tip in this array was malformed and not expected to emit. Figure 3.12 shows detail of several of the DFEA emitters before (top) and after (bottom) conditioning. The length of the

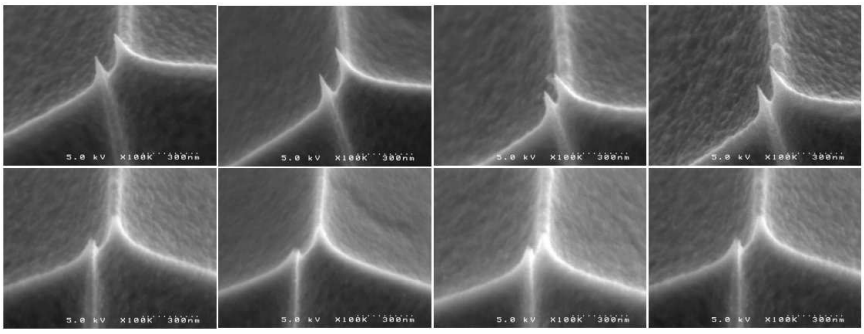

Figure 3.12: DFEA nanotips before (top) and after (bottom) HCC up to 15 μA per tip. Tips are noticeably shorter with significantly increased tip radii

nanotips is noticeably shorter and the tip radius has become significantly larger. Following conditioning, a uniform emission level of 15 μA per tip DC was achieved at an applied field of 15 $\mathrm{V}/\mu\mathrm{m}$. The high-input-power density removed the 5 nm Ni metalization from the anode locally, resulting in significant charging and preventing higher current testing. In subsequent conditioning studies, the array parameters were progressively scaled toward the desired final device, a large area array ($\sim \mathrm{cm}^2$) with high tip density ($\sim$ 4-6 $\mu\mathrm{m}$ pitch). To confirm the possibility of high tip density scaling the conditioning procedures needed validation with smaller tip geometries. As expected, conditioning of the small geometries ($\leq$ 5 $\mu\mathrm{m}$ base) has been identical to that of larger emitters (10-20 $\mu\mathrm{m}$ base). Additionally, there has been no discernable difference in the conditioning of large numbers of emitters compared to that of small ensembles. Figures 3.13 and 3.14 provide further examples of the results of HCC. Both arrays consist of 5 $\mu\mathrm{m}$ base emitters and have the same overall area. The array pitch in Figure 3.13 is 200 $\mu\mathrm{m}$ while the array pitch in Figure 3.14 is 100 $\mu\mathrm{m}$.

A careful conditioning study was performed using a 3$\times$24 ungated DFEA to rule out anode back sputtering as the source of the observed uniformity enhancement. The emitters had a 20 $\mu\mathrm{m}$ base length and were packed with a 28 $\mu\mathrm{m}$ pitch while the anode-cathode gap was 300 $\mu\mathrm{m}$. At this spacing the individual beamlets were approximately 80$\mu\mathrm{m}$ in diameter. As a result, the back sputtered material due to a single beamlet covered multiple

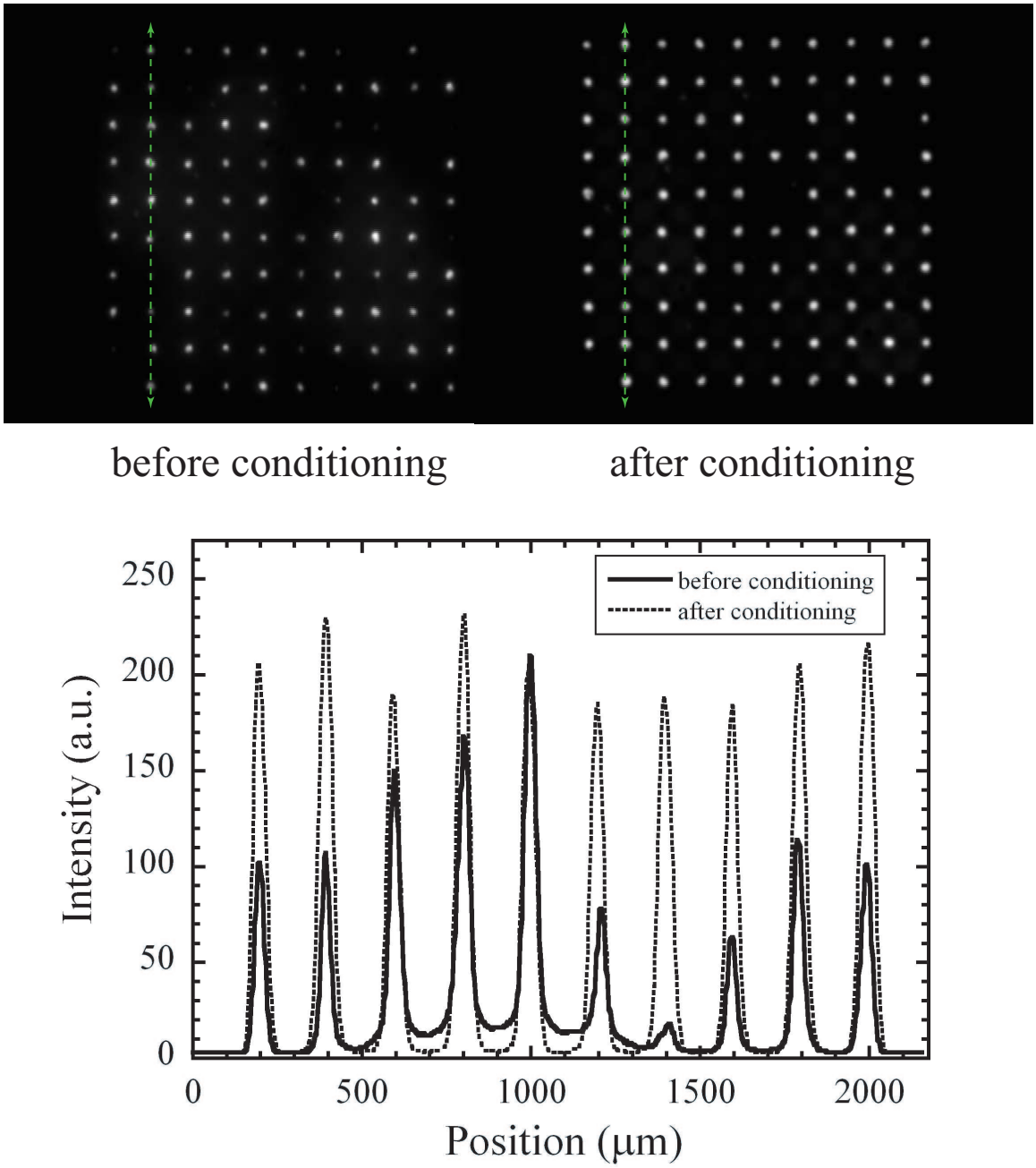

Figure 3.13: Phosphor screen images before and after HCC of a 10x10 DFEA with 5 μm emitter base and 200 μm pitch. The plot demonstrates a linescan of a single row.

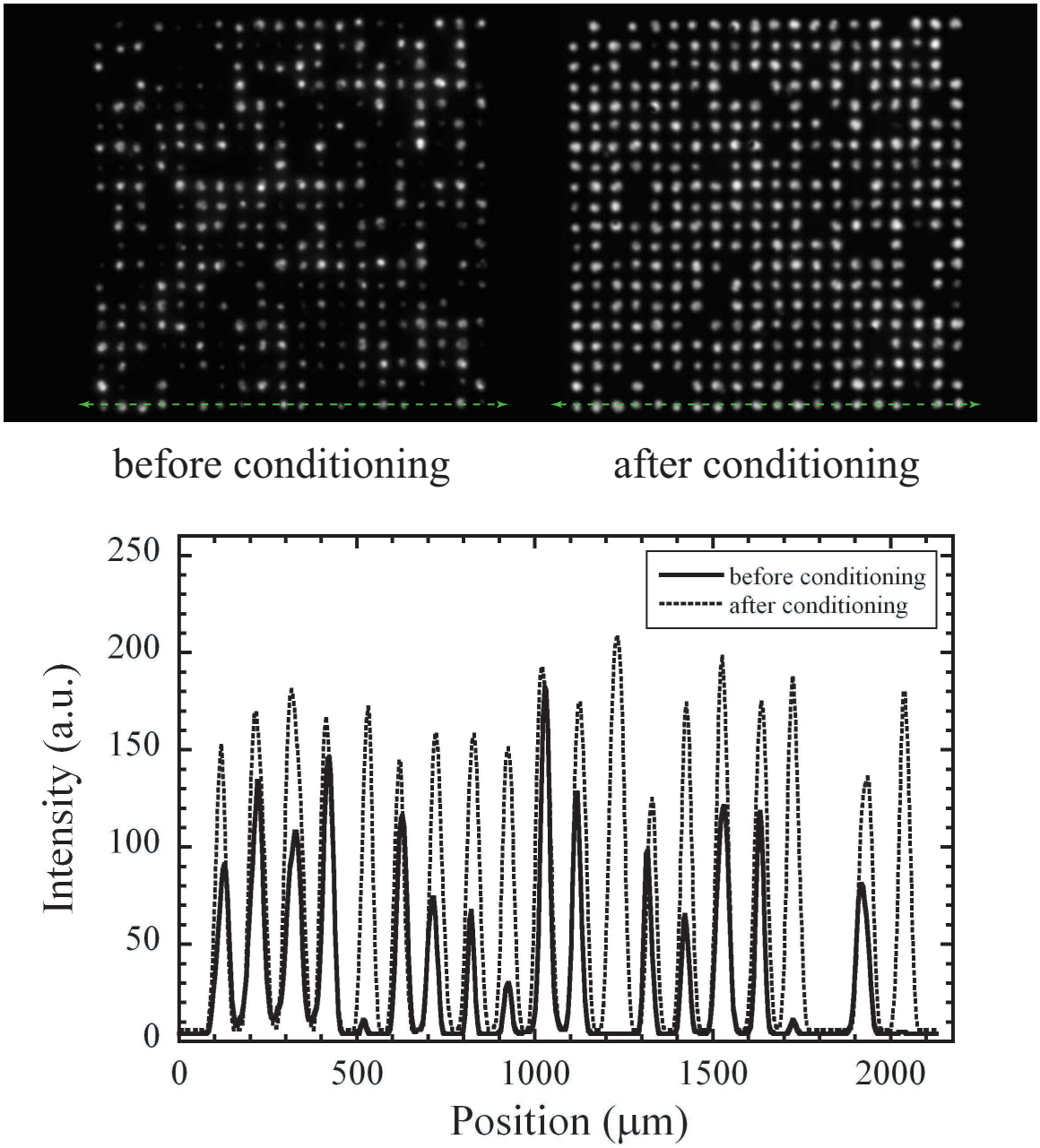

Figure 3.14: Phosphor screen images before and after HCC of a 20x20 DFEA with 5 μm emitter base and 100 μm pitch. The plot demonstrates a linescan of a single row.

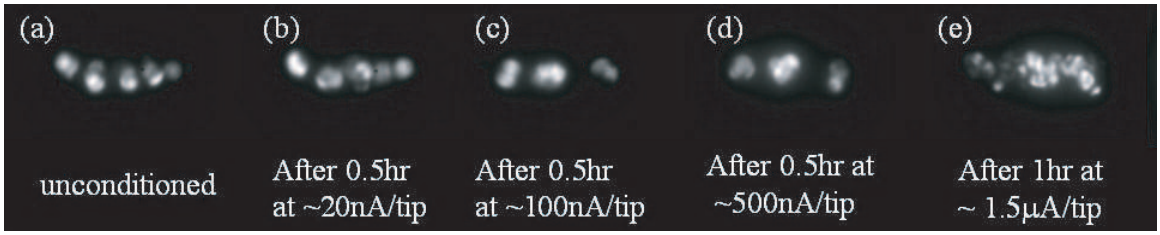

Figure 3.15: HCC progression for a 3×24 ungated DFEA. No emission uniformity changes are noted until an average per-tip current of $\sim 1\ \mu$A.

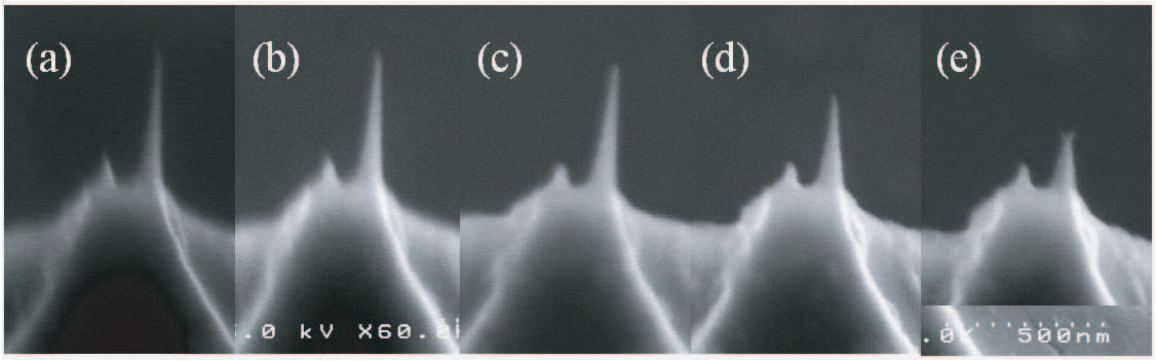

Figure 3.16: Typical morphology evolution of a DFEA emitter during the HCC conditioning process.

emitters. The conditioning procedure follows: An initial image of every emitter in the 72 tip array was taken in an SEM prior to conditioning. An initial uniformity check was made using a Y_2O_3:Eu phosphor anode at a low current level of ~ 10 nA per tip. The array was conditioned with progressively higher per-tip-current levels for half an hour at a time. A polished Molybdenum anode was used during conditioning to minimize back sputtering. Each tip was imaged in the SEM and the emission uniformity was rechecked at ~ 10 nA per tip after each conditioning iteration. No changes in tip morphology or emission uniformity are noted until the per-tip current (current divided by the total number of tips, not by the total number of actively emitting tips) reached levels of $\sim 1\ \mu$A. The progression of emission uniformity and an example of the corresponding morphology changes are shown in Figure 3.15 and Figure 3.16 respectively. Examination of the Molybdenum anode and the cathode surface after operation at the highest current levels showed evidence of small amounts of material transfer. The sputtered material was distributed rather uniformly

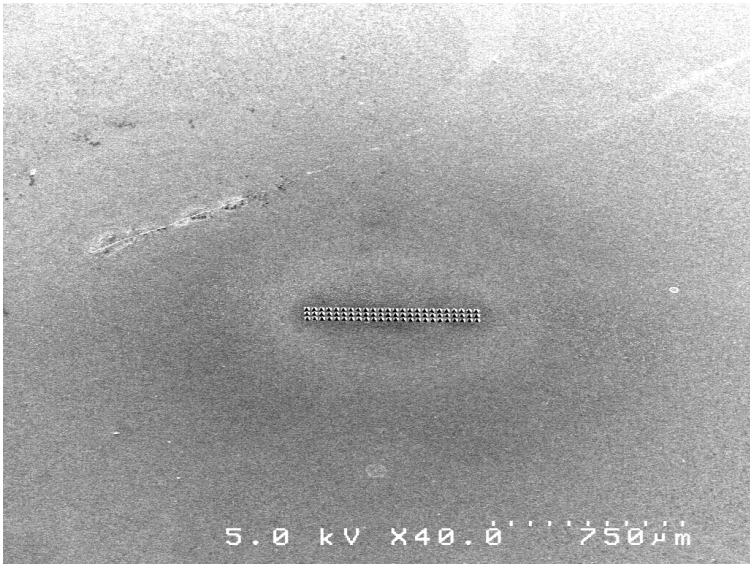

Figure 3.17: Roughly uniform distribution of back-sputtered anode material on the cathode surface following moderate current operation.

over the cathode's active area as seen in Figure 3.17. Examination of the evolution of tip morphology has not conclusively ruled out anode back bombardment as a contributing factor in HCC. However, it is difficult to understand how back bombardment with a roughly uniform spatial distribution could discriminately condition tips based on emission level. Microsecond pulsing of the emission will prevent anode sublimation and should help determine the source of HCC.

Another type of morphological modification was noted during these conditioning studies; nanotip deformation under the stress of the applied electric field was observed. This effect provides a self healing mechanism for certain fabrication or post-processing defects. Figure 3.18 shows the conditioning progression (left to right) for two such defects. Tips that were initially bent at extreme angles to the pyramid's central axis deformed to align with the direction of the macroscopic electric field. Additionally, in some cases double-tips that were stuck together separated. The importance of self-Joule heating to these field-forming effects is not currently known.

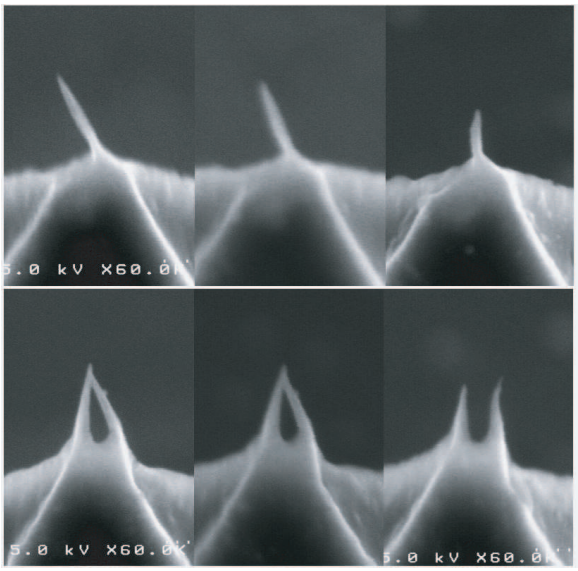

Figure 3.18: Self correction of fabrication and post-processing defects during HCC. The top and bottom are separate tips, and the conditioning progression moves left to right.

III.3 **Future Conditioning Experiments**

The most significant problem with high-current density DC operation of DFEAs in close-diode arrangements is anode back bombardment. This is best illustrated by Figure 3.19. Observations includes catastrophic tip damage and deposition of large particulate matter, $\sim 100\ \mathrm{nm}$ in size. The estimated power density incident on the phosphor anode in this case was $\sim 600\ \mathrm{W/cm^2}$. For a 4 μm pitch array, a per-tip current of 15 μA, and a beam energy of 1.5 kV, the input power density at the anode is $\sim 100\ \mathrm{kW/cm^2}$. This is two orders of magnitude higher than the power densities typically used for sputtering refractory metals. Obviously close-diode DC operation is not possible at these levels, however pulsing the current at microsecond time scales can avoid anode destruction and allow HCC of dense arrays. While the maximum DC current achieved thus far is 15 μA per tip, this is certainly a limitation of the anode and not the cathode. Microsecond pulsing and the resulting removal of anode back bombardment should unlock new levels of performance for DFEAs.

Recently, preliminary experiments on pulsed conditioning of DFEAs have been

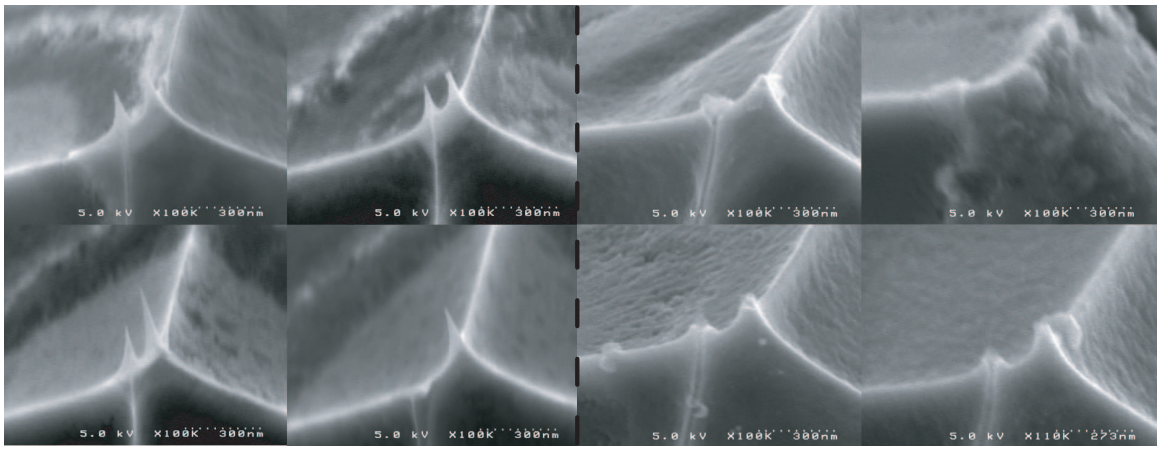

Figure 3.19: Tips from a 28 μm pitch 5×5 ungated DFEA before (four tips on left) and after (four tips on right) HCC and back bombardment damage. The before and after pictures are not of the same emitters, but are representative of the array.

performed in the Department of Electrical and Computer Engineering at Vanderbilt [32]. A Magnavolt (5 kV, 5 A) pulser has been used to test high density, large area arrays in a close-diode configuration. These cathodes have been successfully conditioned with pulsed operation at 1 kHz with a 1% duty factor (10 μs pulses). As expected, HCC procedures are still valid in this regime of operation. The reduced average power density at the anode has prevented back bombardment and facilitated the achievement of peak per-tip currents in excess of 40 μA. This result was from a 224×224 array of 10 μm base emitters with a 20 μm pitch. The corresponding peak current density was then $\sim$ 10 $\mathrm{A/cm^2}$. When scaled for our highest packing density, 4 μm pitch, the current density is $\sim$ 250 $\mathrm{A/cm^2}$. Testing at higher currents was not attempted as the particular cathodes in question were slated for delivery to collaborators. Subsequent tests will explore the maximum achievable currents for single emitters under pulsed operation.

The problem of back bombardment during DC operation becomes less important for a gated device. The high fields required for emission are provided by a low voltage and the gate electrode's close proximity to the emitter, not by the high voltage of a distant electrode. This provides significant flexibility in the physical geometry of the collector system, and

enables minimization of back bombardment. Furthermore, the gate electrode can easily be pulsed near ground and requires very little current. It is anticipated that HCC procedures will be equally effective with gated devices. Ultimately DFEAs will be integrated into environments where anode back bombardment is not present. RF guns do not require an anode to establish the accelerating field and high-voltage DC guns have relaxed physical dimensions which allow extraction of the electron beam.

CHAPTER IV

EMITTANCE AND BRIGHTNESS OF DFEAS

IV.1 Emittance and Brightness

In examining the properties of beams, it is useful to introduce the concepts of trace space and distribution moments. Each beam particle has a trajectory given by $\left(\mathbf{x}_i, \mathbf{x}_i' = \frac{d\mathbf{x}_i}{dz}\right)$, where $\mathbf{x}_i = x_i\hat{\mathbf{x}} + y_i\hat{\mathbf{y}}$ is the transverse position of the i^{th} particle. A coordinate space representation of a beam ensemble at a focus is given in Figure 4.1. To visualize the collective behavior of the beam it is useful to plot these trajectories in so-called trace space, where x' or y' is the ordinate and x or y is the abscissa. In trace space the beam ensemble occupies some volume whose shape evolves as the beam propagates through an electron optical system. While these trajectory points are discrete, for sufficiently high particle number the ensemble can be approximated by a smooth distribution, $n\left(x, y, x', y'\right)$. Statistically the beam ensemble is described in terms of moments of its distribution. These moments quantify observables such as beam size, divergence, and correlations between position and divergence. The first moments in x and x' vanish about the beam axis, and the

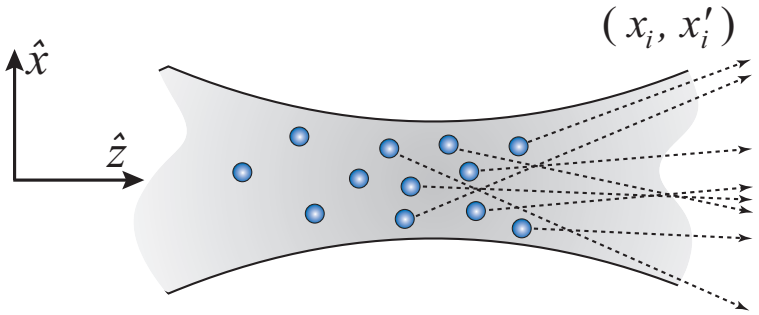

Figure 4.1: Electron trajectories inside the beam envelope at a focus.

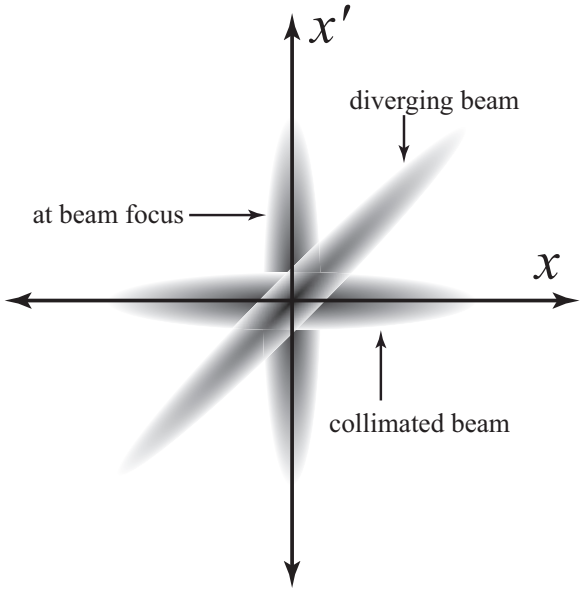

Figure 4.2: (x, x') Three trace space projections: at a beam focus, when the beam is diverging, and when the beam is collimated

second moments in x and x'

$$\sigma_x^2 = \langle x^2 \rangle = \frac{1}{N} \sum_i^N x_i^2 = \iint x^2 n\left(x, x'\right) dx dx' \tag{4.1}$$

$$\sigma_{x'}^2 = \langle x'^2 \rangle = \frac{1}{N} \sum_i^N x_i'^2 = \iint x'^2 n\left(x, x'\right) dx dx', \tag{4.2}$$

give the rms beam size, σ_x, and the rms angular divergence, $\sigma_{x'}$. The correlation moment $\langle xx' \rangle$ indicates whether an electron's transverse position is related to its angular divergence. Figure 4.2 demonstrates three (x, x') trace space projections: at a beam focus, when the beam is diverging, and when the beam is collimated. We may use these distribution moments describe the quality of an electron beam by introducing a quantity called the rms emittance, which is given by

$$\epsilon_x = \sqrt{\langle x^2 \rangle \langle x'^2 \rangle - \langle xx' \rangle^2}. \tag{4.3}$$

Emittance depends on the inherent angular spread that exists at each transverse position in the beam. If we examine 4.3, it is apparent that beam quality does not suffer from the presence of correlations. This is because correlations can be introduced and removed by drift spaces and linear focusing optics. Furthermore, for an ideal beam, all correlations vanish at a beam focus. In this case equation 4.3 reduces to

$$\epsilon_x = \sigma_x \sigma_{x'}. \tag{4.4}$$

It is also common to consider the beam in phase space, where the coordinates use transverse momenta rather than divergence. At any point in phase space the beam ensemble has a density of $\rho(\mathbf{x}, \mathbf{p}, t)$ and a corresponding velocity $\mathbf{v} = (\dot{\mathbf{x}}, \dot{\mathbf{p}})$. Assuming that the number of particles in the beam in conserved, the continuity equation is

$$\rho \nabla \cdot \mathbf{v} + \mathbf{v} \cdot \nabla \rho + \frac{\partial \rho}{\partial t} = 0, \tag{4.5}$$

where ∇ is the phase space gradient. If all forces in the system are derivable from a Hamiltonian, then Hamilton's canonical equations of motion may be substituted into equation 4.5, causing the first term to vanish. The two remaining terms are recognized as the total time derivative of the phase space density

$$\frac{df}{dt} = \mathbf{v} \cdot \nabla \rho + \frac{\partial \rho}{\partial t} = 0. \tag{4.6}$$

This is known as Liouville's theorem [33], and it states that the local density of the beam ensemble in phase space, as viewed while moving with a particle, is constant in time. Liouville's theorem is a statement about density conservation in $6N$-dimensional phase space, where N is the number of electrons in the ensemble. However, if the electrons can be regarded as non-interacting, and the space-charge forces are approximated as an external field applied to all electrons, then Liouville's theorem may be applied to 6-D phase space.

When the beam electrons undergo acceleration, the rms emittance we have described is not constant. Consider the slope of an electron trajectory in the paraxial approximation

$$x' = \frac{dx}{dz} = \frac{p_x}{p_z}, \tag{4.7}$$

where p_x and p_z are the momenta in the x and z directions respectively. When the electron is accelerated in the z direction, p_z changes while p_x remains constant. This raises or lowers the divergence of every electron in the beam, effectively changing the volume occupied in trace space. A more useful parameter that is invariant under accelerations is the normalized emittance, given by [34]

$$\epsilon_{N_x} = \beta\gamma\epsilon_x = \frac{1}{m_e c}\sqrt{\langle x^2\rangle \langle p_x^2\rangle - \langle x p_x\rangle^2}. \tag{4.8}$$

where m_e is the electron mass. As before, when the beam is at a focus, we have

$$\epsilon_{N_x} = \frac{1}{m_e c}\sqrt{\langle x^2\rangle \langle p_x^2\rangle} = \frac{1}{m_e c}\sigma_x \sigma_{p_x}. \tag{4.9}$$

The transverse emittance describes how well a particle beam may be focused. However, it does not involve the intensity of that beam. Another measure of beam quality is the amount of current that lies within a given trace-space volume. This differential quantity, mentioned in Chapter 1, is called the transverse brightness and is simply the local current density in 4-D transverse trace space. As with emittance, the brightness has a normalized version that is invariant under accelerations. This normalized transverse brightness is given by

$$B_N = \frac{1}{\beta^2\gamma^2}\frac{d^4 I}{dx dx' dy dy'}, \tag{4.10}$$

or equivalently, in phase space variables

$$B_N = m^2 c^2 \frac{d^4 I}{dx dp_x dy dp_y}. \tag{4.11}$$

For convenience, an average brightness is typically used in which the total current is divided by the approximate 4-D trace space volume occupied by the beam ensemble,

$$B_N = \frac{1}{\beta^2\gamma^2}\frac{I}{\Delta V_{xx'yy'}} = m^2c^2\frac{I}{\Delta V_{xp_xyp_y}}. \tag{4.12}$$

IV.2 **Experimental Arrangement and Results**

There are two primary techniques for determining the emittance of an electron beam. The first technique determines only the emittance rather than the details of the trace space projection. The electron beam is focused by an optical system, and the beam envelope is determined as a function of the distance along the beam axis, for example, by scanning a phosphor screen or a wire scanner along the length of the electron beam. This measured envelope is compared to envelope equation, using the emittance as a fitting parameter. Alternatively, the beam profile can be measured at a single point while scanning the strength of a focusing solenoid. An example of this technique applied to the beam from an FEA is given in [7].

The other method of emittance measurement involves sampling the electron beam at various transverse positions and examining the angular spread emanating from each point. This constructs a map of the density in transverse trace or phase space. This is commonly refered to as a pepperpot technique and utilizes masks consisting of either pinholes or slits. In the case of a slit array, the beam divergence is sampled in a single transverse dimension, whereas a pinhole array examines both transverse dimensions simultaneously. After passing through the aperture mask, the beamlets enter a field-free drift space where their angular spread is translated into a transverse position spread. The beamlets are examined after this drift using a phosphor screen and CCD camera. The aperture mask parameters and the length of the drift space are such that the beamlets are well correlated at the phosphor but do not have significant overlap with one another. A schematic of

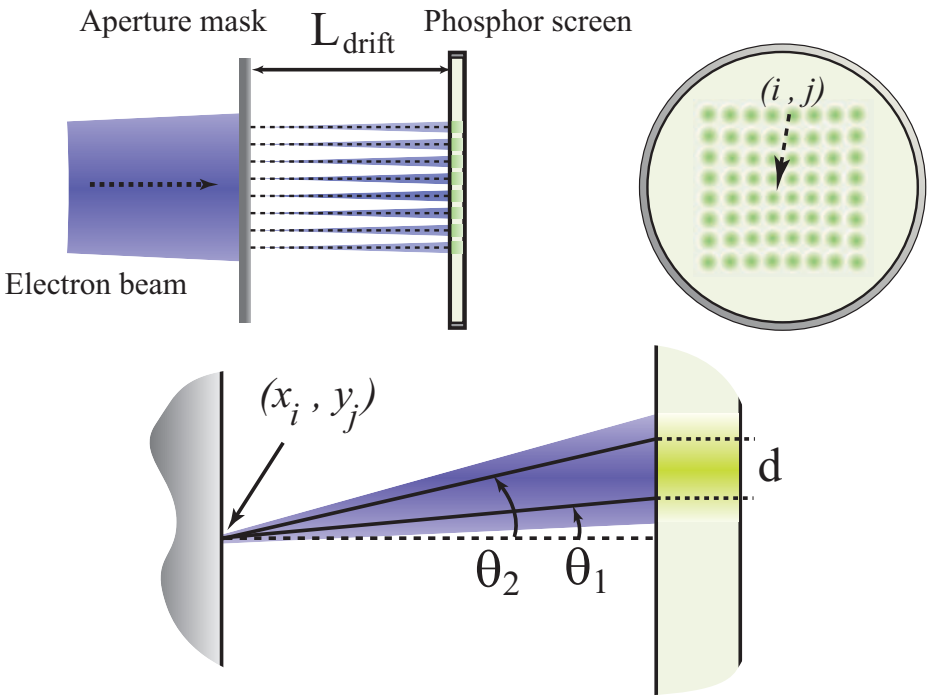

Figure 4.3: The pepperpot technique of determining an electron beam's trace space distribution.

this technique and the resulting trace-space distribution are seen in Figures 4.3 and 4.4 respectively.

For our case of a DFEA cathode, the capability for a high degree of emission uniformity over a large physical area has been demonstrated. Therefore, we simplify the process by measuring the beamlet emitted by a single pinhole and then assuming that the same result is obtained irrespective of transverse position in the beam. An ungated, 3×24, 28 μm pitch, diamond field-emitter array (Figure 4.5) is placed in a close-diode configuration with a pepperpot as the primary anode The experimental arrangement is shown in Figure 4.6. The anode-cathode gap is set using precision quartz capillaries, 330 μm in diameter. When the thickness of the diamond film is included, the gap is $\sim$ 300 μm. In this configuration, fields up to $\sim$ 17 V/μm can be applied. The pepperpot (Figure 4.7)is fabricated from a single SOI wafer, using a multistage patterning and etching process, and has 30-μm square holes with a 200-μm pitch. A field-free-drift space of 5 mm is set with a cylindrical

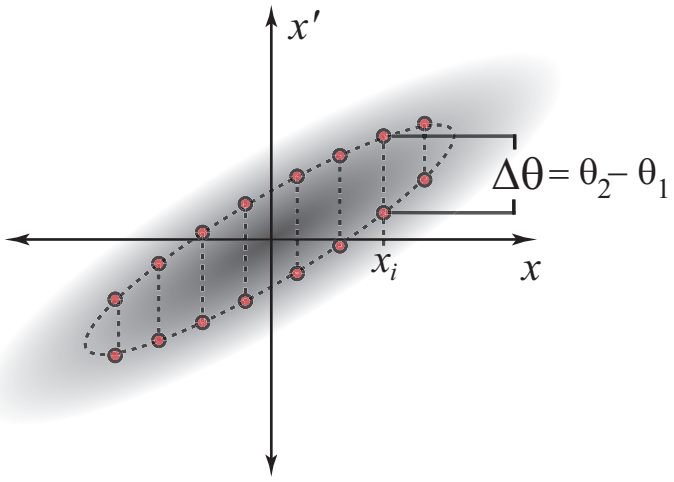

Figure 4.4: The (x, x') trace space distribution obtained using a pepperpot technique

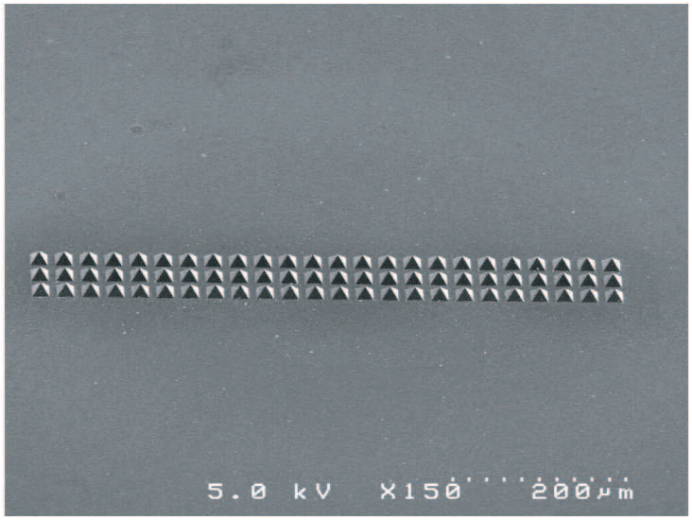

Figure 4.5: 3×24, 28 μm pitch, ungated DFEA used in preliminary emittance measurements.

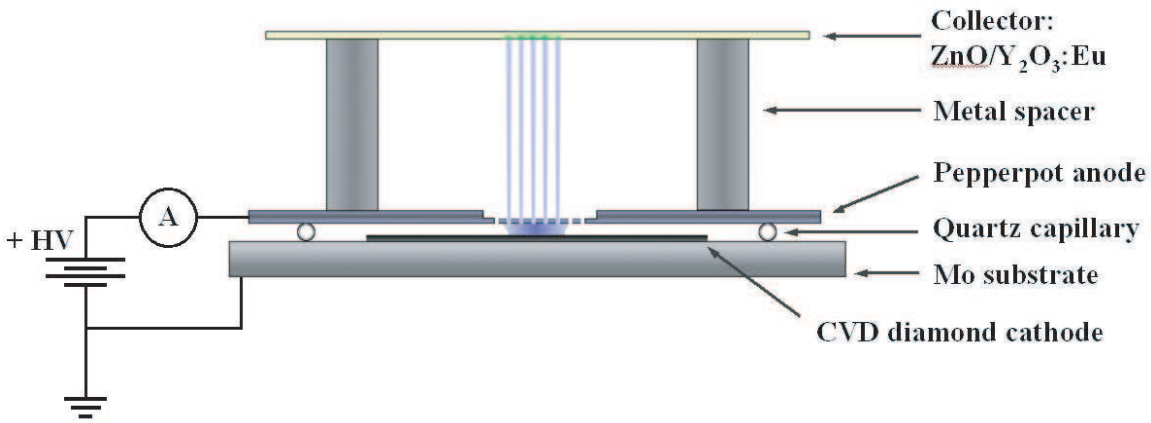

Figure 4.6: The experimental arrangement for emittance measurements with DFEAs.

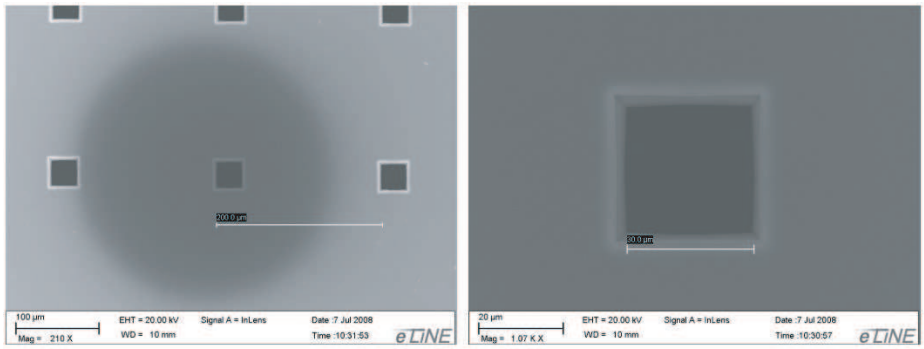

Figure 4.7: SEM micrographs of the pepperpot used in preliminary emittance measurements.

metal spacer and terminates at a high-sensitivity ZnO phophor screen. The apparatus has an integrated resistive heater, allowing annealing of the cathode up to $\sim$ 350 °C. This annealing improves uniformity due to modification of adsorbed species on the emitter surface. In the current experiment, the beamlet that emerges from the pepperpot comprises emission from fewer than a dozen tips. As a result, the beam has nonzero correlations that slightly preserve the aperture's square shape in the final image. Figure 4.8 shows one of the collected beamlets with the approximate location of a linescan that is used to estimate the cathode's rms angular divergence. The sporadic bright spots in the image are the result of phosphor damage from unrelated experiments. The results of the linescan are presented in Figure 4.9. The rms radius of the beamlet at the screen is estimated at approximately 250

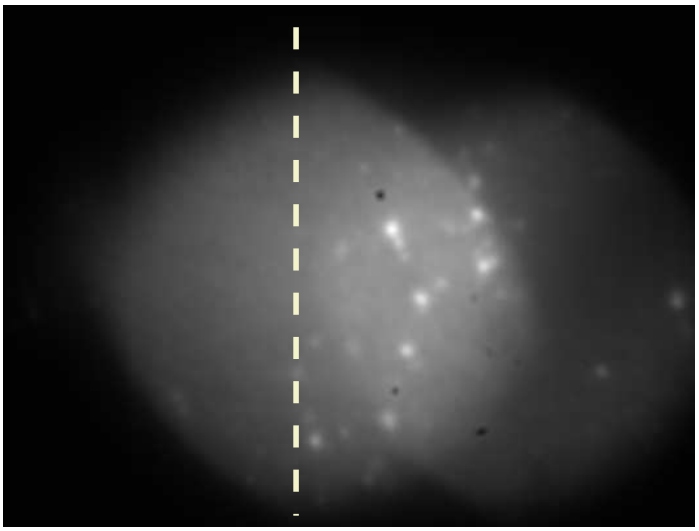

Figure 4.8: Phosphor screen image of a beamlet during an emittance measurement. The line overlay gives the approximate location of the linescan used to calculate the angular divergence.

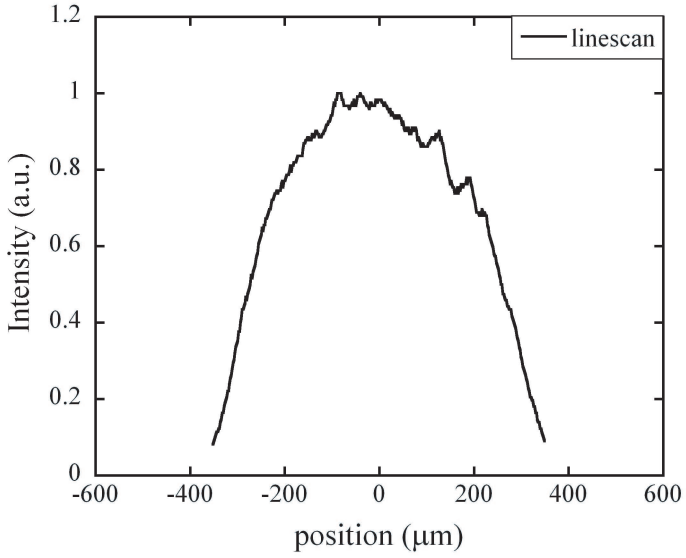

Figure 4.9: This linescan of the beamlet gives an approximate rms radius of 250 μm, corresponding to an rms angular divergence of $\sim$ 38 mrad before aperture defocusing.

μm, which corresponds to an rms angular divergence of $\sigma_{x'} \approx 50$ mrad. The fields around a pepperpot aperture act as a diverging lens and increase the measured divergence at the collector. The focal length of the effective diverging lens is given by $f = 4L$, where L is the anode-cathode spacing. Correcting for the focal length of 1.2 mm reduces the measured rms angular divergence to $\sigma_{x'} \approx 38$ mrad. For a beam energy of 2 kV ($\beta\gamma \approx 0.09$) and a cathode size of $d = 1$ mm, the normalized x-emittance is

$$\epsilon_{N_x} = \beta\gamma\sigma_x\sigma_{x'} = 0.97 \text{ mm} \cdot \text{mrad} \tag{4.13}$$

Assuming spatial uniformity, and identical Gaussian distributions in x and y, the effective trace space volume occupied by a beam with this divergence is [35]

$$\Delta V = 2\pi\sigma_{x'}^2 d^2. \tag{4.14}$$

We may then calculate the normalized brightness 4.12 as a function of current density (A/m^2),

$$B_N = \frac{1}{\beta^2\gamma^2}\frac{J}{2\pi\sigma_{x'}^2}. \tag{4.15}$$

For the highest per-tip currents and tip densities produced thus far, the current density averaged over the area of the array is $J \approx 2.5 \times 10^6$ A/m^2, and the normalized transverse brightness is $B_N \approx 3.5 \times 10^{10}$ A/m$^2 \cdot$ steradian. With the successful development of pulsed conditioning techniques, high-density (4-μm pitch) arrays are now available for emittance testing. This represents an increase in tip density of $>$30 times compared with the present results, and will significantly refine these measurements.

IV.3 **Simulation of Single Tip Emission for Estimating Array Emittance**

For comparison with our experimental results, we have performed simulations of the beamlet from an individual emitter. Field solving for the emitter structure is carried out in POISSON while electron beam trajectories are computed in General Particle Tracer (GPT).

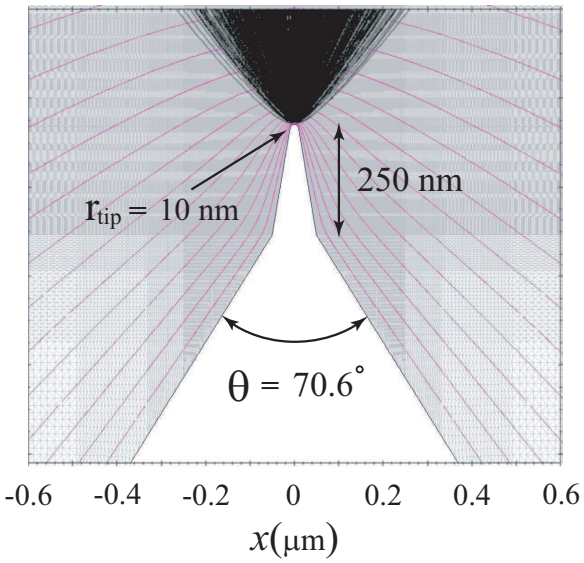

Figure 4.10: Detail of an individual emitters nanotip structure with field solving mesh and trajectories.

These simulations are axially symmetric and cannot emulate the pyramidal geometry of the actual emitters or the double tips sometimes observed. The anode-cathode gap is 300 μm, taking into account the thickness of the diamond layer, and the applied voltage is 2 kV. The electron beam is started at the surface of the emitter nanotip and is given Gaussian distributions in velocity transverse to the surface normal, and transverse position. The rms radius for the transverse velocity distribution, $\beta = 10^{-3}$, was determined using preliminary energy spread measurements of the field emitted beam from a cvd-diamond film. These early measurements suggest a FWHM energy spread of 1.3 eV. A close up view of the emitter's nanotip, electron trajectories, and field solving mesh are seen in Figure 4.10. Figure 4.11 demonstrates propagation of the beam to the pepperpot position, and details of the electron trajectories near the emitter surface are shown in Figure 4.12. The beam's transverse profile and (x, x') trace space projection are shown in Figures 4.13 and 4.14 respectively. The calculated beam spot of $\sim$ 50 μm is comparable to that measured in uniformity conditioning experiments, and the rms divergence at the pepperpot position is $\sim$ 40 mrad, which agrees well with the measured value of 38 mrad.

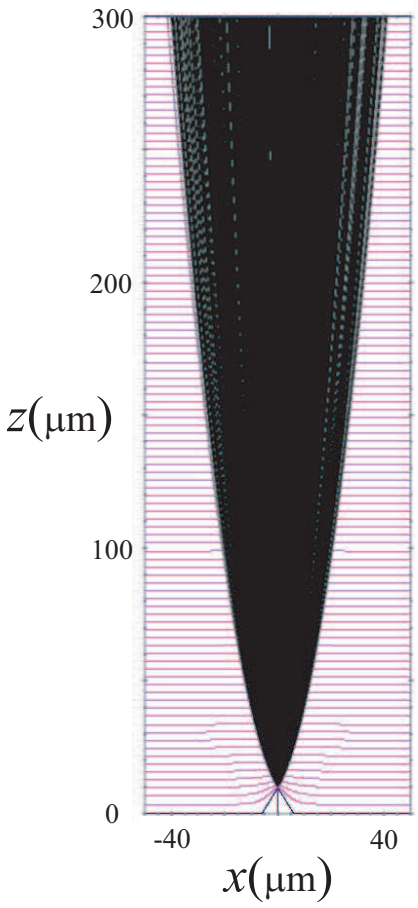

Figure 4.11: Propagation of beamlet to the pepperpot position.

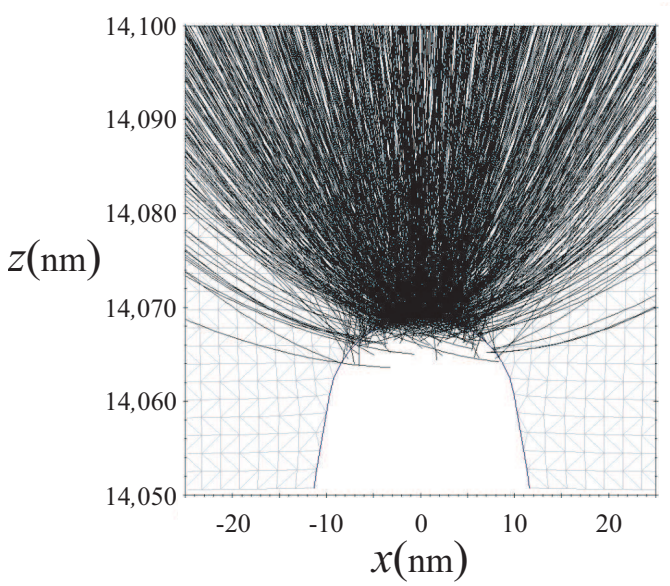

Figure 4.12: Detail of the electron trajectories near the nanotip surface. Some spurious trajectories are present due to imperfect matching of the electric field map to the tip geometry

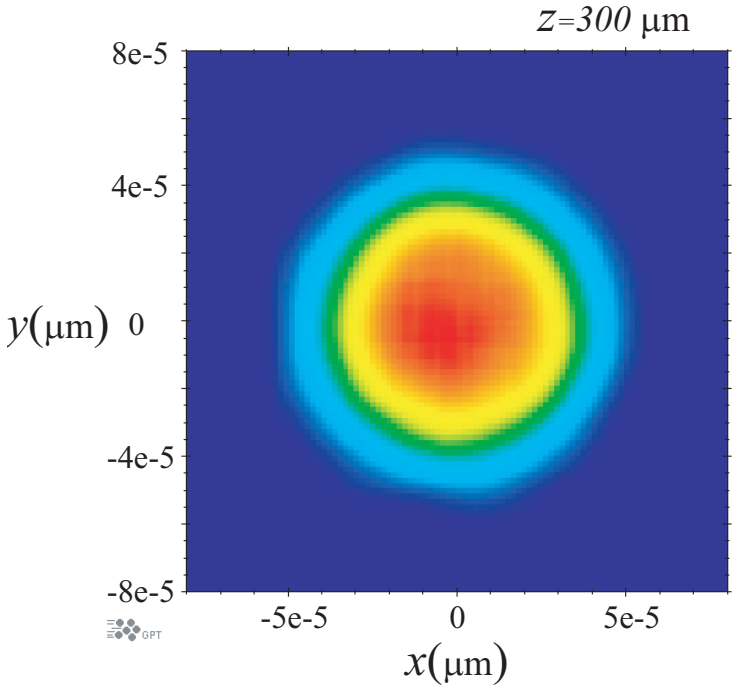

Figure 4.13: Electron beam's transverse profile at the pepperpot anode.

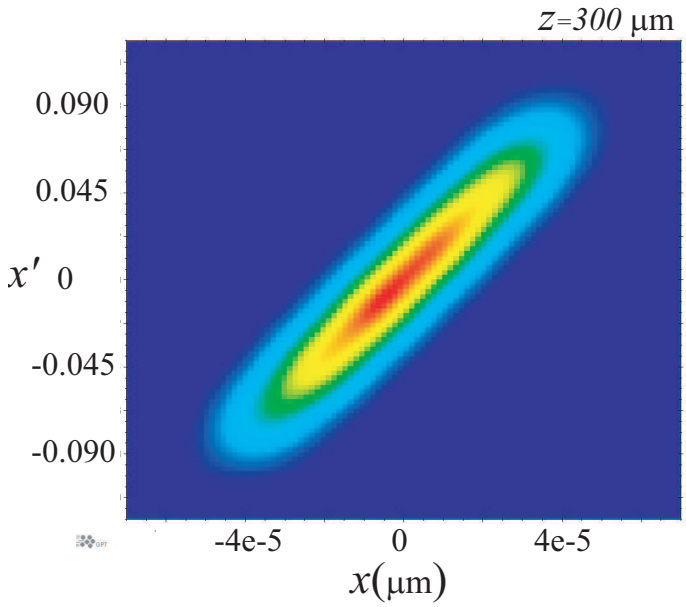

Figure 4.14: (x, x') trace space projection of the electron beam at the pepperpot anode.

CHAPTER V

ENERGY SPECTRUM FROM DFEAS

V.1 Introduction

The name ”diamond field-emitter array” does not hint at the complexity of the emitter material in these devices. The nanodiamond that constitutes the emitter surface consists of sp^3 crystals with interstitial sp^2 and varying levels of incorporated Nitrogen and Boron. Furthermore, the bulk of the emitter's internal structure is large grain microdiamond. Details of the emitter's nanotip structure and chemical composition are slated for investigation with TEM and other techniques in the near future [36]. There is perhaps little reason to believe that these diamond structures should behave as either pure metal or semiconductor field emitters. While Fowler-Nordheim like emission has been demonstrated, a full picture of the emission physics cannot be derived from these data. From a fundamental perspective, perhaps the most illuminating measurement that can be made is that of the emitted energy spectrum from DFEAs. The energy spectrum emitted from a clean nanodiamond surface can give insight into its density of states near the Fermi level, while the spectrum from adsorbed molecules and atoms can aid in the understanding of resonant tunneling effects between the nanodiamond and the surface states due to those adsorbates.

V.2 Energy Analyzer Design, Simulation, and Testing

To measure the emitted energy spectrum we have developed a high-resolution retardation energy analyzer based on previous work at [37]. The measured energy spread in a standard retardation analyzer is artificially high due to trajectories having nonzero transverse momentum. By including a cylindrical focusing electrode, the energy resolution can be improved by several orders of magnitude. A schematic of the analyzer accompanied

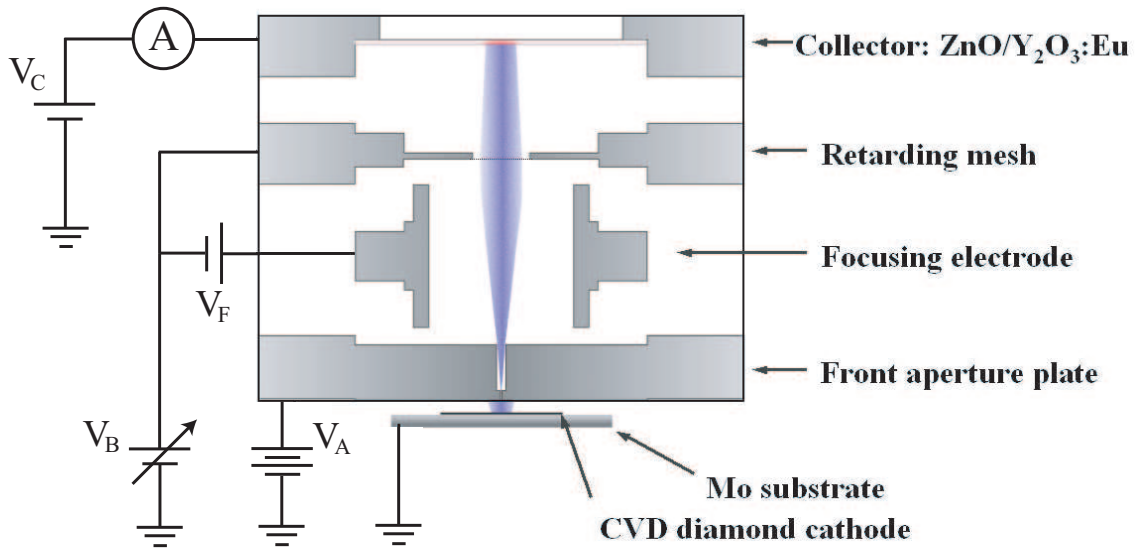

Figure 5.1: High-resolution retardation energy analyzer schematic (with cathode).

by a cathode is shown in Figure 5.1. The system was modeled in SIMION 7.0, an ion/electron optics workbench, in order to predict performance of the analyzer. An isometric-cutaway view of the analyzer is shown in Figure 5.2. To find the achievable energy resolution, we provide the analyzer with a monoenergetic beam having a 5° correlated-full-angle spread. Prior to energy scans, the focusing electrode is adjusted until the electron trajectories are normal to the retarding mesh. Alternatively, the measured energy spread may be minimized as a function of focusing voltage as seen in Figure 5.3. Operating the analyzer at this minimum provides resolution that is smaller than the kinetic-energy error in the simulation. The optimum focusing voltage is found to be $V_{focus} = 0.97V_{beam}$. Figure 5.4 shows the integrated collector signal as a function of retardation voltage for beams of different energies. The error as a fraction of the total beam energy is 10 ppm, 10 mV for a 1 kV beam. Equipotentials and trajectories for an energy scan of a 1 kV beam with $V_{focus} = 970$ V are presented in Figure 5.5.

These simulations demonstrate that the idealized geometry of this analyzer is capable

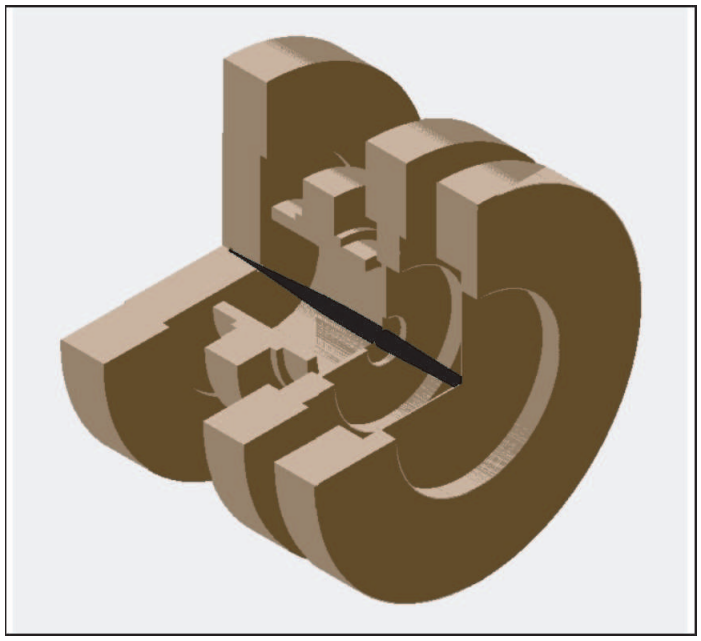

Figure 5.2: Cutaway view of the energy analyzer with electron beam. Simulation geometry by C. L. Stewart.

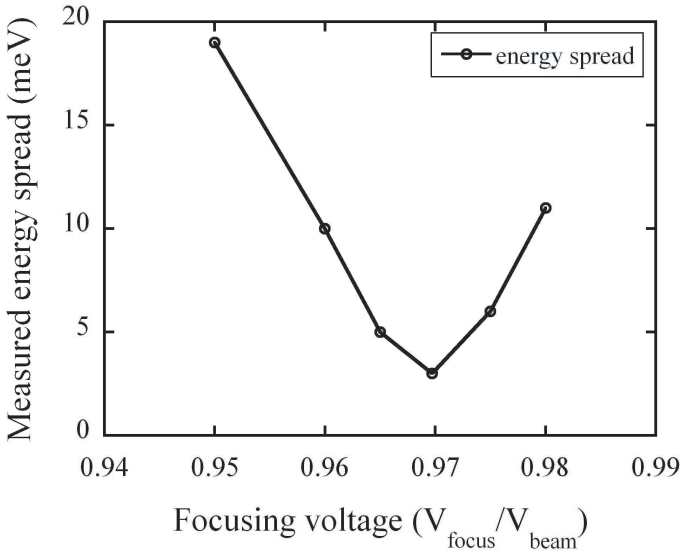

Figure 5.3: Measured energy spread (due to KE error) as a function of focusing voltage. Simulations by C. L. Stewart.

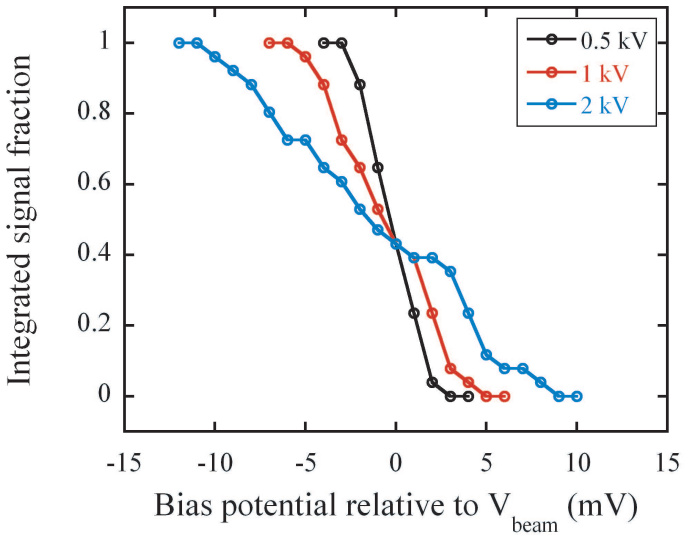

Figure 5.4: Integrated energy distributions for three different beam energies. The focusing is set to optimum for each scan. Simulations by C. L. Stewart.

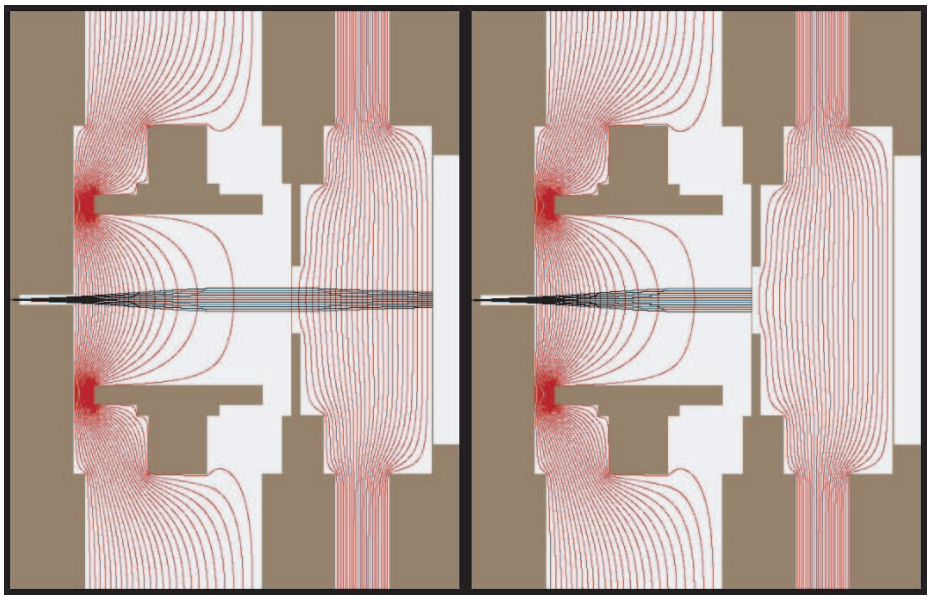

Figure 5.5: Trajectories and equipotentials inside the energy analyzer during a scan.

of very high resolution, however, effects that are excluded from these simulations, such as retarding mesh granularity, are found to have a significant impact on the achievable resolution. Because the emission spectrum from these diamond cathodes has never been measured before, care must be taken to investigate the instrumental broadening due to these non-idealities.

An excellent treatment of a retardation analyzer's broadening function and its deconvolution from experimentally measured energy spectra is given by Reifenberger, Goldberg, and Lee [38]. The measured total energy distribution distribution j_e' is the result of sweeping the analyzer's resolution function T' across the unknown true distribution, j_0'. The measured energy distribution is then given by the convolution

$$j_e'(\epsilon_m) = \int_{-\infty}^{\infty} j_0'(\epsilon)\, T'(\epsilon_m - \epsilon)\, d\epsilon \tag{5.1}$$

where ϵ_m is the mesh potential relative to the Fermi energy. Using the Faltung theorem to deconvolve these functions into their Fourier transforms, we have

$$\tilde{j_e}'(\omega) = \tilde{j_0}'(\omega)\, \tilde{T}'(\omega)\,, \tag{5.2}$$

where

$$\tilde{j_e}'(\omega) = \frac{1}{\sqrt{2\pi}} \int_{-\infty}^{\infty} j_e'(\epsilon)\, e^{i\omega\epsilon} d\epsilon \tag{5.3}$$

If the true energy distribution, $j_0'(\epsilon)$, is known, then the resolution function of the analyzer can be found by

$$T'(\epsilon) = \frac{1}{\sqrt{2\pi}} \int_{-\infty}^{\infty} \frac{\tilde{j_e}'(\omega)}{\tilde{j_0}'(\omega)} e^{-i\omega\epsilon} d\omega. \tag{5.4}$$

If the assumed Fermi energy in the calculation of the resolution function is different from the actual Fermi energy, this exact difference is revealed as a shift in the resolution function from the origin. In this way the Fermi energy can be accurately determined for a given distribution, provided the shape of the theoretical distribution is known. When calculating

the resolution function, high-frequency noise components in the experimentally measured spectra can complicate matters. The effects of this noise may be mitigated in frequency space by applying a Gaussian filter,

$$\tilde{G}(\omega) = e^{-\omega^2/2\alpha^2} \tag{5.5}$$

to the experimental distribution. The parameter α determines the extent of the high-frequency damping and typically $\alpha \approx 30\ \mathrm{eV}^{-1}$. Once the resolution function or its Fourier transform is calculated, it may be deconvolved from measured spectra to yield the corrected distribution

$$j_c'(\epsilon) = \frac{1}{2\pi}\int_{-\infty}^{\infty} \frac{\tilde{G}(\omega)\,\tilde{j_e}'(\omega)}{\tilde{T}'(\omega)} e^{-i\omega\epsilon} d\omega. \tag{5.6}$$

Thermionic cathodes have a simple and well known energy spectrum that can be used to extract the resolution function. When emission occurs far from the Fermi level and the density of states is locally uniform, ingnoring normalization constants, the theoretical total-energy distribution for a thermionic emitter has the form

$$j'(\epsilon) = \epsilon\, e^{-\epsilon/k_B T}, \tag{5.7}$$

where T is the emitter temperature. The Fourier transform of (5.7) is straightforward, and given by

$$\tilde{j_0'}(\omega) = \frac{1}{\sqrt{2\pi}}\left[\frac{1}{k_B T} - i\omega\right]^{-2}. \tag{5.8}$$

Substituting into (5.4), we have

$$T'(\epsilon) = \frac{1}{\sqrt{2\pi}}\int_{-\infty}^{\infty}\int_{-\infty}^{\infty}\left[\frac{1}{k_B T} - i\omega\right]^{2} e^{i\omega(\epsilon'-\bar{\epsilon}+\eta)} j_e'(\epsilon')\, d\omega d\epsilon', \tag{5.9}$$

where $\bar{\epsilon} = \epsilon + \eta$, and η is the difference in the assumed and actual Fermi energy.

Our thermionic source of choice is a large area ($\sim$ 1.5 mm diameter) LaB_6 $\langle 100\rangle$ (2.69

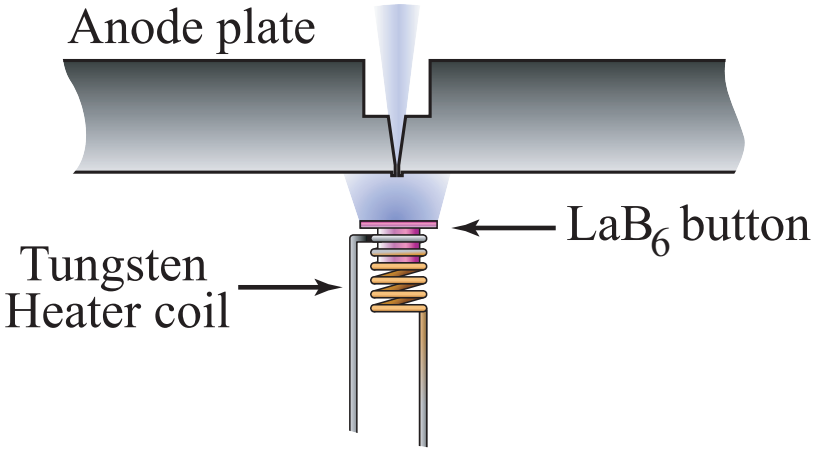

Figure 5.6: Detail of LaB_6 thermionic source and Tungsten heater coil for fiducial testing of the energy analyzer.

eV work function) button cathode. Detail of the experimental arrangement is given in Figure 5.6. Figure 5.7 shows the extracted resolution function for a cathode temperature of $\sim$ 1790 K and a beam energy of 500 V. The resolution function is approximated by a Gaussian least-squares fit with a FWHM of 0.147 eV that is subsequently used to correct measured spectra. The difference in the assumed and actual Fermi energy for this case, is found to be $\eta = 1.705$ eV. The as-measured, theoretical, and corrected spectra are shown in Figure 5.8. While the Gaussian correction sharpens the low energy rise, it does not correct the shift in the peak value's location. This is because the actual resolution function bears a small degree of asymmetry that is not reproduced in the Gaussian. Also, the finite freqency spectrum used in reconstructing the corrected distribution results in ringing on the sharp, low-energy side. In Figure 5.8 this ringing has been truncated at the first zero crossing.

V.3 **Measurement of emitted energy spectrum from DFEAs**

For measurement of the energy spectrum from a DFEA, the cathode and energy analyzer are integrated with the test stand shown in Figure 5.9. The test stand can be operated at UHV pressures and can apply electric fields of up to $\sim$ 25 V/μm. The cathode is held in a miniature vise that is attached to a spring-loaded kinematic mount. This

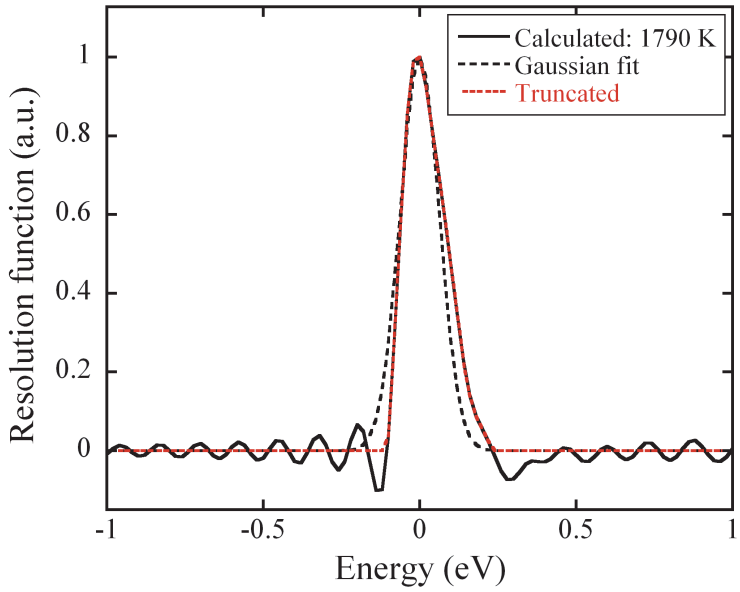

Figure 5.7: The extracted resolution function for the energy analyzer. The Gaussian least-squares fit that will be used for deconvolution of measured spectra is also shown.

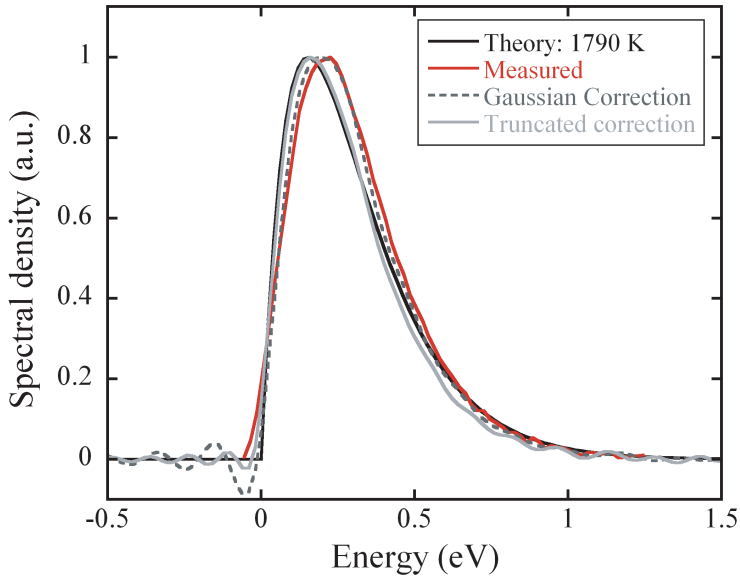

Figure 5.8: As-measured, theoretical, and deconvolved spectra from a 1790 K LaB_6 thermionic emitter. The energy values on the x-axis are given relative to the work function.

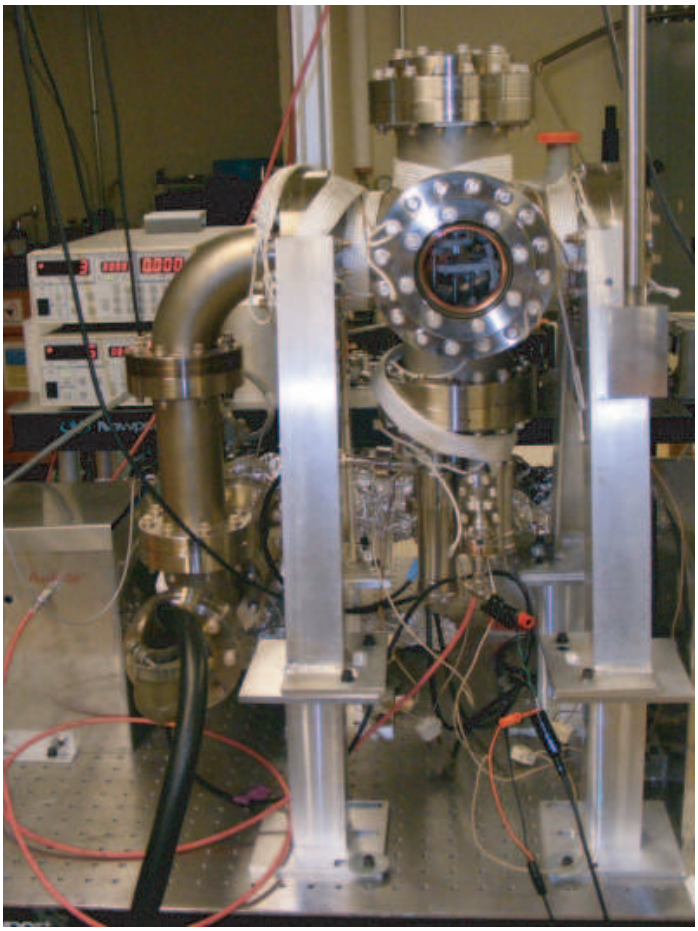

Figure 5.9: General purpose UHV test stand for measuring emission properties of DFEAs.

allows arbitrary adjustment of the planarity of the cathode and analyzer surfaces during HV operation. Additionally, the anode carriage holding the analyzer can be adjusted during operation to change the anode-cathode spacing. The parameters of the DFEA used in these experiments were selected with the following reasoning: The required electric field for moderate current operation is $\sim$ 10 V/μm, which is conveniently produced by a 3 kV anode bias and an anode-cathode gap of 300 μm. In experiments under similar conditions we have observed a beamlet diameter of $\sim$ 80 μm from an individual emitter. The array is then chosen to have a 100-μm pitch and a dimension of 20$\times$20 tips. This guarantees a macroscopic-array size for assisting in alignment of the analyzer. With these dimensions and conditions, roughly 50% of the array area is covered with electron beam at

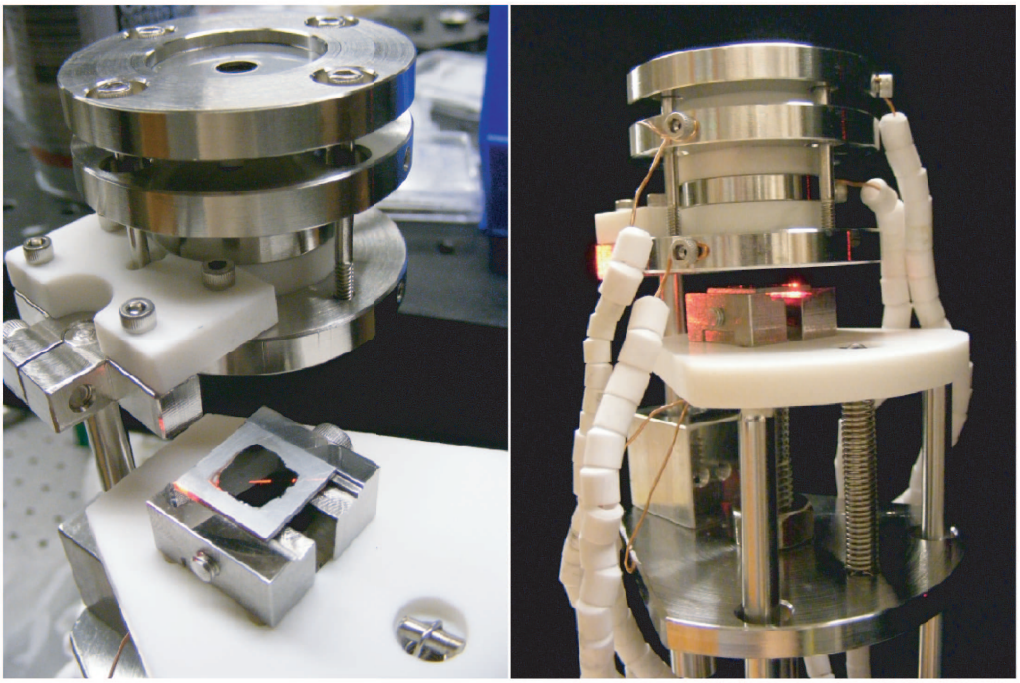

Figure 5.10: 20×20, 100-μm pitch DFEA and energy analyzer in teststand during alignment procedure.

the analyzer's aperture plane. This gives a reasonable probability of successful alignment, and with a front-aperture diameter of 50 μm, a roughly 60% chance that the analyzer will examine current from a single tip.

In these experiments the background pressure ranged from 5×10^{-10} to 2×10^{-9} Torr depending on the emission current level. The first alignment attempt was successful, and beam current was immediately detected at the collector electrode. The analyzer was configured in an observation mode where the accepted beamlet is magnified and allowed to impact the phosphor-screen collector at high energy. In this mode, spatial fluctuations due to adsorbate action can easily be seen. It was clear from these observations that the beam comprised emission from multiple adsorbates. Furthermore, the aperture was completely filled by the beam, suggestive that the accepted beam originated from a single tip. In this configuration, the beam may also be focused near the retarding mesh for fiducial

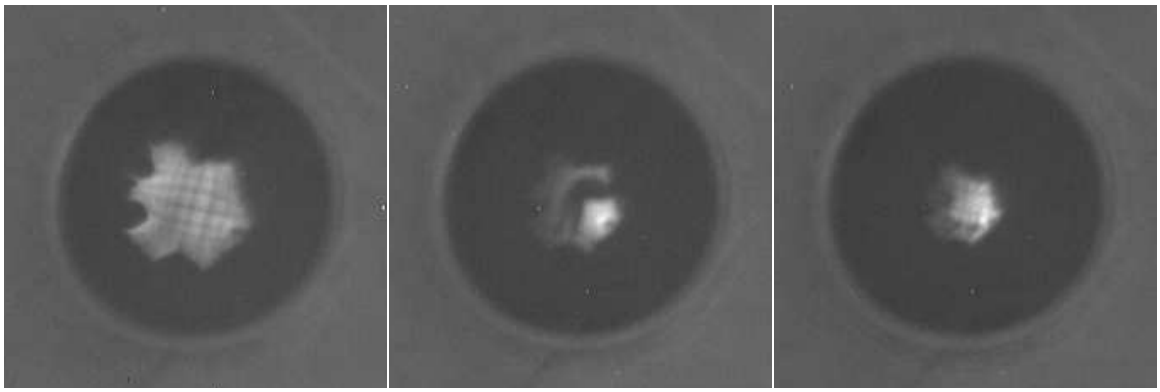

Figure 5.11: Phosphor images produced by focusing the accepted beamlet near the retarding mesh. The 50-μm pitch of the grid can be used for fiducial purposes.

purposes such as estimating the relative importance of spherical and chromatic aberration in the optical system. Figure 5.11 shows the phosphor screen image as the beam focus is longitudinally swept through the retarding mesh. In this case the beam energy was 3 kV, and the retarding mesh and collector were both held at 1.5 kV. When $V_F = -210$ V, the beam was focused directly on the mesh. Although complicated by aberration at the focus, the beam-spot size was estimated at $\sim$ 50-100 μm based on the 50-μm pitch of the mesh. When a monoenergetic beam is used in simulations, then the estimated spot size under these conditions is on the order of a few microns. However, when an energy spread of 1-2 eV is introduced, then the estimated spot size is on the order of many tens of microns. This suggests that spherical aberration in the optical system is unimportant for these beams.

During experiments with the LaB_6 source, the optimum focal setting for energy analysis was found to be 97% of the beam voltage. This focal setting was subsequently used for all DFEA measurements. During these measurements it was very clear if the adsorbate configuration changed during an energy scan. Typically, a given adsorbate configuration would persist for between one and twenty seconds. For a moderate step size of 0.1 V, each scan lasts for approximately 1-3 seconds. As expected, the presence of adsorbates on

the emitter surface has dramatic effects on the spectrum shape and position. Figure 5.12 presents a sampling of the measured spectra. Narrow lines are single spectra (averaged over several scans) taken at different times but under the same experimental conditions, and the thick black and green traces are the measured spectra averaged over $\sim$ 600 scans. Figure 5.13 presents two isolated adsorbate events. The traces are given chronologically from earlier to later times (1,2...). The plot on the right demonstrates the power of adsorbate modification of field emission through resonant tunneling. This was a rapid event in which the current in the accepted beamlet increased by an order of magnitude while maintaining a spectral width of $\sim$ 0.4 eV. The collection of spectra on the left seems to suggest the arrival of an adsorbate on the emitter surface followed by a gradual change in its configuration. For instance, this could correspond to a slow rotation of the adsorbate's molecular axis or a progressive migration to regions of higher field. The presence of adsorbed species on the emitter can create surface states that are resonant with certain electron energies in the emitter's density of states [19, 39]. This resonance can result in order-of-magnitude enhancements of the local tunneling current. Thus, it is anticipated that emission from the clean diamond surface is much weaker than that observed for adsorbed species. Furthermore, the adsorbates tend to shift the peak position of the distribution to lower energies. This suggests that weak spectra with high central energies should be examined as the most likely candidates for origination from a clean emitter surface. In these experiments, spectra with the most energetic peak positions ($\sim$-5.5 eV) have corresponded to the weakest intensities. Figure 5.14 shows unnormalized and normalized versions of these spectra. While some adsorbate modification is observed, it is obvious that all of these distributions share a single spectral feature: a strong peak at a bias of -5.5 V. The black trace appears to be the most likely candidate for emission from a clean surface.

If we ignore normalization factors, the total-energy distribution for thermal-field

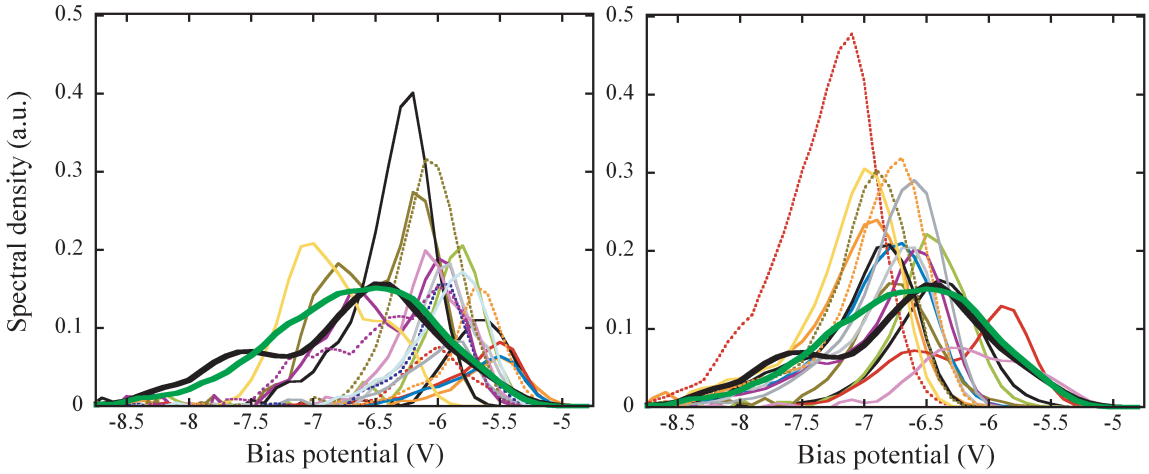

Figure 5.12: Measured emitted energy spectra from a DFEA microtip. Fluctuations in the adsorbate configuration on the emitter surface cause changes in the shape and positions of the spectra. Thin lines are individual spectra and the thick black and green traces are averaged over $\sim$ 600 spectra.

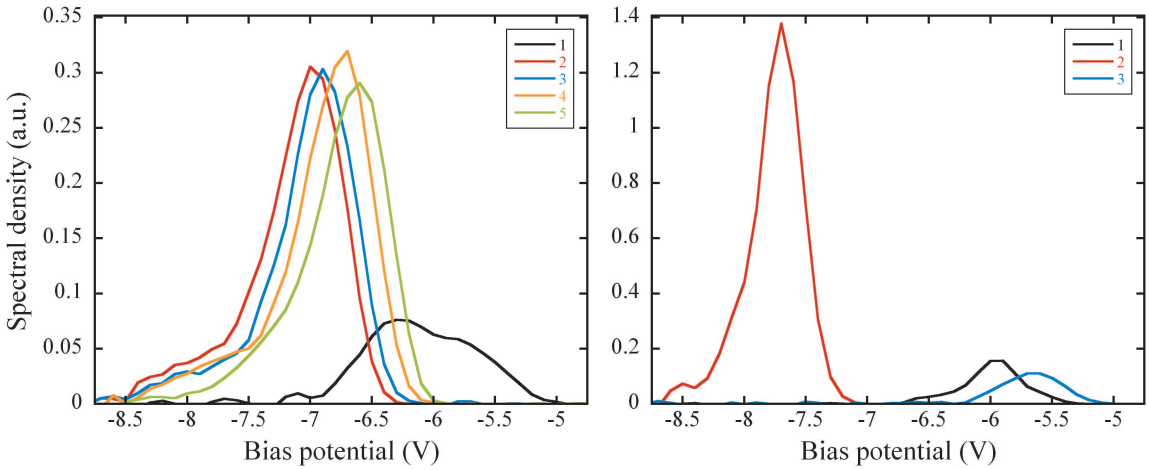

Figure 5.13: Selected adsorbate events; Traces are chronological beginning at the index 1. A significant transition followed by a gradual shifting of the central energy (left). A discrete event resulting in an order of magnitude increase in the emitted current, a peak shift of $\sim$ 2 V, and a narrow energy spread of $\sim$ 0.4 eV (right)

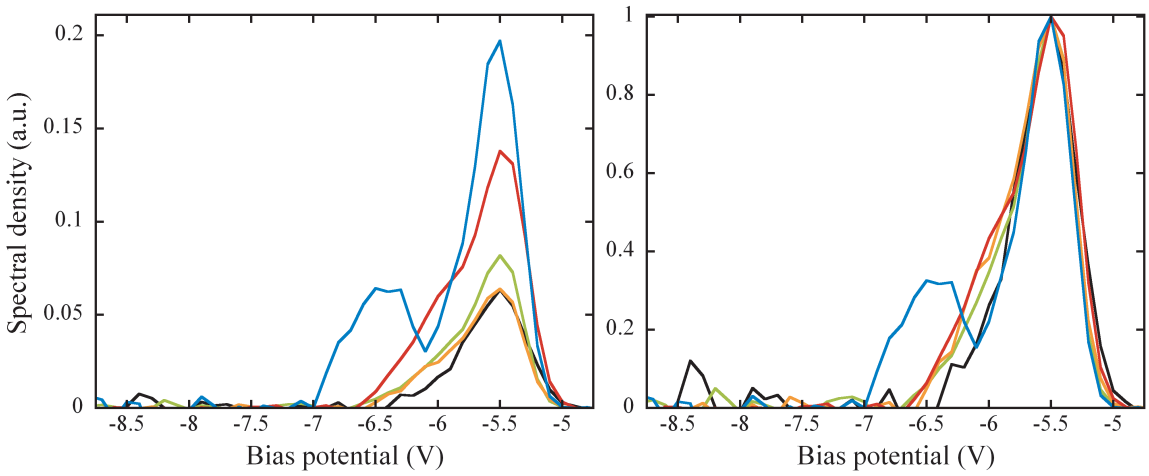

Figure 5.14: Emission spectra that may have originated from a clean diamond surface. These distributions share a well defined spectral feature at -5.5 eV.

emission is given by [40, 41]

$$j'_{TFE}(T,E) = \frac{e^{E/d}}{1+e^{E/k_BT}}, \tag{5.10}$$

where

$$d = \frac{qhF}{4\pi t(y_0)\sqrt{2m_e\phi}}, \tag{5.11}$$

ϕ is the emitter's work function, h is Planck's constant, q is the electron charge, m_e is the electron mass, and $t(y_0)$ is given by

$$t(y_0) = 1 + 0.1107y_0^{1.33}. \tag{5.12}$$

The argument y_0 is

$$y_0 = \frac{\sqrt{q^3F/4\pi\epsilon_0}}{\phi}, \tag{5.13}$$

where ϵ_0 is the permittivity of free space. This model may be used to fit the purported clean diamond spectrum once the instrumental broadening has been deconvolved. The results of this fit are seen in Figure 5.15. The work function is assumed to be ~ 5 eV, and the temperature and electric field are allowed to vary as fitting parameters. The best fit is given

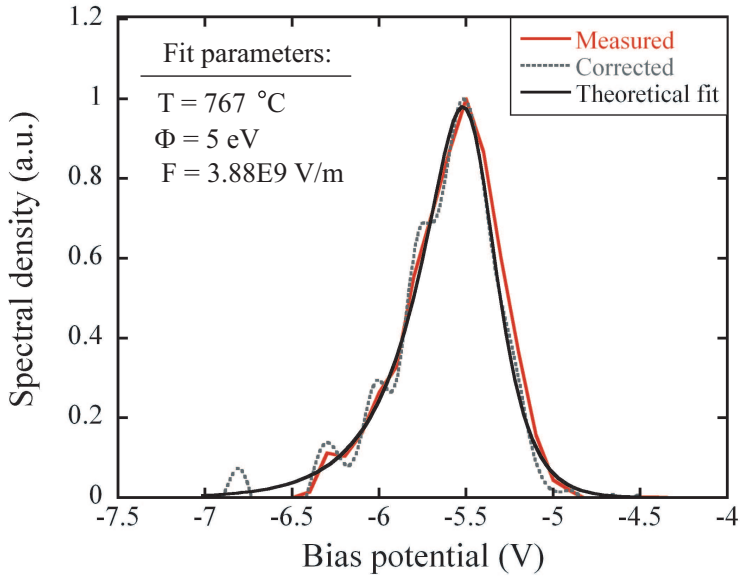

Figure 5.15: The proposed clean-diamond emission spectrum with and without resolution function correction. The corrected trace is fit with a thermal-field emission model.

by $T = 767$ °C and $F = 3.88 \times 10^9$ V/m. While there is significant joule heating of the emitter tips during large per-tip current operation (several μA/tip), these data were taken at a per-tip current of ~ 30 nA, so the fit temperature seems rather high. Further experiments are needed to constrain the values of T and F, and to determine ϕ. The proposed clean spectrum is very similar, both in shape and width (~ 0.5 eV), to the field emission spectra from a nitrogen-containing diamond-like-carbon film, reported in [42]. A heating system is presently being integrated with the cathode holder to allow substrate temperatures up to ~ 350 °C. Operation at elevated temperatures will enable rapid desorption of adsorbed species from the emitter surface. Additionally, flexibility is being added to provide limited translational capability for the cathode holder. This will facilitate the examination of multiple emitters, one by one, so that tip-to-tip variations in the emitted spectra can be studied.

CHAPTER VI

THE SMITH-PURCELL FREE-ELECTRON LASER: AN APPLICATION OF DFEAS

VI.1 Smith-Purcell Radiation and Superradiant Effects

An electron passing in close proximity to a metallic grating (Figure 6.1) emits a wide spectrum of radiation into the space above. This is called Smith-Purcell radiation (SPR) and can be viewed as scattering of the electron's virtual photon field by the grating. Smith and Purcell first demonstrated SPR in 1953 [43] by using a 1.67 μm grating pitch and a beam of $\sim$ 300 kV electrons to produce radiation in the visible spectrum. The periodic nature of the scattering surface provides a coherence condition relating the emitted wavelength to the angle of observation in the far field. This relation, proposed and verified by Smith and Purcell, is given by

$$\lambda_{SP} = \frac{L}{|p|}\left[\frac{1}{\beta} - \cos(\theta)\right], \tag{6.1}$$

where L is the grating period, the integer p is the grating order, β is the electron velocity as

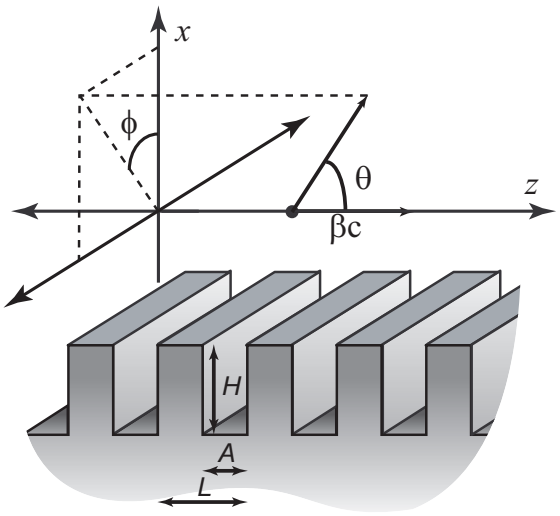

Figure 6.1: An electron passing near a metallic lamellar grating.

a fraction of the speed of light, and θ is the angle of observation measured from the beam

axis. For a given grating period and order the Smith-Purcell band is given by

$$\frac{L}{|p|}\left(\frac{1-\beta}{\beta}\right) \leq \lambda_{SP} \leq \frac{L}{|p|}\left(\frac{1+\beta}{\beta}\right). \tag{6.2}$$

A multitude of theoretical treatments of SPR have been performed which address incoherent, coherent, and superradiant effects [44–51]. In this discussion we follow our previous analysis of SPR and superradiant emission [52]. This theory has been verified with particle-in-cell simulations by Li [53]. We consider the incoherent radiation from a single electron and then extend this result to the cases of single and periodic bunches. The angular spectral fluence emitted by a single electron passing over the grating is given by [54]

$$\frac{d^2\mathcal{W}^{(1)}}{d\omega d\Omega} = \frac{2cR^2}{\mu_0}\left|\tilde{\mathbf{B}}^{(1)}(\omega)\right|^2 \tag{6.3}$$

where c is the speed of light, R is the distance to the far-field observation point, μ_0 is the permeability of free space, and $\tilde{\mathbf{B}}^{(1)}(\omega)$ is the Fourier transform of the magnetic field at the observation point. Assuming a long grating and ignoring edge radiation and bound surface modes, $\tilde{\mathbf{B}}^{(\mathbf{1})}(\omega)$ is shown to be

$$\begin{aligned}\tilde{\mathbf{B}}^{(1)}(\omega) &= \frac{Z_g}{\sqrt{2\pi}}\frac{1-\beta\cos(\theta)}{\beta cR}e^{i\omega/c(R-\delta z/\beta)} \\ &\times \sum_{p=-\infty}^{\infty}\mathbf{a}_p \mathrm{sinc}\left[\frac{Z_g}{2}\left(\frac{\omega}{c}\frac{1-\beta\cos(\theta)}{\beta}+pK\right)\right]\end{aligned} \tag{6.4}$$

where Z_g is the grating length, δz is the electron's initial longitudinal position, and $K = 2\pi/L$ is the grating wavenumber. The coefficients $\mathbf{a}_p$ depend on the unit vector $\hat{\mathbf{R}}(\theta,\phi)$, the electron energy and height above the grating, and the geometric profile of the grating [52]. The argument of the $sinc$ function can be recognized as the aforementioned Smith-Purcell relation. The field is maximized for a given frequency when

$$\frac{\omega}{c}\left(\frac{1-\beta\cos(\theta)}{\beta}\right)+pK=0, \tag{6.5}$$

and the spectral width of order p is approximately

$$\frac{\delta\omega}{\omega} = \frac{1}{|p|\, N_g} \tag{6.6}$$

where N_g is the number of periods in the grating. If $N_g >> 1$ then the radiation on adjacent grating orders is well separated in frequency, and the angular spectral fluence on order p from a single electron is given by

$$\begin{aligned} \frac{d^2\mathcal{W}_p^{(1)}}{d\omega d\Omega} &= \frac{Z_g^2}{\pi\mu_0 c}\left(\frac{1-\beta\cos(\theta)}{\beta}\right)^2 |\mathbf{a}_p|^2 \\ &\times \operatorname{sinc}^2\left[\frac{Z_g}{2}\left(\frac{\omega}{c}\frac{1-\beta\cos(\theta)}{\beta} + pK\right)\right]. \end{aligned} \tag{6.7}$$

Consider N_e electrons passing over the grating simultaneously with the j^{th} electron having an initial position δz_j; the total angular spectral fluence on order p is then given by

$$\frac{d^2\mathcal{W}_p^{(N_e)}}{d\omega d\Omega} = \frac{d^2\mathcal{W}_p^{(1)}}{d\omega d\Omega}\left|\sum_{j=1}^{N_e} e^{-i\omega\delta z_j/\beta c}\right|^2. \tag{6.8}$$

The behavior of the phase-factor summation in (6.8) depends on the bunching spectrum of the electron ensemble. For a large number of electrons with random spacings comparable to the radiation wavelength the summation is $\sim \sqrt{N_e}$, and the resulting angular spectral fluence is a factor of N_e larger than the single electron case. If the electrons are concentrated in a single bunch with length $\Delta z << \beta c/\omega$ then the radiation is emitted coherently and the angular spectral fluence increases by a factor of N_e^2 relative to the single electron case. In both of these cases the simple proportionality of the angular spectral fluence to the single particle case indicates unchanged spectral and angular distributions. If N_b electron bunches are spaced periodically with frequency ω_b then the phase-factor summation is

$$\left|\sum_{j=1}^{N_e} e^{-i\omega\delta z_j/\beta c}\right| = \left|\sum_{j=1}^{N_b} n_e e^{-i\omega j z_b/\beta c}\right| = \frac{\sin\left(\frac{N_b}{2}\frac{\omega z_b}{\beta c}\right)}{\sin\left(\frac{1}{2}\frac{\omega z_b}{\beta c}\right)} \tag{6.9}$$

where n_e is the number of electrons per bunch and $z_b = 2\pi\beta c/\omega_b$ is the bunch separation. When the number of bunches is large, sharp resonances appear at harmonics of the bunching frequency $\omega_h = h\omega_b = 2\pi h\beta c/z_b$ where h is an integer. Expansion of the denominator of (6.9) around these harmonics and substitution into (6.8) gives

$$\frac{d^2\mathcal{W}_{ph}^{(N_e)}}{d\omega d\Omega} = N_e^2 \mathrm{sinc}^2\left(\pi N_b \frac{\omega - \omega_h}{\omega_b}\right) \frac{d^2\mathcal{W}_p^{(1)}}{d\omega d\Omega}. \tag{6.10}$$

When a bunching harmonic is within the Smith-Purcell band the angular power spectrum changes dramatically. The SPR is concentrated into narrow angular peaks centered at

$$\cos(\theta_h) = \frac{1}{\beta} - \frac{|p|\, cK}{\omega_h}. \tag{6.11}$$

In addition to SPR the grating supports non-radiative subluminal electromagnetic modes. The grating periodicity slows the phase velocity of this radiation and facilitates interaction with a passing electron beam. The electron beam behaves as a gain medium for these evanescent modes and under certain conditions the system may spontaneously oscillate. The electron beam becomes bunched on the wavelength of the radiation and superradiant emission results as described in (6.10) and (6.11). Using an evanescent mode of the grating to bunch the electron beam and produce superradiant SPR is the basis of a Smith-Purcell free-electron laser.

VI.2 **SPFEL Experiments**

The generation of superradiant SPR from an SPFEL configuration was first reported by Urata, et al. at Dartmouth College [5]. The experimental apparatus, pictured in Figure 6.2 [5], was a scanning electron microscope (SEM) that had been converted for high current operation. Modification of an existing SEM is a natural choice for SPR sources due to the flexible electron optical systems and low emittance beams that they employ. This device utilized a tungsten-hairpin cathode and produced a continuous electron beam

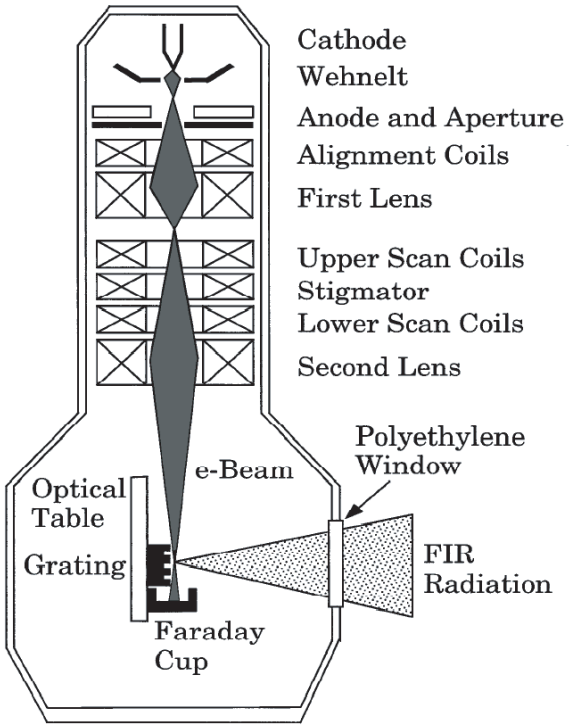

Figure 6.2: Experimental arrangement of the Dartmouth SPFEL [5].

of up to 1 mA in current, beam energies of 20-40 kV, and a minimum beam diameter of $\sim$ 25 μm. The theory of van den Berg [55] was used to design gratings that were optimized for maximum emission of first order SPR directed normally from the grating. The radiation was detected with a Helium-cooled Silicon bolometer and spectra were taken with either a Czerny-Turner monochromater or a Michelson interferometer. Spectra of the radiation were in strong agreement with (6.2) and the radiation was srongly polarized, ruling out blackbody radiation from a beam heated grating [56] as a source. The average power was measured as a function of the electron beam current and two distinct regimes of operation were observed: linear, and superlinear. In the superlinear regime the measured power varied as I^{α} where α ranged from 3-6 depending on the focal settings of the electron optical system. The transition between these two operating regimes was marked by a hard threshold and was interpreted as the onset of a stimulated emission process between the grating and the electron beam [57]. An example of this superradiant behavior is pictured

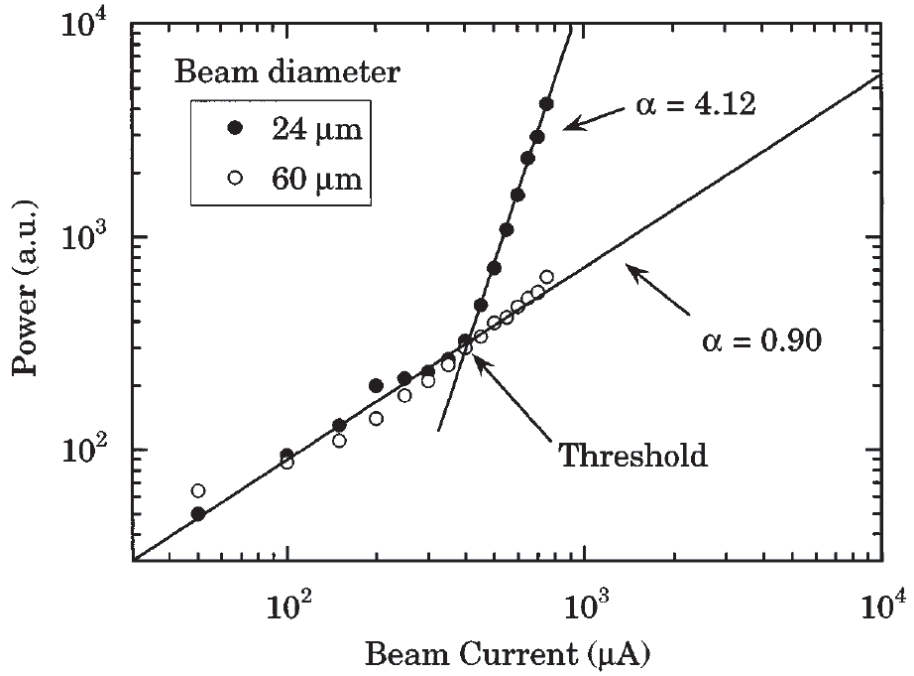

Figure 6.3: Linear and superlinear regimes of operation in the original Dartmouth experiments [5].

in Figure 6.3 [5]. While superlinear current dependence was observed for a multitude of grating parameters and electron beam conditions, the spectral-power distribution was unchanged by the transition to the superlinear regime. The onset of superradiance marks the presence of periodic density modulations in the electron beam. Provided the period of these modulations is on the order of the radiation wavelength, the coherence conditions mentioned in section VI.1 should produce dramatic changes in the spectral-power-density. The lack of observed spectral modification is perhaps the most surprising characteristic of the Dartmouth experiments.

Several years after the original Dartmouth experiments, another SEM based Smith-Purcell device was demonstrated by Kapp et al. at the University of Chicago [56]. This device was capable of producing up to 30-kV, 10-mA, low-emittance electron beams. The beam envelope was characterized by rapidly scanning over a specially made Molybdenum profilometer. It was found that the beam brightness could be changed by an order of magnitude through the range of accessible currents, while the emittance remained

relatively constant. The beam was rastered perpendicular to the grating surface producing a modulated THz output that was detected with a Silicon bolometer, lock-in amplifier, and oscilloscope. A light pipe was positioned close to the grating for efficient THz transport to the system's polyethylene output window. A filter set was used to confirm that the central wavelength of the emission was in agreement with the Smith-Purcell relation (6.2). Estimated power levels were very low, $\sim$ 1 nW, even for high current operation of $\sim$ 5 mA. Furthermore, the best performance was achieved with smaller, low divergence beams even if they contained less total current. While these experiments produced both linear and nonlinear emission regimes, it was concluded that the nonlinearity was due entirely to blackbody radiation from electron beam heating of the grating and other apparatus components. The nonlinear regime disappeared with the application of water cooling and minimization of current interception by the grating.

Two other SPFEL devices are located at Vermont Photonics, Inc. in Bellows Falls, Vermont. Vermont Photonics has produced two identical SPFEL systems that are functionally similar to the SEM based sources mentioned previously. These devices demonstrate nonlinear behavior similar to the Dartmouth system and the spectral-power distribution remains unchanged in the superlinear regime. Electron beam energies of 20-40 kV and currents up to 15 mA are achievable with spot sizes on the order of $\sim 50\ \mu\mathrm{m}$. The Rayleigh range of the beam is approximately equal to half the grating length, $\sim$ 4 mm, to maximize the beam-wave interaction. Tunable THz SPR has been produced from 10-100 cm^{-1} and at power levels up to $\sim 30\ \mu\mathrm{W}$. These sources are unique in that the grating assembly has metallic sidewalls which confine the evanescent modes in the transverse dimension and aid in the transport of SPR to the output window. The theory of such a confined-mode SPFEL is presented in detail in section VI.3.2. Recently, the Vermont Photonics system has been used to explore the Vanderbilt theory of SPFEL operation. These experiments and their comparison to the Vanderbilt SPFEL theory are discussed in section VI.4.

VI.3 **SPFEL Theory**

Some of the earliest theoretical analysis of resonant coupling between an electron beam and a slow-wave structure (SWS) was that of Pierce on the traveling-wave tube (TWT) [58, 59]. Pierce interpreted the interaction as the coupling between a structure wave of the SWS geometry and two space-charge waves of the electron beam. The only structure waves that interact strongly are those that have a phase velocity synchronous with the electron beam. In a TWT the group velocity of the laser mode is positive, and thus its stored energy co-propagates with the electron beam. TWTs are therefore amplifiers and operate on a convective instability. However, such devices can be made to oscillate by utilizing an external resonator or, less efficiently, with parasitic end reflections. If the group velocity at the synchronous point is negative, then the device operates on an absolute instability and may spontaneously oscillate without the assistance of cavity mirrors or end reflections. Such backward-wave oscillators (BWO) were demonstrated experimentally [60, 61] and described theoretically [62] by the early 1950's.

Although different in structure from the early helical and axially symmetric devices, the fundamental operating principle of the SPFEL is the same: resonant energy transfer between the electron beam and a synchronous structure wave causes bunching of the electrons and amplitude growth of the wave. The open grating of the SPFEL supports structure waves which evanesce in the direction normal to the grating surface. The group velocity of these evanescent modes can be either positive or negative, facilitating amplifier or oscillator operation. The two-dimensional theory of this device, including the effects of losses and end reflections, has been examined in detail for the exponential gain/growth regime [63–66], and is closely supported by particle-in-cell (PIC) simulations [65, 67]. Three-dimensional PIC simulations have also been performed for gratings with and without sidewalls [68, 69]. A two-dimensional numerical treatment of device operation from startup to saturation, with one-dimensional electron dynamics, has also been performed [66]. Recently we have developed an analytic theory of SPFEL operation in three dimensions

for the case of an infinitely wide grating (section VI.3.1) [70, 71]. The primary conclusion of section VI.3.1 is that some form of transverse mode confinement is required if an SPFEL is to be experimentally viable. The theory of such a confined-mode SPFEL is presented in section VI.3.2 [72].

In the following theoretical treatments the electron beam is modeled as a relativistic moving-plasma dielectric, and we confine our analysis to the exponential gain/growth regime. In each case the dispersion relation is calculated subject to the boundary conditions of the grating geometry. The electron beam is then added as a perturbation and the resulting complex wavenumber and frequency shifts are calculated for the synchronous structure wave. These shifts result in growth or decay of the evanescent field in space and time, and in this way the electron beam behaves as a gain medium for the radiation mode. While the two-dimensional theory of this process is not considered in the following sections, the reader is referred to [63–65].

VI.3.1 **Three-dimensional theory**

In this section, we include the effects of transverse diffraction in the optical beam of a SPFEL. The approach is similar to that used for the 3-D theory of the Cerenkov FEL [73]. As expected, three-dimensional effects increase the gain length substantially compared to the 2-D theory. Furthermore, the dependence of the gain length on beam current increases due to gain guiding. We find that diffraction of the optical beam in the grating subdivides device operation into two amplifier regions and two oscillator regions. For the amplifier and oscillator regions furthest from the Bragg point, where the group velocity vanishes, we find the inclusion of a fast wave in the physically allowed solutions. This is surprising, considering the nature of a guided system. For the oscillator region closest to the Bragg point there are only two physically allowed solutions. It is not known how the required boundary conditions on the electron and optical beams can be satisfied in this region.

Dispersion: In an SPFEL, resonant energy exchange between the electron beam and bound surface modes gives rise to spatial modulations in the beam density. For an electron beam energy of 150 kV and the grating parameters of Table 6.1, the intensity scale height of the evanescent wave is $\Delta x = \beta\gamma\lambda/4\pi \approx 40\ \mu\mathrm{m}$, where $\beta \approx 0.43$ is the normalized electron velocity, $\gamma = 1/\sqrt{1-\beta^2}$, and $\lambda \approx 10^{-3}\ \mathrm{m}$ is the free-space wavelength. We

Table 6.1: Example grating and beam parameters used in 3-D theory calculations

Grating period	173 μm
Groove width	62 μm
Groove depth	100 μm
Grating length	12.7 mm
E-beam width/height	60 μm
E-beam centroid height from grating top	30 μm
E-beam current	1 mA

anticipate from simple diffraction arguments that the transverse mode width is of order $\Delta y = \sqrt{\beta\lambda Z_g/2\pi}$, where Z_g is the gain length. For a gain length on the order of the grating length, the transverse width is on the order of millimeters. Schematics of the device geometry with all pertinent dimensions are given in Figure 6.4. Because the fields vanish exponentially above the scale height, we simplify the theory by allowing the electron beam to extend to infinity in the x direction. A filling factor can be used to correct for errors introduced by this approximation [74].

In the following analysis we consider only transverse-magnetic (TM) modes of the grating for two reasons. First, to lowest order in the fields, the electron beam resonantly exchanges energy with only the TM modes longitudinal-electric-field component. Energy exchange with transverse-electric (TE) modes is of higher order in the fields and is ignored. Secondly, because the beam is a perturbation, the modes of the inhomogeneous system should resemble those of the empty grating. The empty grating of infinite width does not support TE modes.

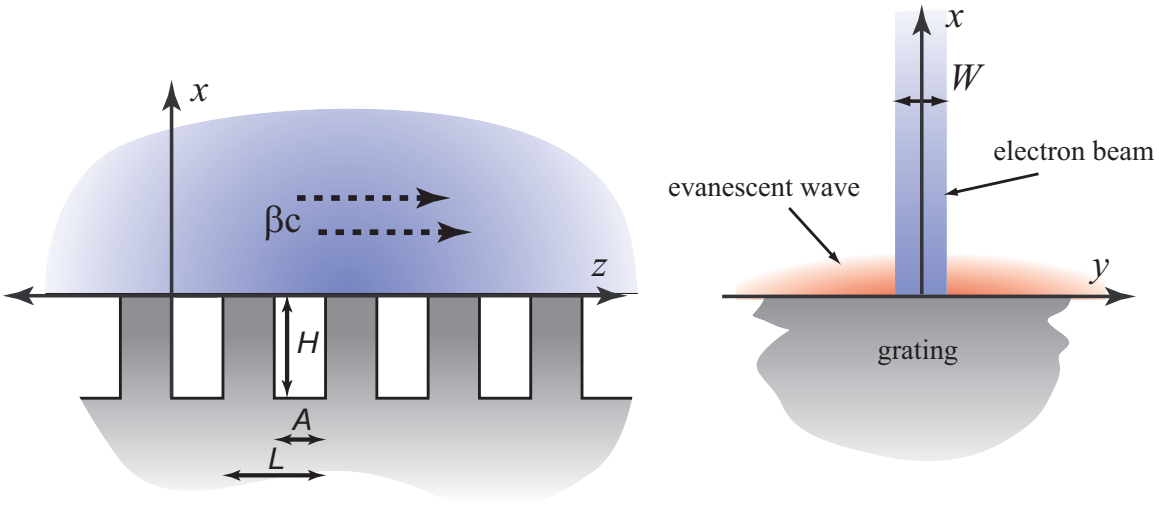

Figure 6.4: Schematic representation of an SPFEL with an infinitely wide grating.

We begin by expressing the fields inside the grooves as Fourier series

$$E_z^{(g)} = \sum_{n=0}^{\infty} E_n^{(g)}(x,y)\cos\left(\frac{n\pi}{A}z\right)e^{-i\omega t} \tag{6.12}$$

$$H_y^{(g)} = \sum_{n=0}^{\infty} H_n^{(g)}(x,y)\cos\left(\frac{n\pi}{A}z\right)e^{-i\omega t} \tag{6.13}$$

where A is the groove width, and ω is the frequency. Each term in the fields must satisfy the wave equation, which is given in the grooves by

$$\left[\nabla_t^2 - \frac{n^2\pi^2}{A^2} + \frac{\omega^2}{c^2}\right] E_n^{(g)}(x,y) = 0 \tag{6.14}$$

where ∇_t is the transverse gradient operator. Taking the Fourier transform of (6.14) in the y direction we have

$$\left[\frac{\partial^2}{\partial x^2} - k_y^2 - \frac{n^2\pi^2}{A^2} + \frac{\omega^2}{c^2}\right] \tilde{E}_n^{(g)}(x,k_y) = 0. \tag{6.15}$$

where k_y is the wavenumber in the y direction. The solution for $\tilde{E}_n^{(g)}(x,k_y)$ that vanishes

at the bottom of the grooves $(x = -H)$ is

$$\tilde{E}_n^{(g)}(x, k_y) = \bar{\tilde{E}}_n^{(g)}(k_y) \sinh\left[\kappa_n(k_y)(x + H)\right], \tag{6.16}$$

where

$$\kappa_n^2 = k_y^2 + \frac{n^2\pi^2}{A^2} - \frac{\omega^2}{c^2}. \tag{6.17}$$

For a TM mode, the components $\tilde{E}_n^{(g)}(x, k_y)$ and $\tilde{H}_n^{(g)}(x, k_y)$ are related through the Maxwell equations by [75]

$$\tilde{H}_n^{(g)}(x, k_y) = \frac{i\omega\epsilon_0 c^2}{\omega^2 - \frac{n^2\pi^2}{A^2}c^2} \frac{\partial}{\partial x} \tilde{E}_n^{(g)}(x, k_y). \tag{6.18}$$

Substituting the solution for $\tilde{E}_n^{(g)}(x, k_y)$ into (6.18), we get

$$\tilde{H}_n^{(g)}(x, k_y) = \bar{\tilde{H}}_n^{(g)}(k_y) \cosh\left[\kappa_n(k_y)(x + H)\right], \tag{6.19}$$

where

$$\bar{\tilde{H}}_n^{(g)}(k_y) = \frac{i\omega\epsilon_0 c^2}{\omega^2 - \frac{n^2\pi^2}{A^2}c^2} \kappa_n(k_y) \bar{\tilde{E}}_n^{(g)}(k_y). \tag{6.20}$$

Above the grating we expand the fields in Floquet series (space harmonics) of the form

$$E_z^{(e)} = \sum_{p=-\infty}^{\infty} E_p^{(e)}(x, y)\, e^{-ipKz} e^{i(kz - \omega t)} \tag{6.21}$$

$$H_y^{(e)} = \sum_{p=-\infty}^{\infty} H_p^{(e)}(x, y)\, e^{-ipKz} e^{i(kz - \omega t)} \tag{6.22}$$

where k is the longitudinal wavenumber, $K = 2\pi/L$ is the grating wavenumber, and L is the grating period. The electron beam is treated as an isotropic dielectric in its rest frame (primed coordinates), having an index of refraction given by [76]

$$n'(\omega')^2 = 1 + \chi_e'(\omega') = 1 - \frac{\omega_e'^2}{\omega'^2} \tag{6.23}$$

where $\chi'_e = -\omega'^2_e/\omega'^2$ is the frequency-dependent susceptibility, and ω'_e is the plasma frequency in the rest frame. The wave equation above the grating is

$$\left[\nabla'^2_t - (k' + pK')^2 + \frac{\omega'^2_p}{c^2} - \frac{\omega'^2_e}{c^2}\right] E^{(e)\prime}_p(x', y') = 0 \tag{6.24}$$

We note that $(k + pK)^2 - \omega_p^2/c^2$, $E_p^{(e)}$, and the transverse dimensions, x and y, are Lorentz invariant. In terms of rest-frame variables, the frequency ω'_p depends on the wavenumber, as denoted by the p subscript. Using the parameters of Table 6.1, the plasma frequency is calculated to be of the order $\sim 10^{10}$ Hz, while the operating frequency is of the order $\sim 10^{12}$ Hz. We then make the approximation $\omega'^2_e << (k' + pK')^2 c^2 - \omega'^2_p$ and simplify (6.24) as

$$\left[\nabla_t^2 - (k + pK)^2 + \frac{\omega^2}{c^2}\right] E_p^{(e)}(x, y) = 0 \tag{6.25}$$

As before, we Fourier transform the wave equation in y and get

$$\left[\frac{\partial^2}{\partial x^2} - (k + pK)^2 + \frac{\omega^2}{c^2}\right] \tilde{E}_p^{(e)}(x, k_y) + \frac{1}{\sqrt{2\pi}} \int_{-\infty}^{\infty} dy e^{ik_y y} \frac{\partial^2}{\partial y^2} E_p^{(e)}(x, y) = 0 \tag{6.26}$$

If we integrate by parts and ignore the discontinuities in $\partial E_p^{(e)}/\partial y$, for an optical beam with $\Delta x/\Delta y << 1$ [73], (6.26) becomes

$$\frac{\partial^2}{\partial x^2} \tilde{E}_p^{(e)}(x, k_y) = \left[(k + pK)^2 + k_y^2 - \frac{\omega^2}{c^2}\right] \tilde{E}_p^{(e)}(x, k_y). \tag{6.27}$$

The solution that vanishes at $x = \infty$ is

$$\tilde{E}_p^{(e)}(x, k_y) = \bar{\bar{E}}_p^{(e)}(k_y)\, e^{-\alpha_p(k_y)x}, \tag{6.28}$$

where

$$\alpha_p^2 = (k + pK)^2 + k_y^2 - \frac{\omega^2}{c^2}. \tag{6.29}$$

The Maxwell equations relate $H_p^{(e)\prime}(x,y)$ and $E_p^{(e)\prime}(x,y)$ above the grating by

$$H_p^{(e)\prime}(x,y) = \frac{i\omega_p'\epsilon_0\left(1+\chi_p'\right)c^2}{\omega^2-\left(k+pK\right)^2c^2}\frac{\partial}{\partial x}E_p^{(e)}(x,y), \tag{6.30}$$

where we ignore $\omega_e'^2 << \left(k'+pK'\right)^2c^2$ in the denominator. To transform $H_p^{(e)\prime}(x,y)$ to the laboratory frame we use

$$H_p = \gamma\left(H_p' + \beta c D_p'\right), \tag{6.31}$$

where D_p' is the x component of the displacement field. From the Maxwell-Ampere law we have $\omega_p' D_p' = \left(k'+pK'\right)H_p'$. Combining this with (6.31), and recognizing that $\gamma\left[\omega_p'+\beta\left(k'+pK'\right)\right]$ is the Lorentz transformation of ω, we see that $H_p^{(e)\prime}(x,y)$ and $H_p^{(e)}(x,y)$ are related by $H_p^{(e)}(x,y) = \frac{\omega}{\omega_p'}H_p^{(e)\prime}(x,y)$. The field in the laboratory frame is then

$$H_p^{(e)}(x,y) = \frac{i\omega\epsilon_0\left(1+\chi_p'\right)c^2}{\omega^2-\left(k+pK\right)^2c^2}\frac{\partial}{\partial x}E_p^{(e)}(x,y). \tag{6.32}$$

Fourier transforming (6.32) in y, we get

$$\begin{aligned}\tilde{H}_p^{(e)}(x,k_y) &= \frac{i\omega\epsilon_0 c^2}{\omega^2-\left(k+pK\right)^2c^2} \\ &\times \left[\frac{\partial}{\partial x}\tilde{E}_p^{(e)}(x,k_y) + \frac{1}{\sqrt{2\pi}}\int_{-\infty}^{\infty}dy e^{ik_y y}\chi_p'(y)\frac{\partial}{\partial x}E_p^{(e)}(x,y)\right].\end{aligned} \tag{6.33}$$

We simplify (6.34) by using the Faltung theorem to write the integral as

$$\begin{aligned}\frac{1}{\sqrt{2\pi}}\int_{-\infty}^{\infty}dy\, e^{ik_y y}\,\chi_p'(y)\frac{\partial}{\partial x}E_p^{(e)}(x,y) = \\ -\frac{1}{\sqrt{2\pi}}\int_{-\infty}^{\infty}dk_y'\tilde{\chi}_p'\left(k_y-k_y'\right)\alpha_p\left(k_y'\right)\tilde{\bar{E}}_p^{(e)}\left(k_y'\right)e^{-\alpha_p\left(k_y'\right)x}\end{aligned} \tag{6.34}$$

where k_y' is a dummy variable and the Fourier transform of the susceptibility is

$$\tilde{\chi_e}'\left(k_y-k_y'\right) = -\frac{1}{\sqrt{2\pi}}\frac{\omega_e'^2}{\omega_p'^2}\int_{-W/2}^{W/2}dy e^{i\left(k_y-k_y'\right)y} - \frac{W}{\sqrt{2\pi}}\frac{\omega_e'^2}{\omega_p'^2}\mathrm{sinc}\left[\frac{W}{2}\left(k_y-k_y'\right)\right]. \tag{6.35}$$

When written in terms of lab-frame variables, $\omega_e'^2/\omega_p'^2$ becomes

$$\frac{\omega_e'^2}{\omega_p'^2} = \frac{\omega_e^2}{\gamma^3 \left[\omega - \beta c \left(k + pK\right)\right]^2}. \tag{6.36}$$

This is divergent near the synchronous point $\omega = \beta ck$ only for $p = 0$. For all other $p \neq 0$ we may ignore the perturbation and rewrite (6.34) as

$$\begin{aligned} \tilde{H}_p^{(e)}\left(x, k_y\right) = \frac{i\omega\epsilon_0 c^2}{\omega^2 - \left(k + pK\right)^2 c^2} \Bigg\{ -\alpha_p\left(k_y\right) e^{-\alpha_p(k_y)x} \bar{\tilde{E}}_p^{(e)} + \delta_{p,0}\frac{W}{2\pi} \\ \times \quad \frac{\omega_e^2}{\gamma^3\left(\omega - \beta ck\right)^2} \int_{-\infty}^{\infty} dk_y' \mathrm{sinc}\left[\frac{W}{2}\left(k_y - k_y'\right)\right] \alpha_0\left(k_y'\right) \bar{\tilde{E}}_0^{(e)}\left(k_y'\right) e^{-\alpha_0\left(k_y'\right)x} \Bigg\} \end{aligned} \tag{6.37}$$

where $\delta_{p,0}$ is the Kronecker delta.

Next we force continuity in $\tilde{E}_z$ and $\tilde{H}_y$ at the $x = 0$ interface. In the grooves $(0 < z < A)$, suppressing the harmonic time dependence, we have

$$\tilde{E}_z^{(g)}\left(x = 0, k_y\right) = \sum_{n=0}^{\infty} \bar{\tilde{E}}_n^{(g)}\left(k_y\right) \sinh\left[\kappa_n\left(k_y\right) H\right] \cos\left(\frac{n\pi}{A} z\right), \tag{6.38}$$

$$\tilde{H}_y^{(g)}\left(x = 0, k_y\right) = \sum_{n=0}^{\infty} \bar{\tilde{H}}_n^{(g)}\left(k_y\right) \cosh\left[\kappa_n\left(k_y\right) H\right] \cos\left(\frac{n\pi}{A} z\right), \tag{6.39}$$

and on the teeth $(A < z < L)$

$$\tilde{E}_z^{(g)}\left(x = 0, k_y\right) = 0. \tag{6.40}$$

Just above the grating, $\tilde{E}_z^{(e)}$ is given by

$$\tilde{E}_z^{(e)}\left(x = 0, k_y\right) = \sum_{p=-\infty}^{\infty} \bar{\tilde{E}}_p^{(e)}\left(k_y\right) e^{i(k+pK)z}. \tag{6.41}$$

Setting (6.39) equal to (6.41), multiplying both sides by $e^{-i(k+pK)z}$, and integrating over

the grating period L, we get

$$\bar{\tilde{E}}_q^{(e)}(k_y) = \frac{1}{L}\sum_{n=0}^{\infty} \bar{\tilde{E}}_n^{(g)}(k_y)\sinh\left[\kappa_n(k_y)H\right]K_{qn} \tag{6.42}$$

where

$$K_{qn} = iA\frac{(k+qK)A}{(k+qK)^2A^2 - n^2\pi^2}\left[(-1)^n e^{-i(k+qK)A} - 1\right]. \tag{6.43}$$

Similarly, making $\tilde{H}_y$ continuous across the $x = 0$ interface within the groove, multiplying both sides by $\cos\left(\frac{m\pi}{A}z\right)$, and integrating from 0 to A, we find

$$\bar{\tilde{H}}_m^{(g)}(k_y)\frac{1+\delta_{m,0}}{2}A\cosh\left[\kappa_m(k_y)H\right] = \sum_{p=-\infty}^{\infty}\tilde{H}_p^{(e)}(0,k_y)K_{pm}^*. \tag{6.44}$$

We may now substitute expressions (6.20) and (6.38) into (6.44), remembering to evaluate at $x = 0$, and then use (6.42) to arrive at the dispersion relation

$$\bar{\tilde{E}}_m^{(g)}(k_y) = \sum_{n=0}^{\infty}\left[R_{mn}(k_y)\bar{\tilde{E}}_n^{(g)}(k_y) + S_{mn}\left(k_y, \bar{\tilde{E}}_n^{(g)}(k_y)\right)\right]. \tag{6.45}$$

The first term in the square brackets represents modes admitted by the empty (no beam) grating. The second term embodies the modification of those modes by the presence of the electron beam. The matrix elements are given by

$$\begin{aligned} R_{mn}(k_y) = &-\frac{4}{1+\delta_{m,0}}\frac{A}{L}\frac{\sinh\left[\kappa_n(k_y)\right]}{\cosh\left[\kappa_n(k_y)\right]}\frac{\omega^2 - \frac{m^2\pi^2}{A^2}c^2}{\kappa_m(k_y)} \\ \times &\sum_{p=-\infty}^{\infty}\frac{(k+pK)A}{(k+pK)^2A^2 - n^2\pi^2}\frac{(k+pK)A}{(k+pK)^2A^2 - m^2\pi^2}\frac{\alpha_p(k_y)}{\omega^2 - (k+pK)^2c^2} \\ &\times\begin{cases} 1-(-1)^m\cos\left[(k+pK)A\right] & m+n = \text{even} \\ i(-1)^m\sin\left[(k+pK)A\right] & m+n = \text{odd} \end{cases}, \end{aligned} \tag{6.46}$$

and

$$
\begin{aligned}
& S_{mn}\left(k_y, \bar{\tilde{E}}_n^{(g)}\right) \\
= \; & \frac{W}{AL\pi\left(1+\delta_{m,0}\right)} \frac{1}{\cosh\left[\kappa_m\left(k_y\right) H\right]} \frac{\omega^2 - \frac{m^2\pi^2}{A^2}c^2}{\kappa_m\left(k_y\right)} \frac{K_{0n}K_{0m}^*}{\omega^2 - k^2c^2} \frac{\omega_e^2}{\gamma^3\left[\omega - \beta ck\right]^2} \\
\times \; & \int_{-\infty}^{\infty} dk_y' \mathrm{sinc}\left[\frac{W}{2}\left(k_y - k_y'\right)\right] \alpha_0\left(k_y'\right) \sinh\left[\kappa_n\left(k_y'\right) H\right] \bar{\tilde{E}}_n^{(g)}\left(k_y'\right)
\end{aligned}
\tag{6.47}
$$

Calculations show that the dispersion relation for the grating is well described using a single term $(m, n = 0)$ for the groove fields, provided that we use at least three terms $(-1 < p < 1)$ for the fields above the grating. We therefore define the dispersion function $D\left(\omega, k, k_y\right)$ as

$$
D\left(\omega, k, k_y\right) = 1 - R_{00}\left(\omega, k, k_y\right). \tag{6.48}
$$

The dispersion curve $D\left(\omega, k, 0\right) = 0$, for waves traveling normal to the grooves of the empty grating described by Table 6.1, is plotted in Figure 6.5, along with a 150-kV beam line. At the intersection of these curves the phase velocity of the evanescent wave and the electron beam are synchronous, i.e. $\omega/k = \beta c$. Energy in the evanescent mode will travel along the grating at the group velocity $\beta_g = d\omega/dk$.

When the electron beam is present, the dispersion relation (6.45) becomes

$$
\begin{aligned}
D\left(\omega, k, ky\right) \bar{\tilde{E}}_0^{(g)}\left(k_y\right) = & \frac{W}{\pi ALk^2} \frac{\omega_e^2}{\gamma^3\left[\omega - \beta ck\right]^2} \frac{1 - \cos\left(kA\right)}{\cosh\left[\kappa_0\left(k_y\right) H\right]} \frac{\omega^2}{\kappa_0\left(k_y\right)} \frac{1}{\omega^2 - k^2c^2} \\
\times \; & \int_{-\infty}^{\infty} dk_y' \mathrm{sinc}\left[\frac{W}{2}\left(k_y - k_y'\right)\right] \alpha_0\left(k_y'\right) \sinh\left[\kappa_0\left(k_y'\right) H\right] \bar{\tilde{E}}_0^{(g)}\left(k_y'\right)
\end{aligned}
\tag{6.49}
$$

We expect that the gain will be maximal near the synchronous point $(\omega_0, k_0, k_y = 0)$ where

$$
D\left(\omega_0, k_0, 0\right) = 0, \tag{6.50}
$$

$$
\omega_0 = \beta ck_0. \tag{6.51}
$$

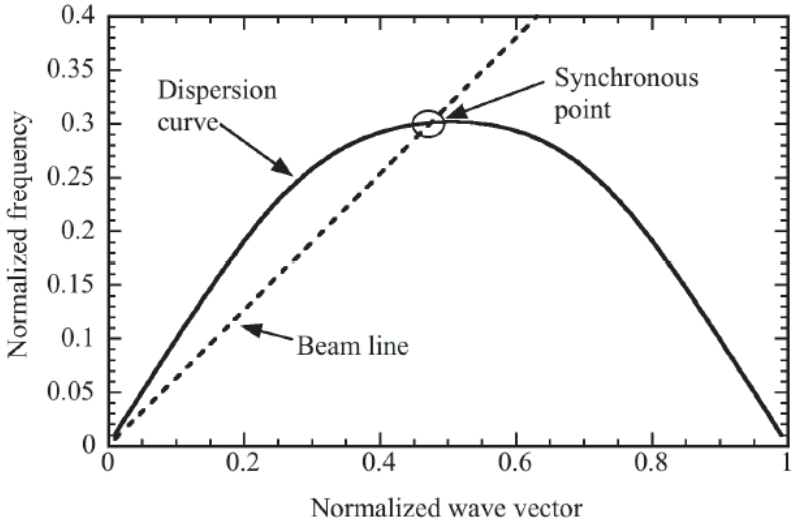

Figure 6.5: Grating dispersion curve and electron beamline. The synchronous point is $\omega/k = \beta c$ and the group velocity is $\beta_g = d\omega/dk$.

Noting that the dispersion function is symmetric in k_y, we expand as

$$D(\omega, k, k_y) \approx D_\omega \delta\omega + D_k \delta k + D_y \delta k_y^2, \tag{6.52}$$

where

$$\delta\omega = \omega - \omega_0, \tag{6.53}$$

$$\delta k = k - k_0, \tag{6.54}$$

$$\delta k_y = k_y, \tag{6.55}$$

and

$$D_\omega(\omega_0, k_0) = \frac{\partial D}{\partial \omega}(\omega_0, k_0, 0), \tag{6.56}$$

$$D_k(\omega_0, k_0) = \frac{\partial D}{\partial k}(\omega_0, k_0, 0), \tag{6.57}$$

$$D_y(\omega_0, k_0) = \frac{\partial D}{\partial k_y^2}(\omega_0, k_0, 0). \tag{6.58}$$

The derivatives D_ω and D_k are related by

$$\frac{dD}{dk} = 0 = \frac{\partial D}{\partial k} + \frac{\partial D}{\partial \omega}\frac{\partial \omega}{\partial k} = D_k + \beta_g c D_\omega, \tag{6.59}$$

where $\beta_g c = \partial\omega/\partial k$ is the group velocity. This allows us to rewrite the dispersion function as

$$D\left(\omega, k, k_y\right) \cong D_\omega\left(\delta\omega - \beta_g c\delta k\right) + D_y \delta k_y^2. \tag{6.60}$$

Because $k_y << k \approx O\left(\omega/c\right)$, we can make the approximations

$$\alpha_0\left(\omega, k, k_y\right) \approx \alpha_0\left(\omega_0, k_0, 0\right) = \frac{\omega_0}{\beta\gamma c}, \tag{6.61}$$

and

$$\kappa_0\left(\omega, k, k_y\right) \approx \kappa_0\left(\omega_0, k_0, 0\right) = i\frac{\omega_0}{c}, \tag{6.62}$$

near the sychronous point. We also note that

$$\omega - \beta c k = \delta\omega - \beta c\delta k. \tag{6.63}$$

Including these approximations, the dispersion relation (6.50) becomes

$$\begin{aligned}\left(\delta\omega - \beta c\delta k\right)^2 \left[D_\omega\left(\delta\omega - \beta_g c\delta k\right) + D_y\delta k_y^2\right]\bar{\tilde{E}}_0^{(g)}\left(k_y\right) = -\frac{\beta^3 c^2 W}{\pi A L}\frac{\omega_e^2}{\gamma^2\omega_0^2} \\ \times\tan\left(\frac{\omega_0}{c}H\right)\left[1 - \cos\left(k_0 A\right)\right]\int_{-\infty}^{\infty} dk_y' \mathrm{sinc}\left[\frac{W}{2}\left(k_y - k_y'\right)\right]\bar{\tilde{E}}_0^{(g)}\left(k_y'\right).\end{aligned} \tag{6.64}$$

This result may be compared to the 2-D theory of the SPFEL by taking the limit as $W \to \infty$ and subsequently evaluating at $k_y = 0$. In this limit, the sinc function behaves as a delta

function, selecting out the integrand value at $k_y' = k_y = 0$. Evaluaing (6.65) gives

$$\begin{aligned}(\delta\omega - \beta c\delta k)^2 (\delta\omega - \beta_g c\delta k) \\ = \quad -\frac{2\beta^3 c^2}{ALD_\omega}\frac{\omega_e^2}{\gamma^2\omega_0^2}\tan\left(\frac{\omega_0}{c}H\right)\left[1-\cos\left(k_0 A\right)\right],\end{aligned} \tag{6.65}$$

which matches the dispersion relation for the 2-D theory [63–65].

Of more interest is the limit in which the electron beam is very narrow compared to the mode width. In this case, $\mathrm{sinc}\left[\frac{W}{2}\left(k_y - k_y'\right)\right] \approx 1$, and the remaining integral is recognized as $\sqrt{2\pi}\bar{E}_0{}^{(g)}(0)$. The dispersion relation is simplified by the substitution

$$\Delta k_y^2 = \frac{D_\omega}{D_y}\left(\delta\omega - \beta_g c\delta k\right). \tag{6.66}$$

The roots of this equation are $\Delta k_y^{(+)}$ and $\Delta k_y^{(-)} = -\Delta k_y^{(+)}$, which lie in the right half and left half of the complex plane, respectively. Solving (6.65) for $\bar{\bar{E}}_0^{(g)}$ and inverting the Fourier transform, we get

$$\begin{aligned}\bar{E}_0^{(g)}(y) = -\frac{\beta^3 c^2 W}{\pi ALD_y}\frac{\omega_e^2}{\gamma^2\omega_0^2}\tan\left(\frac{\omega_0}{c}H\right) \\ \times\left[1-\cos\left(k_0 A\right)\right]\frac{\bar{E}_0^{(g)}(0)}{\left(\delta\omega - \beta c\delta k\right)^2}\int_{-\infty}^{\infty} dk_y \frac{e^{-ik_y y}}{\Delta k_y^2 + k_y^2}.\end{aligned} \tag{6.67}$$

The integrand has poles at $i\Delta k_y^{(+)}$ and $i\Delta k_y^{(-)} = -i\Delta k_y^{(+)}$, which lie above and below the real axis respectively. The integral is evaluated using contour integration and the residue theorem. For $y > 0$ the contour is closed in the lower half plane, so the integrand vanishes along the curved segment. Integrating clockwise around the contour, we find

$$\bar{E}_0^{(g)}(y) = \frac{\beta^3 c^2 W}{ALD_y}\frac{\omega_e^2}{\gamma^2\omega_0^2}\tan\left(\frac{\omega_0}{c}H\right)\left[1-\cos\left(k_0 A\right)\right]\frac{\bar{E}_0^{(g)}(0)}{\left(\delta\omega - \beta c\delta k\right)^2}\frac{e^{\Delta k_y^{(-)} y}}{\Delta k_y^{(-)}}. \tag{6.68}$$

The pole in the lower half plane has $\mathrm{Im}\left(i\Delta k_y^{(-)}\right) = \mathrm{Re}\left(\Delta k_y^{(-)}\right) < 0$; therefore, the field

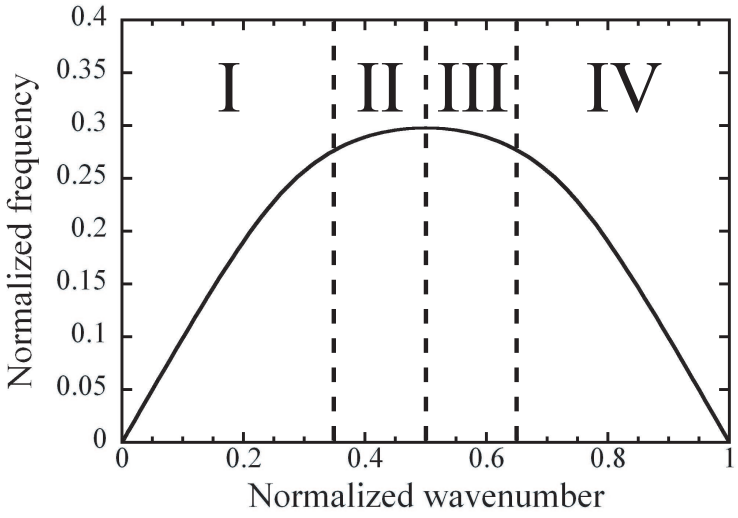

Figure 6.6: The number of physically allowed roots changes depending on the operating point, (ω, k). Regions I, II, III, and IV have three, two, two, and three roots respectively.

vanishes at $y = \infty$, as required. Similarly, for $y < 0$ the contour is closed in the upper half plane and $\mathrm{Im}\left(i\Delta k_y^{(+)}\right) = \mathrm{Re}\left(\Delta k_y^{(+)}\right) > 0$, and the field vanishes at $y = -\infty$.

Evaluating (6.68) at $y = 0$ we arrive at the dispersion relation for the narrow beam case,

$$(\delta\omega - \beta c\delta k)^2 \left[\frac{D_\omega}{D_y}(\delta\omega - \beta_g c\delta k)\right]^{\frac{1}{2}} = \Delta, \tag{6.69}$$

where

$$\Delta = \frac{\beta^3 c^2 W}{ALD_y}\frac{\omega_e^2}{\gamma^2\omega_0^2}\tan\left(\frac{\omega_0}{c}H\right)\left[1 - \cos\left(k_0 A\right)\right], \tag{6.70}$$

and the sign of $\left[\frac{D_\omega}{D_y}(\delta\omega - \beta_g c\delta k)\right]^{\frac{1}{2}} = \Delta k_y^{(-)}$ is chosen so that its real part is negative. Calculations show that D_ω is negative, irrespective of k, but D_y changes sign such that $D_y > 0$ near the center of the Brillouin zone $(k/K = 1/2)$ and $D_y < 0$ towards the edges of the zone $(k = 0, K)$. This subdivides the dispersion curve into the four distinct regions pictured in Figure 6.6. We now consider the amplifier and oscillator regimes of the SPFEL.

Amplifier: When the device operates as a steady-state amplifier, $\delta\omega = 0$ and β_g is positive. In region II, the dispersion relation becomes

$$\delta k^{\frac{5}{2}} = \Gamma \tag{6.71}$$

where

$$\Gamma = \frac{\Delta}{\beta^2 c^2} \left| \frac{D_y}{D_\omega \beta_g c} \right|^{\frac{1}{2}}. \tag{6.72}$$

We find the roots of (6.71) to be

$$\delta k_n = \Gamma^{\frac{2}{5}} e^{i\frac{4}{5}n\pi}. \tag{6.73}$$

Similarly, for region I, the roots are given by

$$\delta k_n = \Gamma^{\frac{2}{5}} e^{i\left(\frac{4}{5}n\pi + \frac{\pi}{5}\right)} \tag{6.74}$$

The solutions from (6.73) are plotted on the complex plane in Figure 6.7. To relate δk and Δk_y, we rearrange (6.69) as

$$\delta k^2 = \frac{1}{\Delta k_y^{(-)}} \frac{\Delta}{\beta^2 c^2}. \tag{6.75}$$

Valid roots obey the condition $\mathrm{Re}\,(\Delta k_y) < 0$, i.e. $\mathrm{Re}\,(\delta k^2) < 0$. For region II, only two roots satisfy this condition, $n = 2, 3$. From Figure 6.8 we see that these are slow waves, i.e. they have a phase velocity lower than that of the synchronous point. In region I, however, there are three physically allowed roots including one fast wave solution. It is surprising that a fast wave is allowed in a gain-guided system.

In region II, the $n = 3$ root has loss and the $n = 2$ has gain. The gain for the $n = 2$ root is given by

$$\mu_{3D} = -\mathrm{Im}\,(\delta k_2) = \Gamma^{\frac{2}{5}} \sin\left(\frac{2}{5}\pi\right). \tag{6.76}$$

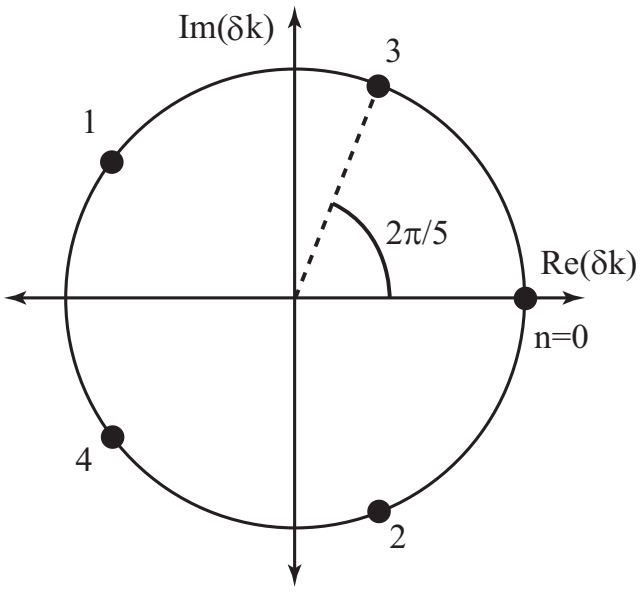

Figure 6.7: Roots of the narrow-beam dispersion relation.

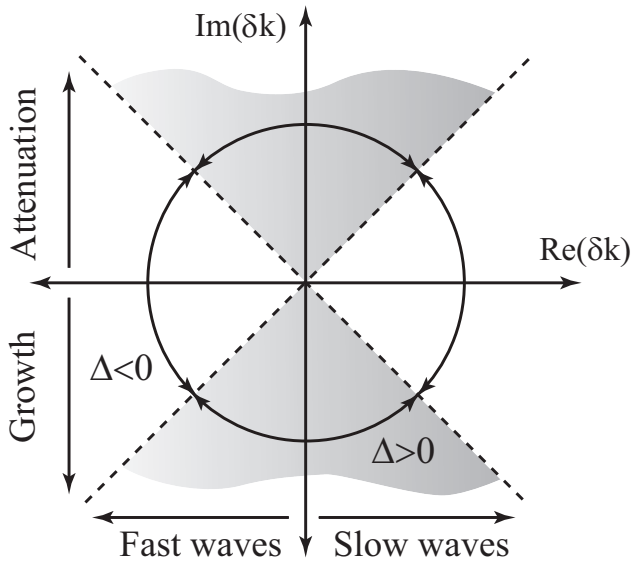

Figure 6.8: Selection diagram for allowed roots.

The transverse decay rate of the field is found from (6.66) to be

$$\Delta k_y^{(-)} = -\left(\left|\frac{D_\omega}{D_y}\beta_g\right| c\right)^{\frac{1}{2}} \Gamma^{\frac{1}{5}} e^{i\frac{4}{5}\pi}, \tag{6.77}$$

and the corresponding $1/e$ width of the optical mode is

$$\Delta y = -\frac{2}{\mathrm{Re}\left(\Delta k_y^{(-)}\right)} = 2\left(\left|\frac{D_\omega}{D_y}\beta_g\right| c\right)^{-\frac{1}{2}} \Gamma^{-\frac{1}{5}} \cos\left(\frac{\pi}{5}\right). \tag{6.78}$$

The prefactors of (6.77) are positive real, and upon examination we see that the real part of $\Delta k_y^{(-)}$ is indeed negative, as required for the fields to vanish at $y = \infty$.

From (6.76) we see that the gain length and the electron-beam current are related by

$$\mu = \frac{1}{Z_g} \propto n_e^{\frac{2}{5}} \propto I^{\frac{2}{5}}. \tag{6.79}$$

To understand this result we consider the relationship from previous two-dimensional analyses [63–65], given by

$$\frac{1}{Z_g} \propto n_e^{\frac{1}{3}} \propto I^{\frac{1}{3}}. \tag{6.80}$$

In the three-dimensional case, the average electron density over the area of the mode is of order

$$n_e \approx \frac{I}{\Delta x \Delta y \beta c} \propto \frac{I}{\sqrt{Z_g}}. \tag{6.81}$$

Combining (6.80) and (6.81), we get

$$\frac{1}{Z_g} \propto I^{\frac{2}{5}}. \tag{6.82}$$

The relationship given in (6.82) is simply understood to be the manifestation of gain guiding in the SPFEL. As an example we consider the grating and beam described in Table 6.1. For this particular grating the Bragg point $(\beta_g = 0)$ is located at $V_{Bragg} \approx$

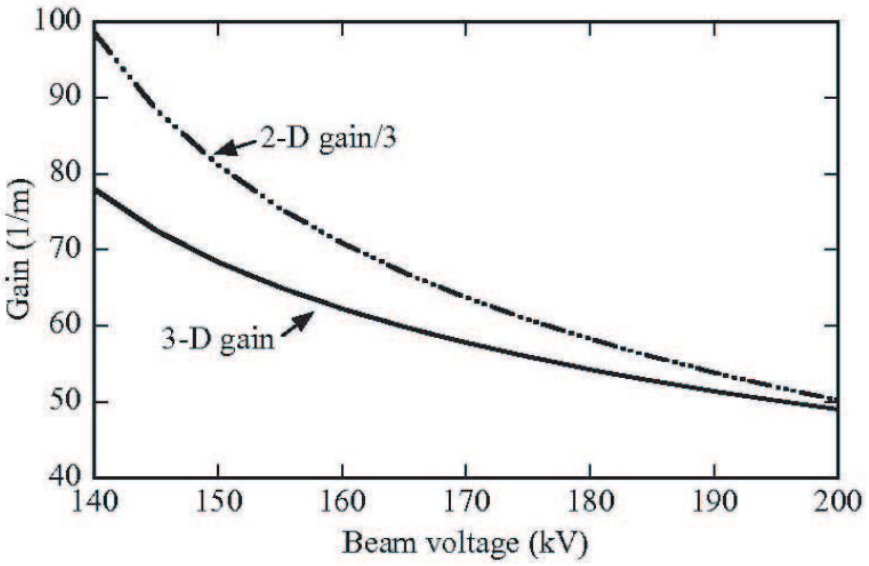

Figure 6.9: Gain coefficient (1/m) vs. beam voltage (V)

$126\mathrm{kV}$. For an operating voltage of 150 kV, the scale height of the evanescent wave is calculated to be $\Delta x \approx 38\mu\mathrm{m}$. To compensate for errors introduced in our assumption that the beam stretches from the grating top to infinity, we scale the electron density by the filling factor [74]

$$F_{fill} = e^{-\frac{h_e - W/2}{\Delta x}} - e^{\frac{h_e + W/2}{\Delta x}}, \tag{6.83}$$

where h_e is the height of the beam centroid relative to the grating top, and $\Delta x = 1/2\alpha_0\,(0) = \beta\gamma\lambda/4\pi$ is the intensity scale height for the synchronous evanescent wave. For this case the filling factor is $F_{fill} \approx 0.8$. The three-dimensional gain is plotted in Figure 6.9, along with the two-dimensional gain which has been scaled down by a factor of three to appear on the same graph. The transverse profile of the electric field is given in Figure 6.10, and the $1/e$ mode width is found to be $\Delta y \approx 4.4$ mm. By examining the geometry of this mode, it is clear that the initial assumptions made concerning its dimensions are justified.

Oscillator: When the synchronous point is to the right of the Bragg point, the group velocity of the evanescent mode is negative. This allows energy exchanged in the beam-wave interaction to be transported to the up-stream end of the grating. This serves as an

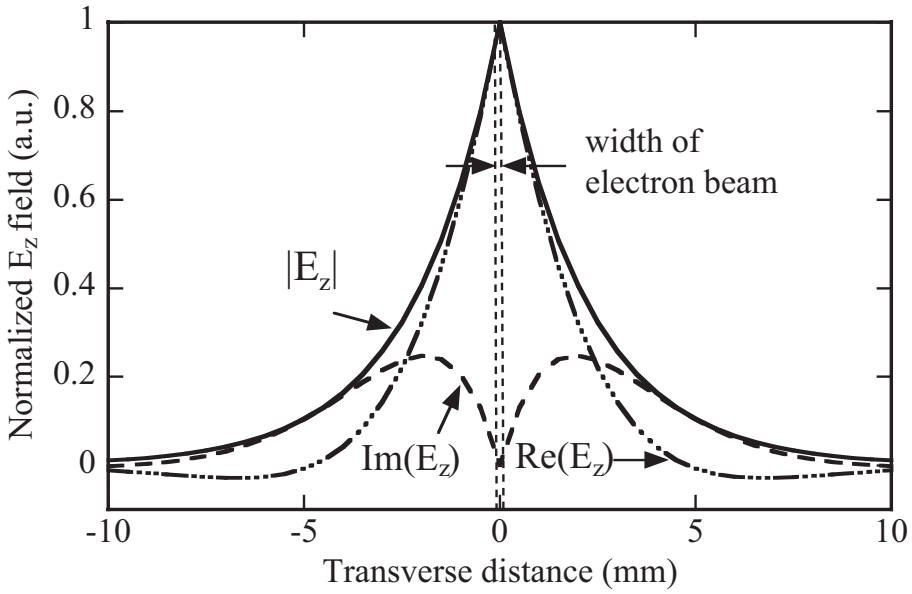

Figure 6.10: Transverse profile of the longitudinal electric field strength.

intrinsic form of feedback and, provided that the beam current exceeds the so-called start current, allows the device to oscillate. For a solution to exist in the oscillator case, three boundary conditions must be satisfied in conjunction with the dispersion relation (6.69). The electron beam must be free of density and velocity modulations at the upstream end of the grating, and the input optical field at the downstream end must vanish [64, 65]. These boundary conditions are satisfied by interference of the three waves that compose the mode. We find that while region IV has three physically allowed roots, only two waves are admitted in region III. It is not clear how all three boundary conditions may be satisfied without the presence of a third wave. PIC code simulations do not provide a clear answer to this problem since they are influenced by the finite width of the grating even without sidewalls [69]. Furthermore, solutions to the inhomogeneous system can have different transverse widths due to the presence of gain guiding. While beyond the scope of this work, it may be possible to use additional waves supported by the grating to satisfy the boundary conditions on the input field for all y. Based on our calculations of gain dilution by diffraction effects in the amplifier case, it seems unlikely that functional SPFELs will be

constructed without some form of mode confinement. This viewpoint is supported by the PIC simulations of Li [69], which show a significant increase in the oscillator start current.

VI.3.2 **Three-dimensional theory of the confined-mode SPFEL**

In the previous section we found that transverse diffraction effects reduce the strength of the beam-wave interaction. The reduced overlap between the electron beam and the optical mode effectively dilutes the gain medium and increases the device's gain length (amplifier) and start current (oscillator). The competition between gain guiding and diffraction results in a mode width on the order of several millimeters. Adding metallic sidewalls with submillimeter spacing confines the optical mode and mitigates the effects of transverse diffraction. In this section the theory of such a confined-mode device is presented, including amplifier and oscillator operation. The general approach is similar to that of section VI.3.

Dispersion: As before, we begin by expressing the fields in the grooves and above the grating. In previous analyses it was found that the lowest order longitudinal term, a constant, was sufficient for describing the groove fields. The fields may then be expanded as Fourier series in the y (transverse) direction as

$$E_z^{(g)} = \sum_{r=0}^{\infty} E_r^{(g)} \sin\left[\kappa_r \left(x+H\right)\right] \cos\left[\left(2r+1\right)\frac{\pi}{G}y\right] e^{-i\omega t} \tag{6.84}$$

$$H_y^{(g)} = \sum_{r=0}^{\infty} H_r^{(g)} \cos\left[\kappa_r \left(x+H\right)\right] \cos\left[\left(2r+1\right)\frac{\pi}{G}y\right] e^{-i\omega t} \tag{6.85}$$

where G is the spacing between the grating sidewalls. From the wave equation we have

$$\kappa_r^2 + \left(2r+1\right)^2 \frac{\pi^2}{G^2} - \frac{\omega^2}{c^2} \tag{6.86}$$

From the Maxwell equations the coefficients are related by

$$\frac{\omega^2}{c^2} H_s^{(g)} = i\omega\kappa_s\epsilon_0 E_s^{(g)}. \tag{6.87}$$

As before, the fields above the grating can be expanded as Floquet series of the form

$$E_z^{(e)} = \sum_{r=0}^{\infty}\sum_{p=-\infty}^{\infty} E_{rp}^{(e)} e^{-\alpha_{rp}x}\cos\left[(2r+1)\frac{\pi}{G}y\right] e^{ipKz} e^{i(kz-\omega t)} \tag{6.88}$$

$$H_y^{(e)} = \sum_{r=0}^{\infty}\sum_{p=-\infty}^{\infty} H_{rp}^{(e)} e^{-\alpha_{rp}x}\cos\left[(2r+1)\frac{\pi}{G}y\right] e^{ipKz} e^{i(kz-\omega t)} \tag{6.89}$$

The electron beam is again treated as a relativistic moving plasma dielectric. The electron beam's index of refraction is the same as in section VI.3, and the approximation $\omega_e'^2 << \left(k' + pK'\right)^2 c^2 - \omega_p'^2$ is still valid. The wave equation gives

$$\alpha_{rp}^2 - (2r+1)^2\frac{\pi^2}{G^2} - (k+pK)^2 + \frac{\omega^2}{c^2} = 0. \tag{6.90}$$

Invoking the Lorentz invariance of the displacement D_z and the Maxwell equations we have

$$\sum_{r=0}^{\infty}\sum_{p=-\infty}^{\infty} H_{rp}^{(e)}\left[\alpha_{rp}^2 - (2r+1)^2\frac{\pi^2}{G^2}\right] e^{-\alpha_{rp}x}\cos\left[(2r+1)\frac{\pi}{G}y\right] e^{ipKz} e^{i(kz-\omega t)} \tag{6.91}$$
$$= \epsilon_0\sum_{r=0}^{\infty}\sum_{p=-\infty}^{\infty} E_{rp}^{(e)}\left(1 - \frac{\omega_e'^2}{\omega_p'^2}\right)(i\omega\alpha_{rp})\, e^{-\alpha_{rp}x}\cos\left[(2r+1)\frac{\pi}{G}y\right] e^{ipKz} e^{i(kz-\omega t)}.$$

Multiplying by $\cos\left[(2s+1)\frac{\pi}{G}y\right] e^{-i(k+qK)z}$ and integrating over the grating width and grating period, we have

$$H_{sq}^{(e)}\left[(k+pK)^2 - \frac{\omega^2}{c^2}\right] = i\omega\epsilon_0\left[\alpha_{sq}E_{sq}^{(e)} - \frac{\omega_e'^2}{\omega_p'^2}\sum_{r=0}^{\infty}\alpha_{rq}J_{rs}E_{rq}^{(e)}\right]. \tag{6.92}$$

J_{rs} describes the coupling between transverse modes, mediated by the electron beam, and

is given by

$$J_{rs} = \frac{W}{G}\left\{ sinc\left[(r+s+1)\,\pi\frac{W}{G}\right] + sinc\left[(r-s)\,\pi\frac{W}{G}\right]\right\}. \tag{6.93}$$

Examining (6.36), we see that the susceptibility is divergent near the synchronous point for only the $p = 0$ component. Accordingly (6.92) may be simplified as

$$H_{sq}^{(e)}\left[(k+pK)^2 - \frac{\omega^2}{c^2}\right] = i\omega\epsilon_0\left[\alpha_{sq}E_{sq}^{(e)} - \frac{\omega_e}{\gamma^3\left(\omega-\beta ck\right)^2}\sum_{r=0}^{\infty}\alpha_{rq}J_{rs}E_{rq}^{(e)}\right]. \tag{6.94}$$

Matching (6.84) and (6.88) at the $x = 0$ interface, multiplying by $e^{-i(k+qK)z}$, and integrating over the grating period, we get

$$E_{sq}^{(e)} = K_q \sin\left[\kappa_s H\right] E_s^{(q)} \tag{6.95}$$

where

$$K_q = i\frac{e^{-i(k+qK)A}-1}{(k+qK)\,L} \tag{6.96}$$

Similarly, matching (6.85) and (6.89) and integrating over the groove width, we get

$$H_s^{(g)} A\cos\left[\kappa_s H\right] = L\sum_{p=-\infty}^{\infty} K_p^* H_{sp} \tag{6.97}$$

Combining (6.87), (6.94), (6.95) and (6.97) gives the matrix equation

$$D_s E_s^{(g)} = \sum_{r=0}^{\infty} R_{sr} E_r^{(g)} \tag{6.98}$$

where

$$D_s\left(\omega,k\right) = 1 + \frac{L}{A}\tan\left(\kappa_s H\right)\sum_{p=-\infty}^{\infty}\frac{\omega^2 K_p^* K_p}{\omega^2 - \left(k+pK\right)^2 c^2}\frac{\alpha_{sp}}{\kappa_s} \tag{6.99}$$

is the dispersion function for the s^{th} field component of the empty grating and the matrix

elements

$$R_{sr}\left(\omega,k\right)=\frac{L}{A}\frac{\omega^{2}K_{0}^{*}K_{0}}{\omega^{2}-k^{2}c^{2}}\frac{\omega_{e}^{2}}{\gamma^{3}\left(\omega-\beta ck\right)}\frac{\alpha_{r0}}{\kappa_{s}}J_{rs}\frac{\sin\left(\kappa_{r}H\right)}{\cos\left(\kappa_{s}H\right)} \tag{6.100}$$

describe the coupling between transverse orders of the field.

Table 6.2: Example grating and beam parameters used in confined-mode-theory calculations

Grating period	157 μm
Groove width	61 μm
Groove depth	226 μm
Grating length	7.85 mm
Grating width	500 μm
E-beam width/height	44 μm
E-beam centroid height from grating top	35 μm
E-beam voltage	30 kV
E-beam current	10 mA

Figure 6.11 compares the dispersion relation from the two-dimensional theory with the first three transverse orders of the confined-mode theory for a grating with the parameters in Table 6.2. Additionally, electron beamlines for 30, 34, and 38 kV are shown, and we note that the synchronous point for each energy corresponds to $(\beta_g > 0)$ for the two-dimensional theory and $(\beta_g < 0)$ for the confined-mode theory.

The matrix equation must be solved numerically, and to facilitate this, we recast it in the form of the eigenvalue equation

$$\lambda\epsilon_{s}=\sum_{r=0}^{\infty}T_{sr}\epsilon_{r} \tag{6.101}$$

where

$$\epsilon_{r} = D_{r}E_{r}^{(g)} \tag{6.102}$$

$$T_{sr} = \frac{R_{sr}}{D_{r}}. \tag{6.103}$$

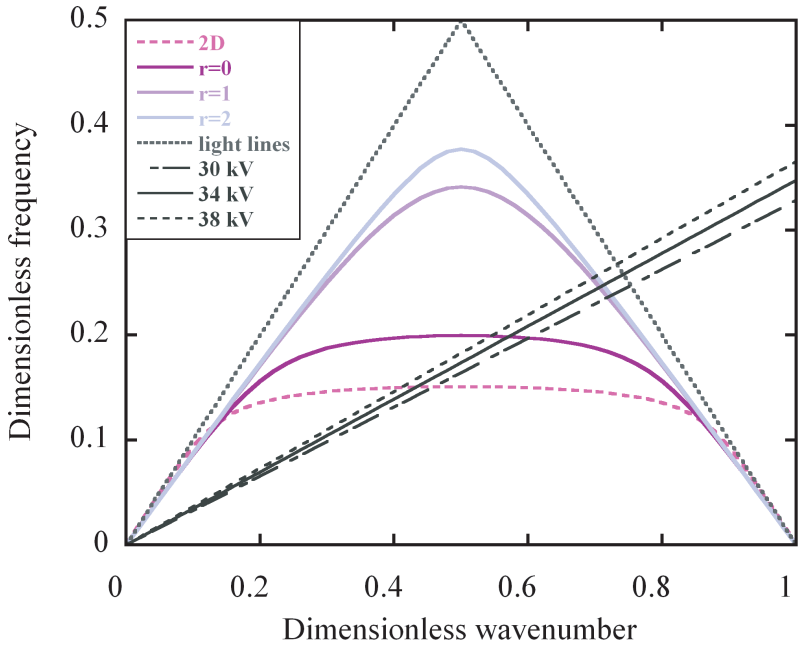

Figure 6.11: Dispersion relation for 2-D, and 3-D confined mode theories. 30, 34, and 38 kV electron beamlines are included.

The dispersion relation is then

$$\lambda(\omega, k) - 1 = 0. \tag{6.104}$$

This can be solved with a root finding algorithm. To minimize gain dilution, the sidewalls are separated on the order of the wavelength of the optical mode. In this case the $s = 0$ mode is widely separated in frequency from the higher order components. To solve the exact multi-mode system, (6.101), we require an initial guess for the complex wavenumber and frequency shifts. To obtain this initial value, we simplify the system by allowing the electron-beam width to be comparable to the grating width; The coupling constants (J_{rs}) for $r \neq s$ are small and the matrix, R_{sr}, is largely diagonal. In this case the $r = s = 0$ mode should dominate the interaction and we may simplify the Dispersion relation as

$$D_0(\omega, k) = R_{00}(\omega, k). \tag{6.105}$$

As before, we Taylor expand the empty grating dispersion function near the synchronous

point as

$$D_0(\omega, k) = D_\omega \delta\omega + D_k \delta k. \tag{6.106}$$

Writing D_k in terms of D_ω, (6.106) becomes

$$D_0(\omega, k) \approx D_\omega (\delta\omega - \beta c \delta k) \tag{6.107}$$

and the dispersion relation is then

$$(\delta\omega - \beta c\delta k)^2 (\delta\omega - \beta_g c\delta k) = \frac{\omega_e^2}{\gamma^3} \frac{Q_{00}(\omega_0, k_0)}{D_\omega(\omega_0, k_0)} \tag{6.108}$$

where

$$Q_{sr}(\omega, k) = \frac{L}{A} \frac{\omega^2 K_0^* K_0}{\omega^2 - k^2 c^2} \frac{\omega_e^2}{\gamma^3} \frac{\alpha_{r0}}{\kappa_s} J_{rs} \frac{\sin(\kappa_r H)}{\cos(\kappa_s H)}. \tag{6.109}$$

We now consider the cases of amplifier ($\beta_0 > 0$) and oscillator ($\beta_0 < 0$) operation.

Amplifier: When the device operates as a steady state amplifier, the maximum gain occurs at $\delta\omega = 0$ [64]. The dispersion relation reduces to

$$\delta k^3 = -\frac{\omega_e^2}{\gamma^3 \beta^2 c^3 \beta_0} \frac{Q_{00}(\omega_0, k_0)}{D_\omega(\omega_0, k_0)} \tag{6.110}$$

Calculations show that Q_{00} and D_ω are negative irrespective of operating voltage. The roots of (6.110) are then

$$\delta k_n = \left| \frac{\omega_e^2}{\gamma^3 \beta^2 c^3 \beta_0} \frac{Q_{00}(\omega_0, k_0)}{D_\omega(\omega_0, k_0)} \right|^{\frac{1}{3}} e^{i\frac{2\pi}{3}n} \tag{6.111}$$

Examining Figure 6.12 we see that only the $n = 2$ root has gain; the gain is given by

$$-\mathrm{Im}(\delta k_2) = \mu = \frac{\sqrt{3}}{2} \left| \frac{\omega_e^2}{\gamma^3 \beta^2 c^3 \beta_0} \frac{Q_{00}(\omega_0, k_0)}{D_\omega(\omega_0, k_0)} \right|^{\frac{1}{3}}. \tag{6.112}$$

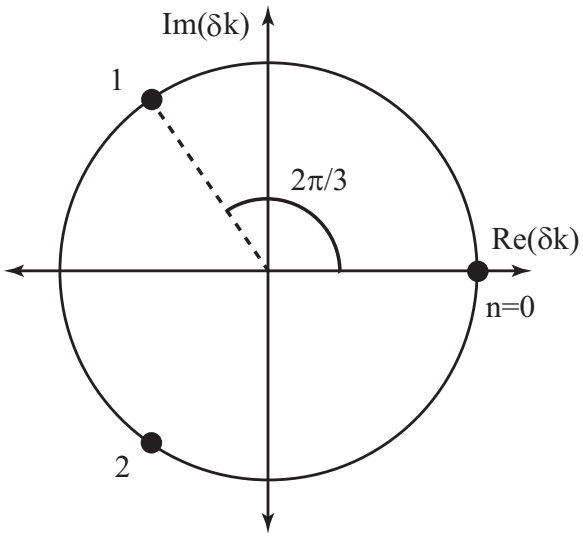

Figure 6.12: Roots of the dispersion relation for amplifier operation of the confined-mode SPFEL.

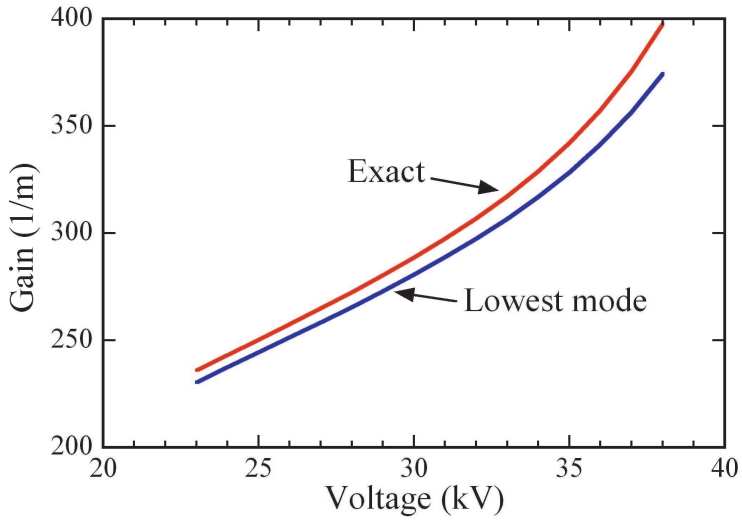

Figure 6.13: Comparison of the exact and approximate solutions for the gain.

We now have an approximate solution to (6.101) which can be used to seed an numerical computation of the multi-mode gain. A comparison of the approximate and exact results is shown in Figure 6.13. The close agreement suggests that the interaction is indeed dominated by the lowest order mode, and the approximate dispersion relation (6.108) is sufficiently accurate.

Oscillator: For oscillator operation $(\beta_0 < 0)$ the boundary conditions on the electron beam and the radiation field are discussed in the previous section. The electron beam must be free of density and velocity modulations at the upstream end of the grating, and the input optical field at the downstream end must vanish. In a gain guided system, the optical mode width depends on that particular mode's gain. If multiple orders with different transverse profiles are used to describe the interaction, complications arise in satisfying the aforementioned boundary conditions. However, as found in the preceeding analysis, the interaction is typically dominated by the lowest order mode. Each of the three allowed roots have the same transverse profile and the boundary conditions may be satisfied as in previous two-dimensional analyses [64, 65]. During oscillator operation these three waves become frequency locked, having the same $\delta\omega$. However, each wave may take on a different δk, interfering with one another to satisfy the boundary conditions at the ends of the grating.

To simplify the analysis we define the dimensionless variables

$$\delta_j = \left| \frac{\gamma^3 \beta^2 c^3 \beta_0}{\omega_e^2} \frac{D_\omega\left(\omega_0, k_0\right)}{Q_{00}\left(\omega_0, k_0\right)} \right|^{\frac{1}{3}} \left(\frac{\delta\omega}{\beta c} - \delta k_j \right) \tag{6.113}$$

$$\kappa = \left| \frac{\gamma^3 \beta^2 c^3 \beta_0}{\omega_e^2} \frac{D_\omega\left(\omega_0, k_0\right)}{Q_{00}\left(\omega_0, k_0\right)} \right|^{\frac{1}{3}} \left(\frac{1}{\beta} - \frac{1}{\beta_0} \right) \delta\omega \tag{6.114}$$

where $j = 1, 2, 3$ corresponds to the three roots. The dispersion relation (6.108) may then be written in the dimensionless form

$$\delta_j^2 \left(\delta_j - \kappa\right) + 1 = 0. \tag{6.115}$$

As in the two-dimensional theory [64], the boundary conditions are given by

$$\begin{vmatrix} 1/\delta_1^2 & 1/\delta_2^2 & 1/\delta_3^2 \\ 1/\delta_1 & 1/\delta_2 & 1/\delta_3 \\ e^{-i\xi\delta_1} & e^{-i\xi\delta_2} & e^{-i\xi\delta_3} \end{vmatrix} = 0 \tag{6.116}$$

where

$$\xi = \left| \frac{\omega_e^2}{\gamma^3 \beta^2 c^3 \beta_0} \frac{Q_{00}\left(\omega_0, k_0\right)}{D_\omega\left(\omega_0, k_0\right)} \right|^{\frac{1}{3}} Z = \frac{2}{\sqrt{3}} \mu Z \tag{6.117}$$

is the dimensionless gain. By solving the system numerically for $(\kappa, \delta_1, \delta_2, \delta_3)$ as a function of ξ, we can determine the growth rate $(\mathrm{Im}\left(\delta\omega\right))$ and the start current for the oscillator.

Results: The confined-mode theory may be readily compared with PIC code simulations by D. Li et al [69]. While the grating used in the simulations and our analytic theory is identical, a few differences regarding the electron beam should be noted. The simulations use a finite beam with a circular cross section extending from $h_b = 13$ $\mu\mathrm{m}$ to $h_t = 57$ $\mu\mathrm{m}$ while the theory assumes a beam which extends to $x = \infty$. To calculate the plasma frequency, we use a square beam with the same cross-sectional area as that of the simulations. A filling factor corrects for the finite nature of the beam, giving an effective plasma frequency of

$$\omega_{eff} = \sqrt{F_{fill}}\omega_e = \left[e^{-2h_b\alpha_{00}} - e^{-2h_f\alpha_{00}}\right]^{\frac{1}{2}} \omega_e \tag{6.118}$$

For the parameters of Table 6.2 the filling factor is $F \approx 0.5$. The simulations also utilize a strong axial magnetic field to confine the electron beam. The magnetic field further reduces the effective plasma frequency by a factor of $1/\sqrt{2}$ [74]. Figure 6.14 presents a comparison of theory and simulations [69] for the growth rate of the $r = 0$ evanescent mode as a function of the electron beam current.

VI.4 **Theoretical Analysis of the Vermont Photonics Device**

Recently, we have collaborated with Vermont Photonics to test the confined-mode SPFEL theory. There were several primary objectives of these experiments: to measure a non-linear emission regime concurrent with the spectral modification discussed in section VI.1, to observe the spectrum of excited evanescent modes, and to investigate the possibility that a GHz electron beam instability has been responsible for the observed non-linearity

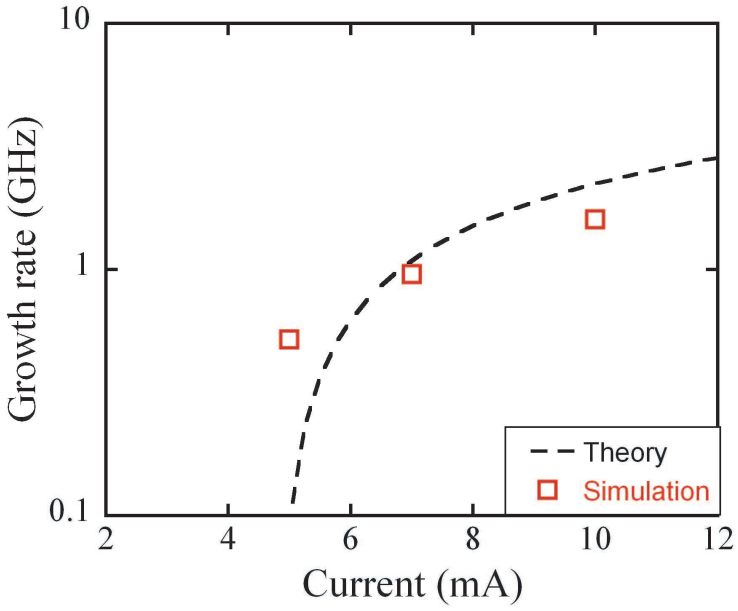

Figure 6.14: Comparison of the analytic confined-mode theory with simulations by D. Li.

thus far. We hoped to confirm lasing (oscillator) in this system, but were not successful in this. The grating parameters used in these experiments are given in Table 6.3. The experimental arrangement is summarized in Figures 6.15, 6.16, and 6.17. The grating

Table 6.3: Parameters of the grating used in the collaborative experiments with Vermont Photonics

Grating period	155 μm
Groove width	51 μm
Groove depth	218 μm
Grating length	7.85 mm
Grating width	500 μm

is bordered by vertical sidewalls that transition into long angled wings to improve the transport efficiency of THz radiation to the output window. The primary collector for the THz radiation is an off-axis paraboloid that can be scanned along the length of the grating. The system is aligned using a pair of autocollimators such that radiation emitted near the grating surface is collimated and directed to the output window. Additionally, a planar reflector that is optimized for directing superradiant emission to the output window can

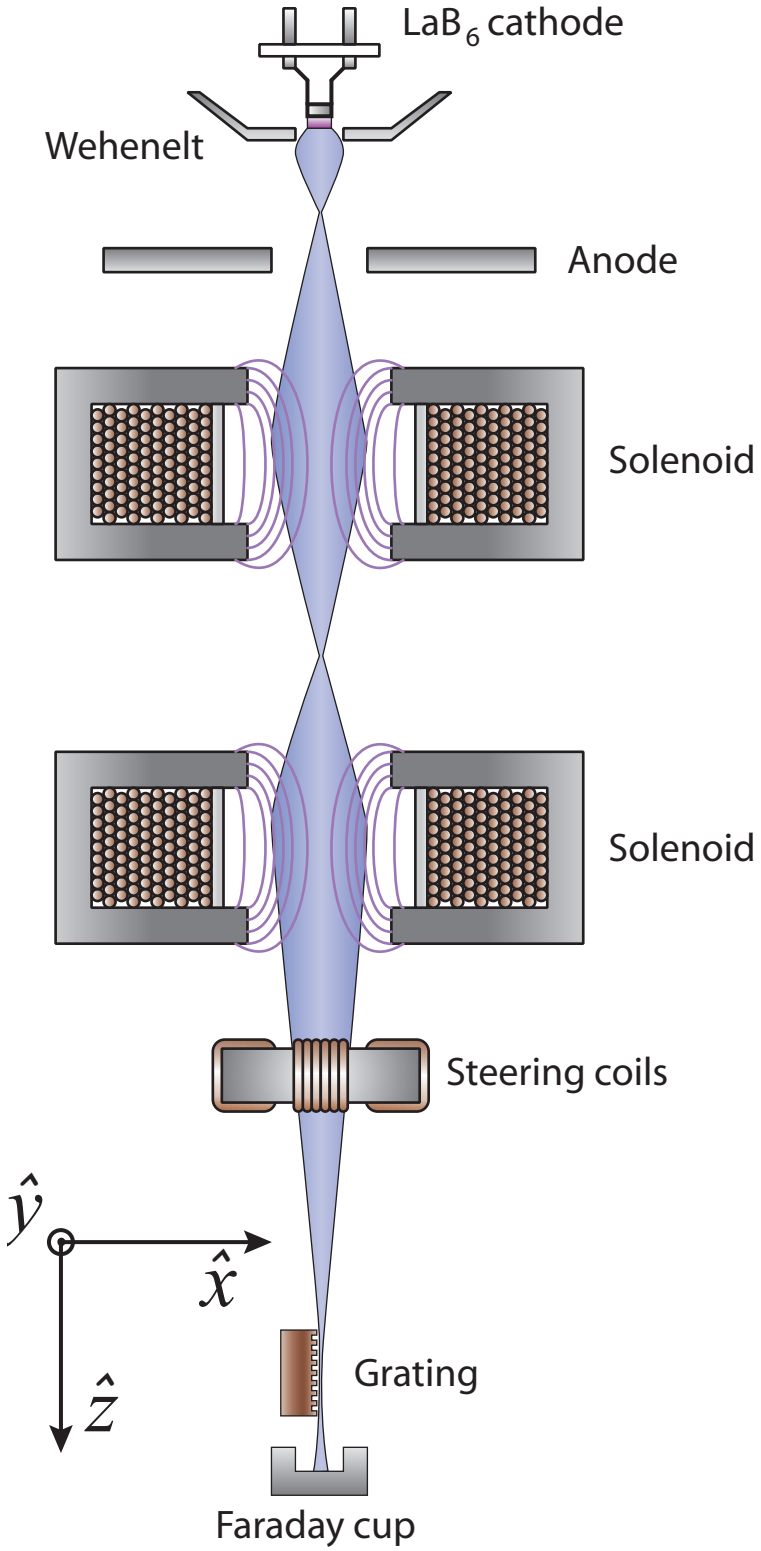

Figure 6.15: Schematic representation of the Vermont Photonics SPFEL.

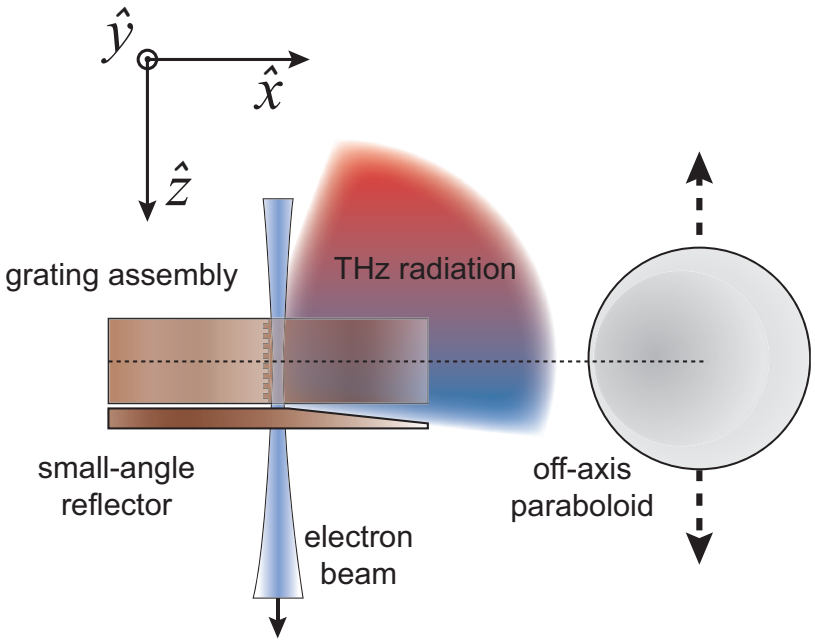

Figure 6.16: Interaction region detail in the Vermont Photonics experimental arrangement.

be added to the downstream end of the grating. This is useful when the superradiant SPR happens to be emitted at foward angles. The radiation is detected with a Helium cooled Silicon bolometer from IR labs, and the spectral content is obtained with an automated Michelson interferometer. The achievable spectral resolution is typically $\sim 0.2\ \mathrm{cm}^{-1}$, and while the minimum detectable power is ~ 1 nW, ~ 30 nW is required for accurate spectral analysis.

In previous collaborative experiments with Vermont Photonics we observed for the first time the evanescent wave in a Smith-Purcell device. The parameters of the grating from these experiments are given in Table 6.3. Sample spectra are given in Figure 6.18. As expected, the $s = 0$ evanescent-wave signal is strongest when the collector system is centered on the upstream end of the grating. The reader should note the absence of higher transverse order modes in these spectra. PIC simulations, like those shown in Figure 6.19 [68], provide an excellent visualization of the scattering of these evanescent waves from the ends of the grating.

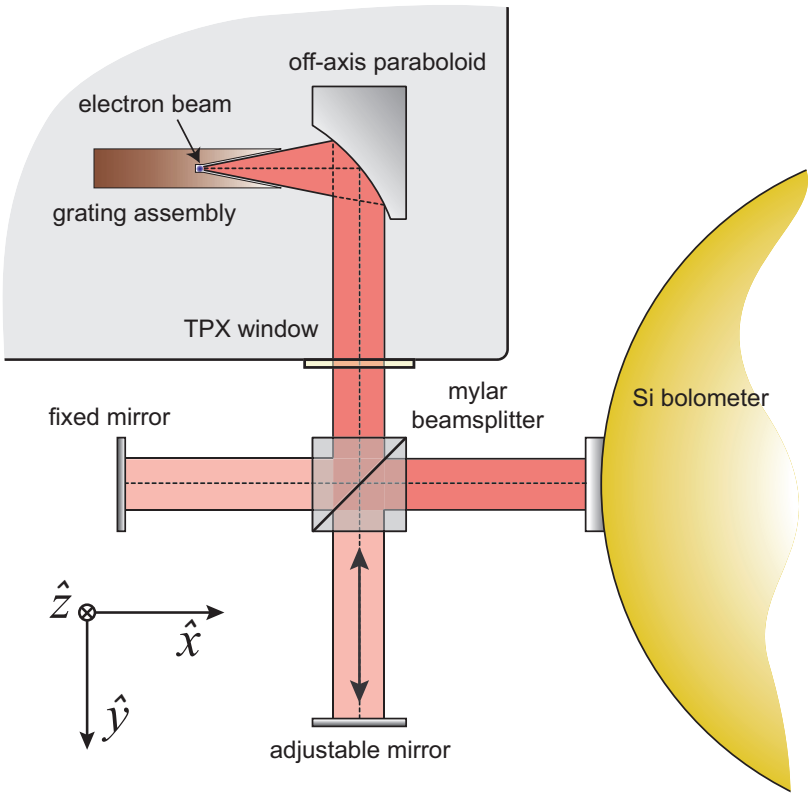

Figure 6.17: Schematic of the THz collector and interferometer arrangement in the Vermont Photonics experiments.

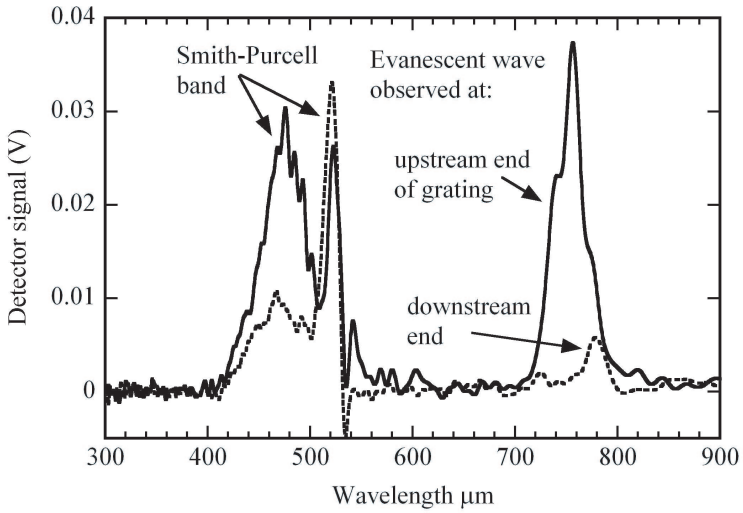

Figure 6.18: Spectra taken with the collection optics centered above the upstream (solid) and downstream (dotted) ends of the grating. The intensity difference between the two positions is indicative of a backward group velocity for the evanescent wave.

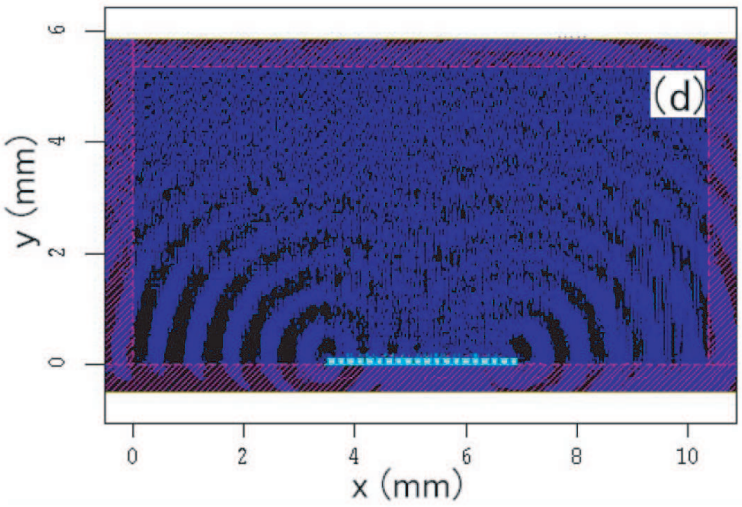

Figure 6.19: The impedance mismatch at the grating ends causes scattering of the evanescent modes [68].

In the most recent experiments, we have observed for the first time the $s = 1$ evanescent mode. It was believed that the transfer of energy from the electron beam to the higher order modes would be weak due to their much higher group velocity. However, under certain conditions this mode dominated the collected radiation power. For efficient excitation of the structure waves we begin by focusing the collection system on the longitudinal center of the grating and then we adjust the electron beam for maximum radiation power. This roughly corresponds to the situation where the beam is focused at the grating center and the Rayleigh range is approximately half the grating length. The simulated electron beam waist at the grating region is shown in Figure 6.20. The electron-beam current used in these experiments ranges from $\sim$ 5 - 15 mA. The high power density of the beam prevents the use of many traditional techniques for measuring the beam profile, and we are forced to use the THz signal as our primary diagnostic. This makes tuning the device a challenge in that maximum THz during the alignment procedure does not necessarily indicate the optimum beam condition for efficient excitation of the evanescent mode.

It was noticed early in the experiments that the spectral content of the detected radiation changed depending on the transverse position of the electron beam in the grating channel.

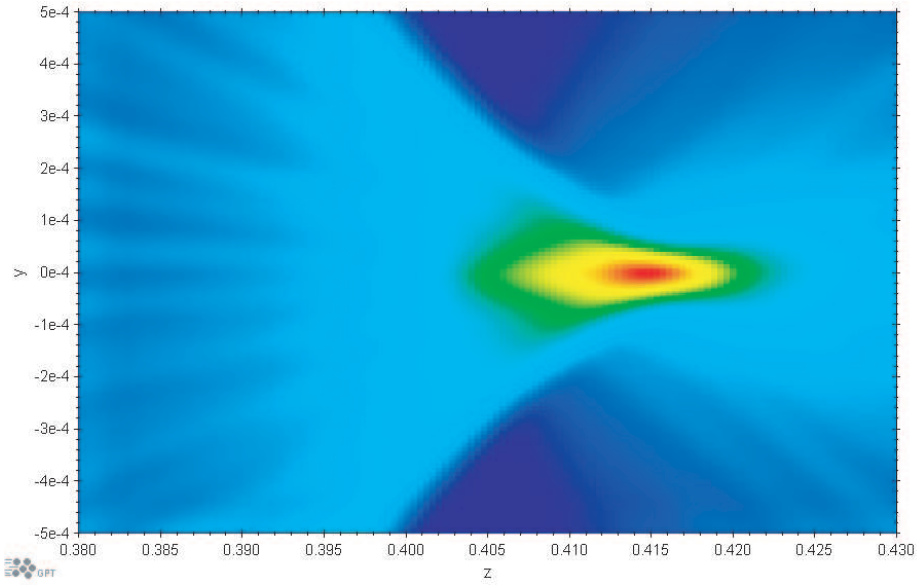

Figure 6.20: Beam waist at the Vermont Photonics SPFEL grating region as simulated in POISSON/GPT. Dimensions are given in meters.

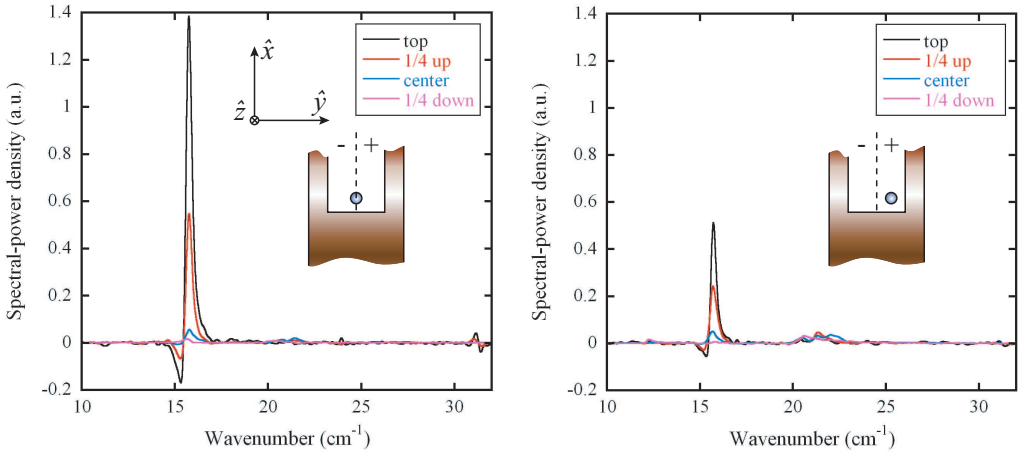

Figure 6.21: Spectra taken as a function of longitudinal mirror position when the electron beam is in the transverse center of the grating (left) and approximately 100 μm right of center (right).

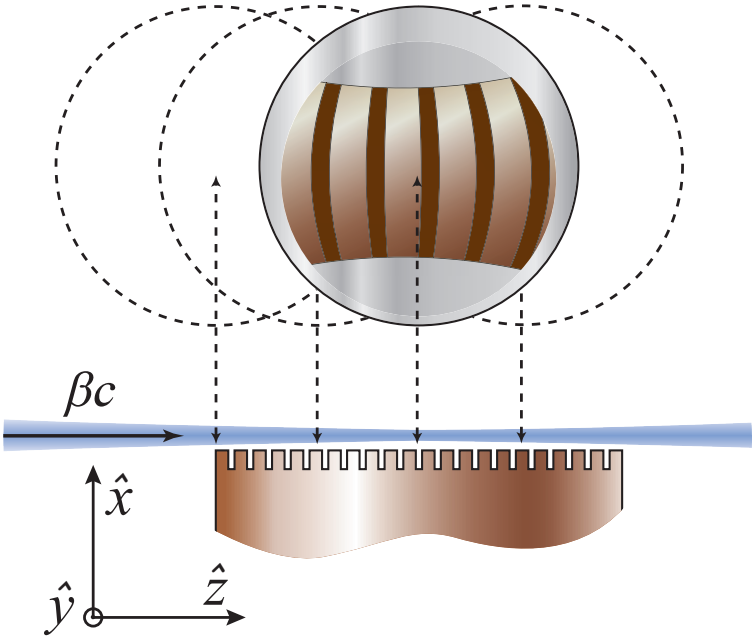

Figure 6.22: Mirror scan procedure for the data in Figures 6.24, 6.25, and 6.26.

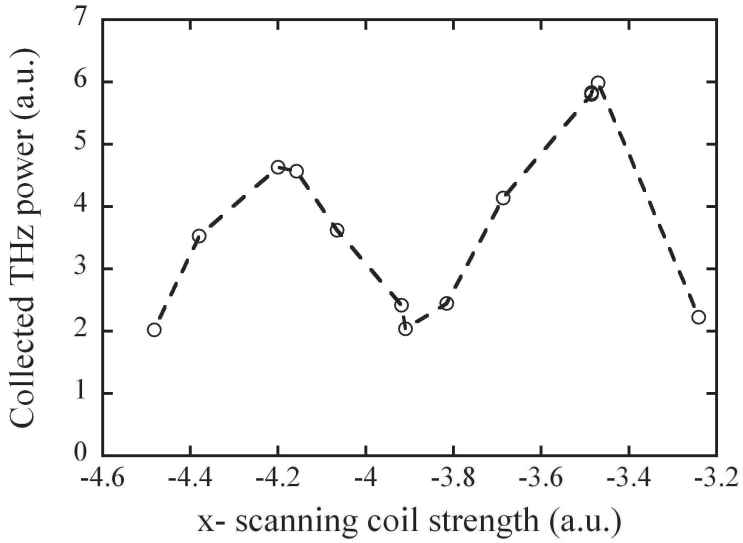

Figure 6.23: An example of the collected total power maxima observed when scanning the electron beam in the transverse dimension. While many different profiles were observed, this was the most common.

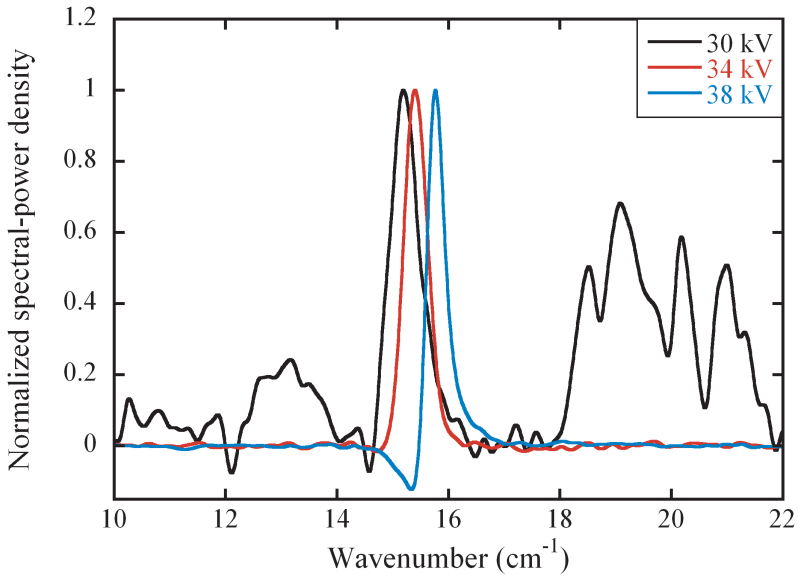

Figure 6.24: Spectra taken from the upstream end of the grating; The largest feature of each spectrum is normalized to 1 for comparison. The $r = 0$ mode, $\sim 13\ \mathrm{cm}^{-1}$, is only observed at 30 kV, possibly due to lower Ohmic losses at larger β_g or grating damage effects.

Consider the spectra in Figure 6.21, which were obtained using the procedure shown in Figure 6.22. In general, evanescent waves of the grating were driven more efficiently when the electron beam was centered (Figure 6.21 left), while SPR was enhanced for an off-center beam (Figure 6.21 right). It is not clear whether this is due to preferential excitation of different radiation modes or variations in the collection efficiency with beam position. Also, for a fixed mirror position, transverse scanning of the electron beam revealed two maxima in the detected total power. Figure 6.23 provides an example of this observation.

These maxima were typically equally spaced from a central minimum that is thought to correspond to the grating's transverse center. The relative intensity of these two peaks varied depending on the beam conditions. Based on a calibration of the (x, y) scanning coils, the separation of the two peaks was on the order of 200 μm when the mirror was at the longitudinal grating center. This profile was less symmetric for some mirror positions and beam conditions and sometimes included multiple shoulders without a central minimum. However, as the mirror was moved toward the upstream grating end, this transverse profile

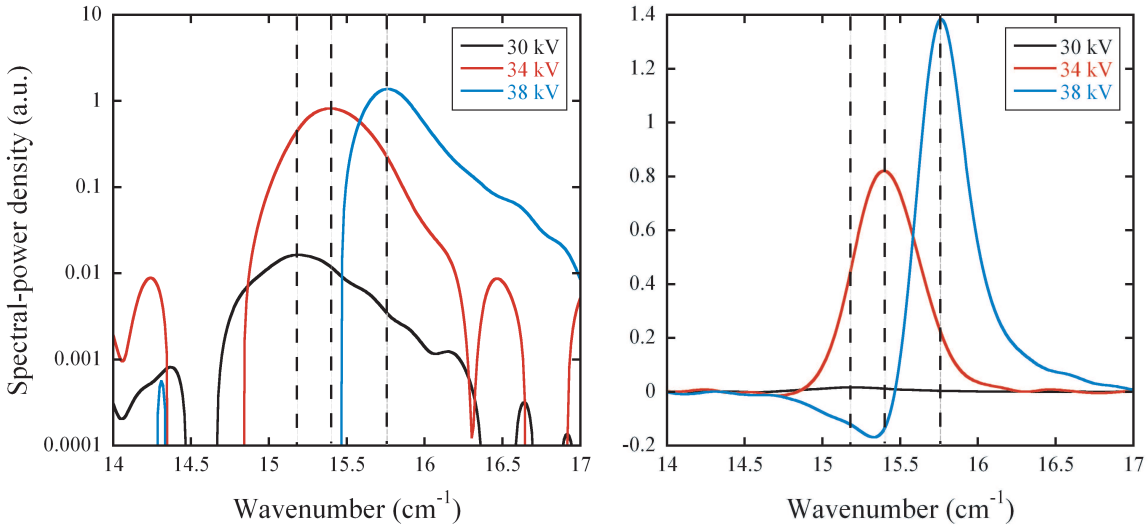

Figure 6.25: THz emission spectrum (log and linear) for different electron beam energies. The $r = 1$ evanescent mode is dominant, two orders of magnitude larger than the first-order SPR (at $\sim 20\ \mathrm{cm}^{-1}$, not shown).

transitioned into a single peak and the collected power was dominated by the scattered $s = 1$ structure wave ($\sim 16\ \mathrm{cm}^{-1}$). The origin of these transverse distributions is not fully understood.

The scattered $s = 1$ mode was observed for three different voltages, 30, 34, and 38 kV, so that the shift of the synchronous point could be measured. For the data in Figures 6.24 and 6.25, the electron beam was optimized using the procedure detailed above. In Figure 6.24 the spectra are normalized to one so that the relative distribution of their spectral power may be easily observed. All other spectra are normalized in the following manner: The bolometer signal at zero-path difference (ZPD) for the interferometer is proportional to the total power. We divide this maximum signal by the integral of the spectrum and multiply by the original spectrum. This normalization ensures that the spectra may be accurately compared to one another. A comparison between these measurements and the wavelengths predicted by the confined-mode theory is given in Figure 6.26. For 30 kV operation we observe the normal Smith-Purcell radiation, a weak $s = 0$ mode signal, and a stronger $s = 1$ peak. When the beam energy is increased to 34 kV the fundamental

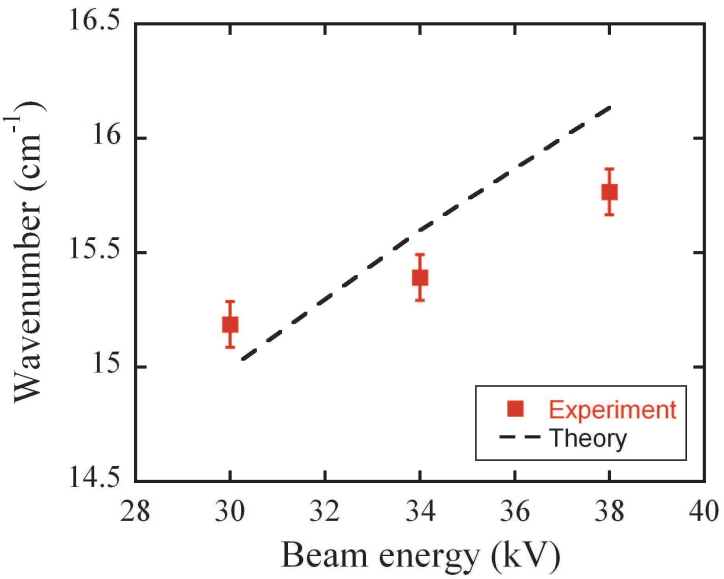

Figure 6.26: Comparison of experiment and theory for the wavenumber of the $r = 1$ evanescent mode. The error bars represent the spectrometer resolution

evanescent mode and the SPR largely vanish while the $s = 1$ signal becomes significantly stronger. At 38 kV the $s = 1$ mode grows dramatically and is the only detectable feature in the spectrum. Currently, the disappearance of the $s = 0$ and the dominance of the $s = 1$ mode is not understood. However, one possible explanation is that the Ohmic losses for the $s = 0$ mode are more severe; due to its very low group velocity this mode transports energy upstream very slowly. While this explains the extinction of mode with increasing voltage, it does not explain previous results in which the $s = 0$ mode was dominant at the grating end and the $s = 1$ mode was completely unexcited. Another possibility is that the fundamental mode is more sensitive to grating damage than the higher order modes. The first 25% of the grating teeth and sidewalls can experience significant damage during the tuning process from exposure to the electron beam. Typically larger $s = 0$ signal was observed with a pristine grating, but this signal tended to diminish over several hours of operation.

Another primary objective of these experiments was to investigate the suspected presence of a GHz instability in the electron beam. Previous experiments at Dartmouth and

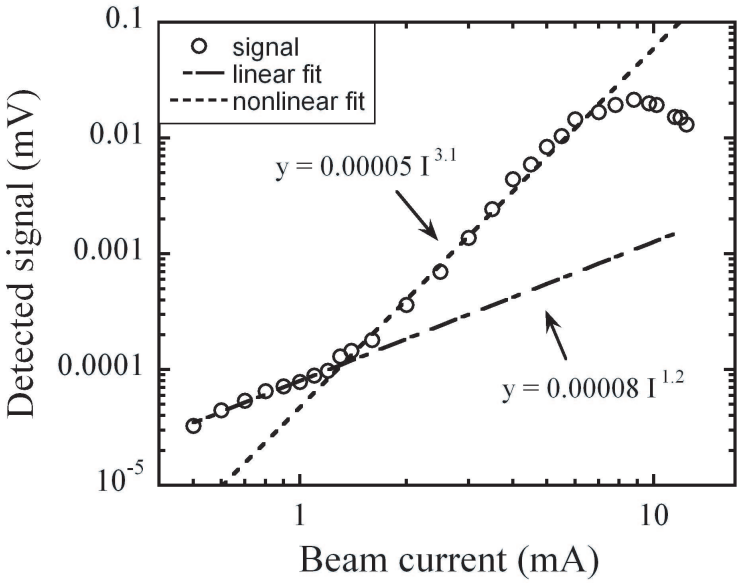

Figure 6.27: Typical example of the linear and non-linear emission regimes in the Vermont Photonics device.

Vermont Photonics exhibited a nonlinear dependence of the output power on the electron beam current. An example of this nonlinearity from the Vermont Photonics device is shown in Figure 6.27. Initially, this nonlinearity was thought to result from the onset of superradiance. However, superradiant emission is accompanied by modification of the angular power spectrum as detailed in section VI.1. No such modification has been observed in either device. Furthermore, nonlinear emission is always observed irrespective of the grating geometry, and the beam current threshold for onset of nonlinear emission seems relatively insensitive to said geometry. These same effects were observed for Cerenkov devices at Dartmouth [77] and the device properties were largely insensitive to the dielectric properties. Nonlinearity in the emitted SPR must be the result of a modulated electron beam density. This modulation would have been easily observed if it occured at a frequency in the THz region. This suggests that the modulation frequency lies below the frequency resolution of the spectrometers that were used, i.e. $\leq\sim 5\mathrm{GHz}$. Alternatively, if the modulation is unstable and fluctuates in frequency, then its spectral signature could be washed out during signal acquisition.

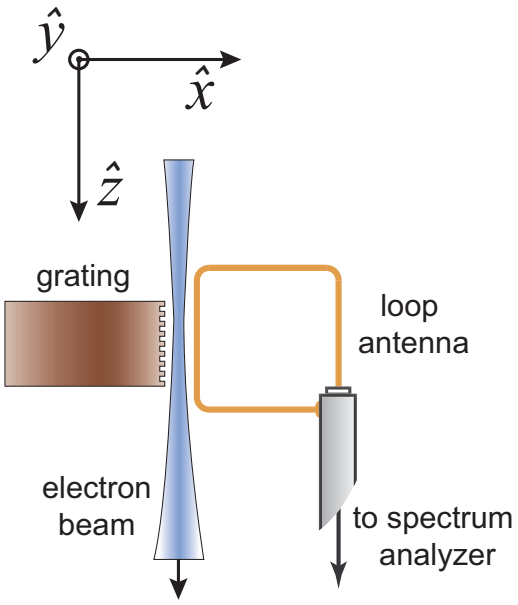

Figure 6.28: Experimental arrangement for measurement of GHz electron beam instabilities.

To produce the observed nonlinear emission, the beam oscillation must persist until it reaches the grating region. A simple loop antenna, designed for $\sim$ 2 GHz, was used in a first attempt at searching for this signal. The system was arranged as seen in Figure 6.28. The grating was left in place so that the beam conditions required for nonlinear emission could be verified while searching for the GHz instability. The initial search failed to detect any GHz signals, however, further experiments are being planned using other antenna and measurement techniques. Additionally, simulations of the electron gun are being considered to estimate the expected frequency of any supported cathode oscillations.

VI.5 **Design of a DFEA Driven Confined-Mode SPFEL**

The high current density of DFEAs and the ability to pulse their emission at microsecond time scales makes the development of a simple SPFEL possible. Until now, attempts to construct SPFELs have been based on modified electron microscopes or similar electron optical columns. These devices are typically large and thus far have produced tightly focused electron beams of no more than 20 mA. Consider the DFEA based SPFEL

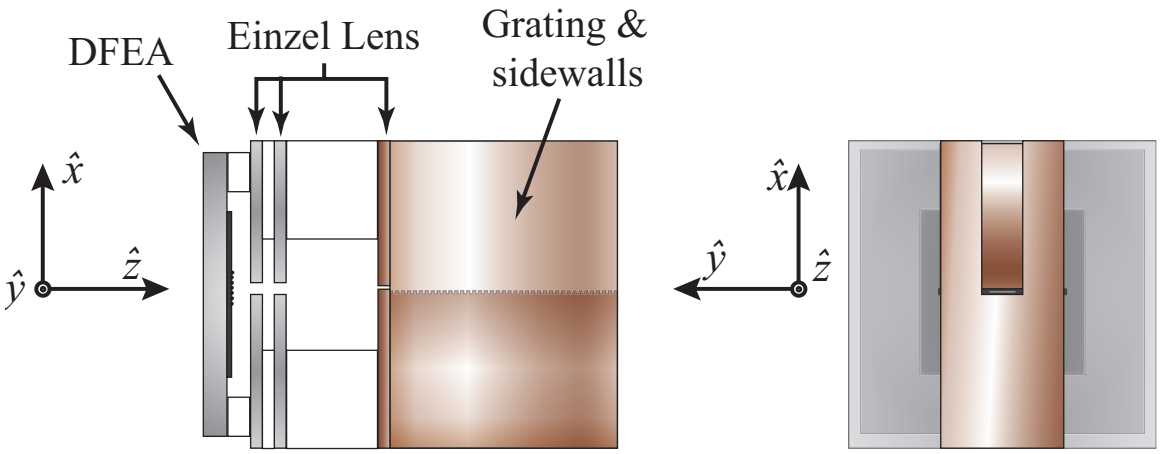

Figure 6.29: Experimental configuration for a DFEA-SPFEL. The total length of the system is $\sim$ 2 cm.

configuration pictured in Figure 6.29. A large area DFEA ($\sim 3 \times 1$ mm) is integrated with a simple Einzel lens that uses an aperture plate on the grating face as its third electrode. The dimensions of the lens electrodes from left to right are 200 μm $\times$ 2 mm, 400 μm $\times$ 2 mm, and 100 μm $\times$ 1 mm. The grating has sidewalls separated by 1 mm. The macroscopic cathode area greatly simplifies alignment by flooding a large area on the anode plate with current. However, this relaxation of alignment constraints comes with the requirement of pulsing the emission on microsecond time scales. Heating calculations with a copper anode have demonstrated $\sim$ 500 °C temperature rise from $\sim$ 5 μs pulses at current densities of $\sim$ 250 A/cm^2 [78]. The thermal relaxation of the system occurs on roughly millisecond time scales. Therefore, the system may be pulsed at frequencies in the hundreds of Hertz range with duty factors of $\sim$ 0.05 % - 0.5 %.

The parameters of the grating are set in part by the need for a practical beam energy. The beam energy is chosen to be 10 kV for the purposes of the design presented here. The primary requirements on the grating geometry are that its fundamental evanescent mode has a low group velocity at the interaction point (so that the gain is large), and that the scale height of that mode is a comfortable size in the context of the electron optical system. A suitable set of grating parameters is given in Table 6.4. The dispersion curves for the first

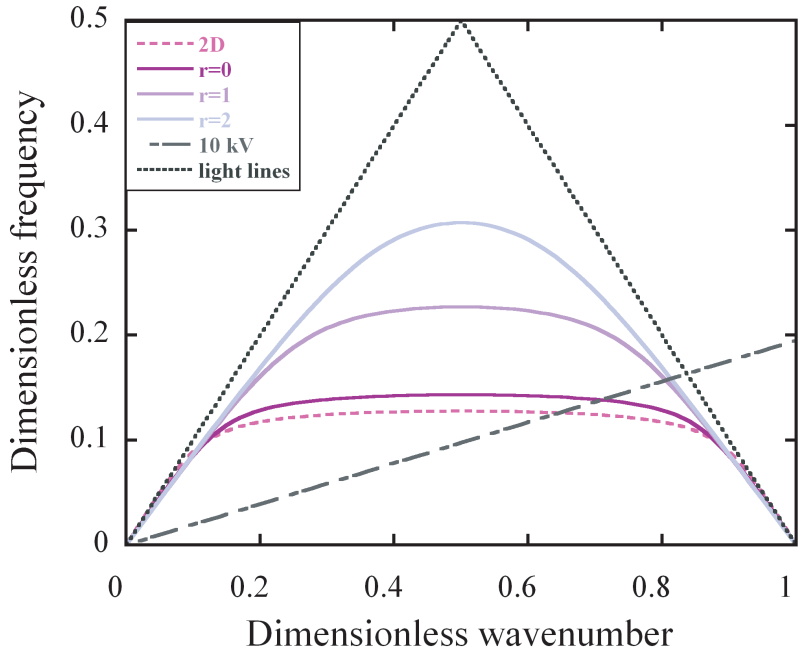

Figure 6.30: Dispersion curves for the first three transverse orders of the evanescent wave. Light lines and a 10 kV electron beamline are also displayed.

three transverse orders of the evanescent wave are plotted in Figure 6.30 along with a 10 kV electron beamline. This grating has a free-space wavelength for the $s = 0$ evanescent wave of $\lambda_{00} = 1.084$ mm, and the first-order Smith-Purcell band is $619\mu\text{m} \leq \lambda_{SP} \leq 919\ \mu\text{m}$. The group velocity at the interaction point is $\beta_g = -0.061c$ and the scale height of the $s = 0$ mode is $1/\alpha_0 = 34\ \mu\text{m}$.

Table 6.4: Parameters of the grating used in designing the DFEA-SPFEL

Grating period	150 μm
Groove width	50 μm
Groove depth	260 μm
Grating length	1 cm
Grating width	1 mm

The electron optical system has been simulated in SIMION 7.0 for determination of the optimum focusing parameters and the approximate beam envelope over the grating. A cutaway view of the device with an electron beam is shown in Figure 6.31. The optimum focal strength for the device was determined by the following procedure: We define an

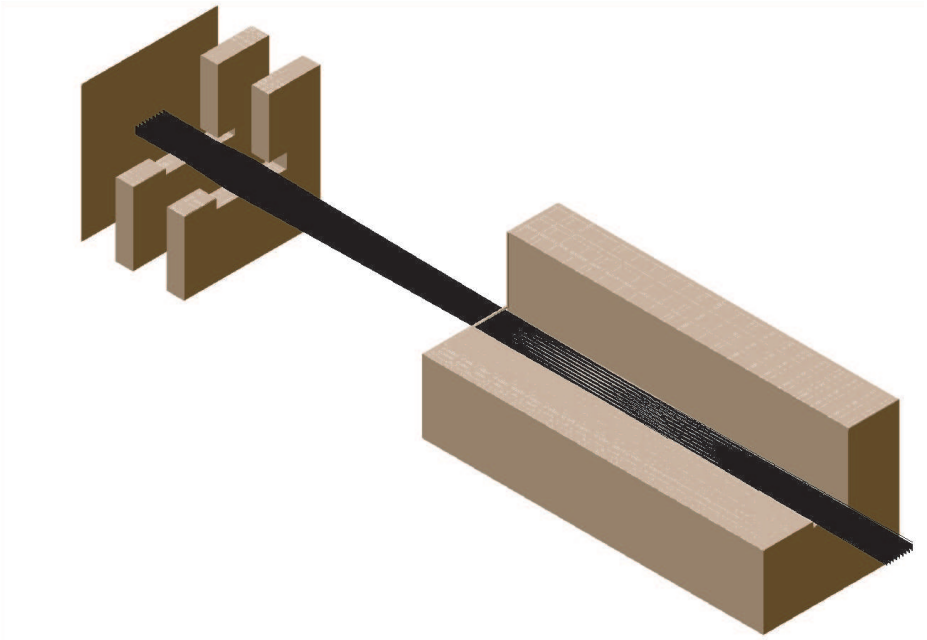

Figure 6.31: Cutaway view of the simulated DFEA driven SPFEL geometry with an electron beam.

effective interaction strength for an electron passing over the grating given by

$$\eta\left(z\right) = e^{x(z)\alpha_0}, \tag{6.119}$$

where $x\left(z\right)$ is the height of the electron above the grating surface as a function of the longitudinal coordinate z, and α_0 is the scale height of the $s = 0$ evanescent wave. The parameter η represents the exponentially decaying interaction of the evanescent wave with the electron as the electron's height above the grating is increased. This parameter is summed over the entire ensemble at a given z position while scanning the focusing bias. This determines the longitudinal profile of the effective strength of the beam-wave interaction as a function of the focusing potential. The results of these scans are shown in Figure 6.32 The optimum focusing strength for this arrangement is determined to be $V_f = 0.58V_{beam} = 5850$ V. The initial electron beam has x and y dimensions of 0.2 mm and 1 mm respectively. Under these conditions $\sim$ 70 % of the electron beam passes the grating aperture and $\sim$ 65 % reaches the grating exit. The effective aperture is defined by

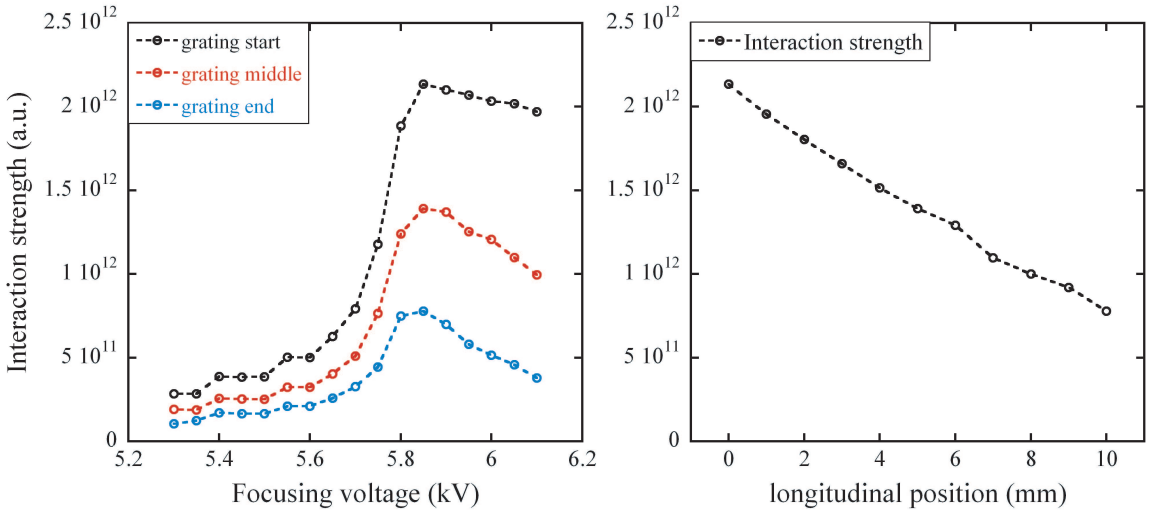

Figure 6.32: Determination of the optimal focusing bias using an interaction-strength weighting parameter for each electron. The plot to the right presents the longitudinal profile of the effective interaction strength for optimum focusing, $V_f = 5.85$ V.

the first lens electrode for the x dimension and by the grating aperture for the y dimension. A side view of the beam's propagation through the device is shown in Figure 6.33. The rms beam envelope was calculated for optimum focusing and is shown in Figure 6.34. The beam centroid drifts further away from the grating surface near the grating end due to intercept losses of aberrated trajectories. Now the simulated beam envelope can be used in calculating the start current and growth rate for the SPFEL interaction. We approximate the actual beam envelope as a uniform density beam that fills the region $x_c - \sqrt{3}\sigma_{bottom} \leq x \leq x_c + \sqrt{3}\sigma_{top}$, where x_c is the average position of the beam centroid, and σ_{bottom} and σ_{top} are the average values of the rms beam radius above and below the centroid. All positions are measured relative to the grating's top surface. Fine-pitch DFEAs are capable of current densities in excess of 250 A/cm^2 in 10 μs pulses. This corresponds to currents through the grating of up to 350 mA. Additional simulation will be required to determine the effects of space charge on the propagation of such a beam. The resulting beam parameters of the simulations are presented in Table 6.5

When the beam parameters of Table 6.5 are used in conjunction with the grating of

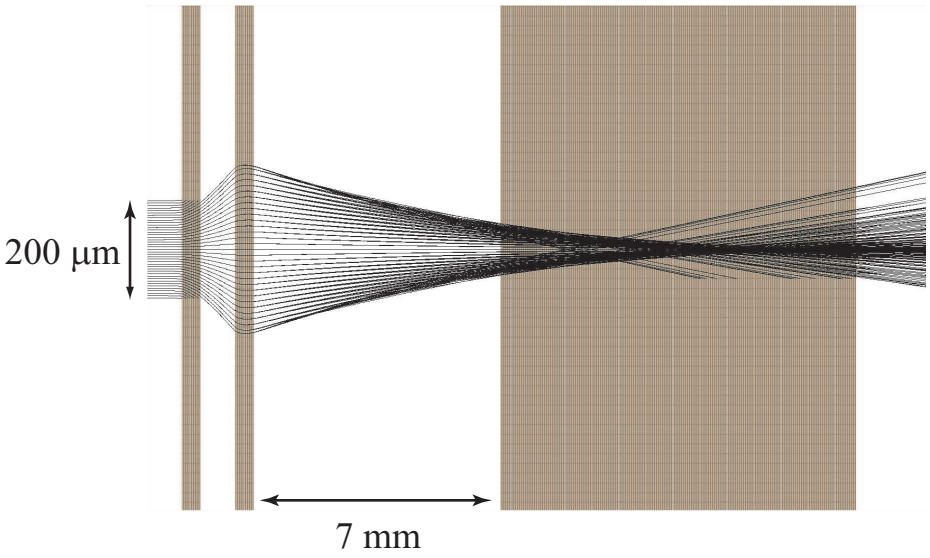

Figure 6.33: Side view of the electron beam's propagation throught the DFEA-SPFEL.

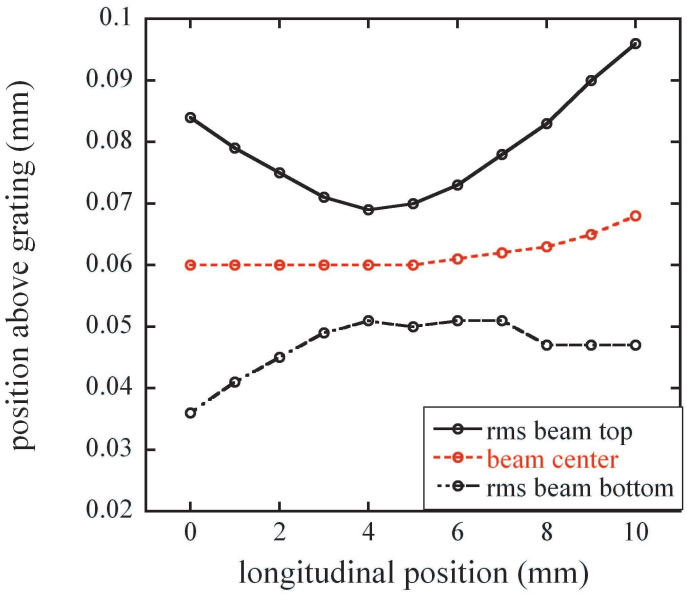

Figure 6.34: Rms beam envelope for the electron beam at optimum focusing conditions.

Table 6.5: Electron beam parameters determined by simulation of the DFEA-SPFEL electron optical system.

Beam width	$1\ \mathrm{mm}$
Beam bottom	$34\ \mu\mathrm{m}$
Beam top	$86\ \mu\mathrm{m}$
Beam current	$0 \leq I_{beam} \leq 350\ \mathrm{mA}$
Beam voltage	$10\ \mathrm{kV}$

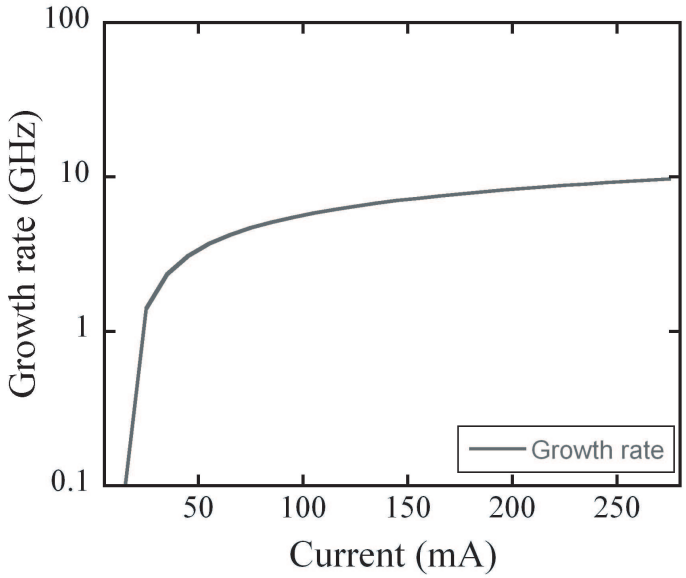

Figure 6.35: Calculated growth rate for the $s = 0$ evanescent wave as a function of electron beam current.

Table 6.4, the start current for oscillation on the $s = 0$ backward wave is $I_{start} = 11.4$ mA. This current level is easily achieved with the current densities that have already been demonstrated for sparse, 20-μm pitch arrays. The growth rate for the evanescent mode as a function of current is shown in Figure 6.35. The growth rate is on the order of several GHz, meaning that the beam-wave resonance should saturate in nanoseconds. For these grating and beam parameters, the dominant superradiant-SP emission should occur where the third harmonic of the evanescent wave coincides with the second order SPR: $\theta = 72^{\circ}$ and $\lambda_{SP} = 361\ \mu\mathrm{m}$ (0.831 THz).

CHAPTER VII

QUANTUM-DEGENERATE ELECTRON BEAMS AND A PROSPECTIVE SOURCE

VII.1 Introduction

In recent years our development of high-brightness electron-beam sources has led us to consider the ultimate limit of brightness, the so-called quantum-degenerate limit. This limit represents the maximum phase-space density that can be achieved with a beam of fermions, and is a direct consequence of the anti-symmetric nature of their wavefunctions. The uncertainty principle sets a fundamental unit of volume for 6-dimensional phase space of h^3. Each h^3 of phase space contains a single spin pair of electrons for a degenerate beam. The level of quantum degeneracy in a beam can be written in terms of the 6-dimensional brightness (6-dimensional phase-space density as

$$\delta = \frac{h^3 B_{6D}}{2} = \frac{h^3 d^6 N_e}{2dx dp_x dy dp_y dE dt} \tag{7.1}$$

where N_e is the number of electrons, x and y are the transverse spatial coordinates, p_x and p_y are the transverse momenta, E is the longitudinal energy, and t is the time coordinate. In terms of this degeneracy parameter, the normalized transverse brightness is given by

$$B_N = \frac{m^2 c^2 d^4 I}{dx dy dp_x dp_y} = 2\frac{m^2 c^2 q^2 \Delta V}{h^3}\delta \tag{7.2}$$

where ΔV in the electron-energy spread in eV. The quantum-degenerate limit, $\delta = 1$, is then calculated for a field emitter ($\Delta V \approx 0.3$ eV) to be $B_N \approx 3 \times 10^{18}$ A/m^2-str. Figure 1.1 (Chapter 1) displays this brightness limit and the estimated brightness from a range of different cathode technologies. Thus far, specialized field emitters are the only sources capable of reaching this limit.

VII.2 **Measurement of Quantum Degeneracy**

Simple estimates of the quantum degeneracy in an electron beam require knowledge of the transverse brightness and the electron-energy spread. The transverse brightness is typically not measured directly but is rather estimated based on the measurement of other beam parameters. One such technique, described by [9], involves the use of low-energy point-projection microscopy for determining the transverse coherence length of the electron source. The electron waves diffract around a hard edge and interfere at a downstream detector producing Fresnel fringes. The number of observed fringes depends on the emitter surface area over which the electrons are emitted coherently, A_c. The coherence time for the electrons follows from the uncertainty principle and is approximately $t_c = h/\Delta E$. The degeneracy is roughly the number of electrons that pass through the coherence area A_c during the coherence time t_c, i.e. $\delta = (J/q)\, A_c t_c$, where J is the current density.

A more sophisticated and definitive method of measuring degeneracy is the Hanbury Brown-Twiss coincidence measurement. This technique is also known as intensity interferometry, and it provides a direct measure of quantum degeneracy. A diagram of such a measurement is shown in Figure 7.1. When a beam has insignificant levels of degeneracy, the arrival of electrons at the detector plane is stochastic and Poissonian statistics accurately describe the system. However, as the degeneracy is increased, temporal antibunching begins to develop in the beam. This antibunching can be detected as anticorrelations in electron arrivals at the two detectors, which are placed within the beam's magnified transverse-coherence area. A measurement of this type has been performed on the beam from a tungsten field emitter [12]. Weak antibunching was successfully detected and that signature was only present when both detectors were coherently illuminated by the beam. The corresponding quantum degeneracy in this case was $\delta \approx 1.6 \times 10^{-4}$.

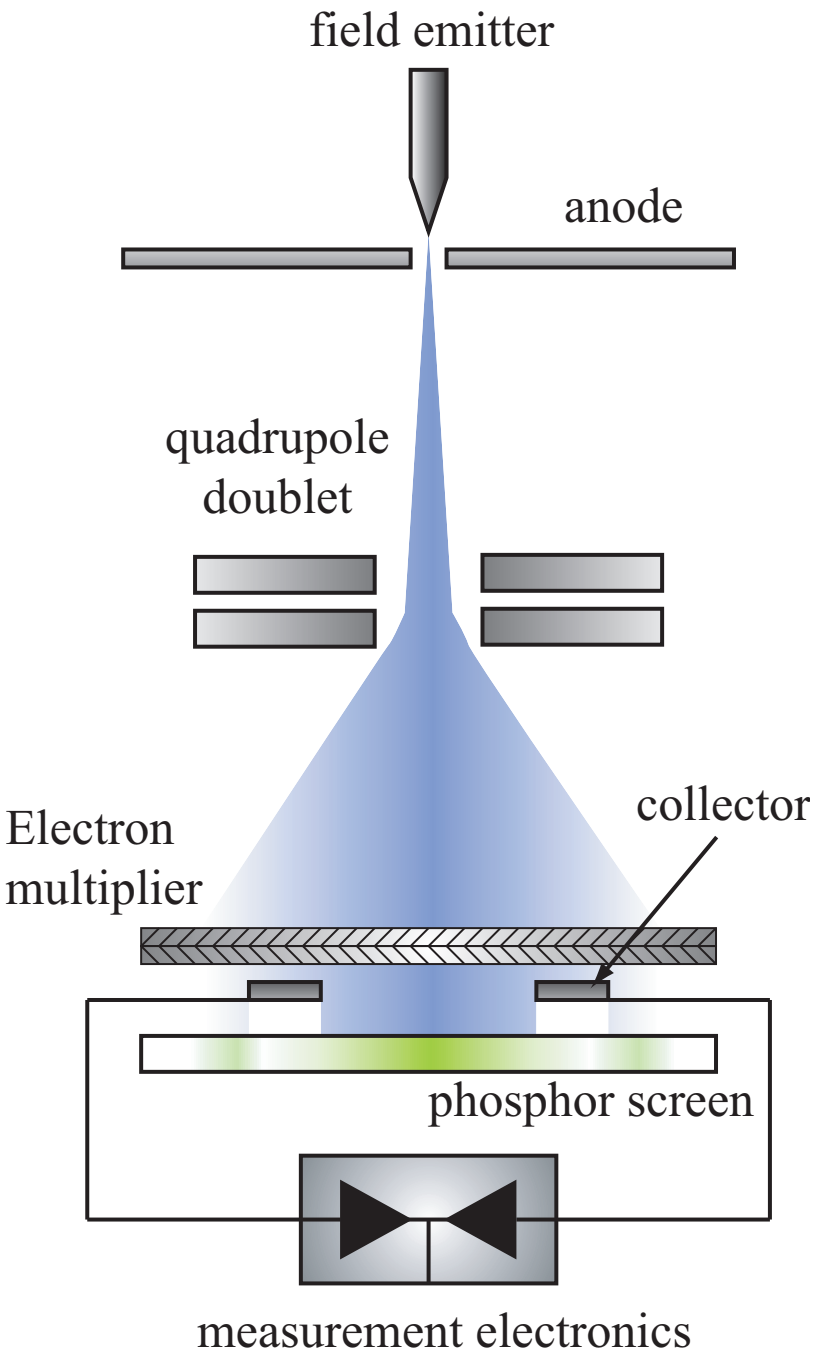

Figure 7.1: Experimental arrangement for measuring electron-beam antibunching. The same arrangement was used by Kiesel et al to measure the degeneracy of a beam from a tungsten field emitter.

VII.3 **A Carbon Nano-Tube Based Quantum-Degenerate Electron Beam Source**

We have recently begun a program to develop high-brightness electron sources capable of reaching the quantum-degenerate limit. From a practical standpoint, it is important that these sources operate with very high local current densities in a stable manner for extended periods of time. Covalently bonded carbon structures such as carbon nanotubes and diamond microtips have excellent high-current-emission stability due to their stable structure and chemically inert nature. In contrast, for tungsten emitters we have observed significant emission fluctuations during field-emission microscopy studies. Additionally, metals are less chemically stable and are more prone to back bombardment damage and catastrophic failure modes such as explosive evaporation. Carbon nanotubes and diamond are known to have excellent thermal conductivity which helps mitigate such thermally driven failure modes.

It has been known for many decades that the presence of adsorbed molecules or atoms on the surface of a field emitter can produce order-of-magnitude enhancements of the local emission current. Typically, the adsorbed species are residual gases from the vacuum system. Depending on the operating conditions, these adsorbates are typically stable for many seconds. We are beginning experimental and theoretical efforts to determine which types of adsorbates provide the greatest emission and stability enhancements. In recent months we have observed beams of extraordinary brightness from adsorbed gas molecules on individual MWCNT. Collaborators at Leiden University in the Netherlands mount these individual MWCNTs on a tungsten-needle support for handling and mechanical stability [79]. An example of the completed cathode is shown in Figure 7.2. A simple diagram of the field-emission microscope used to examine these cathodes is presented in Figure 7.3. Figure 7.4 shows a field-emission micrograph of a MWCNT whose surface was cleaned with a combination of laser irradiation and high-current operation.

The underlying covalent structure of the closed-cap nanotube is clearly seen in the form of bright pentagonal rings. Figure 7.4 also demonstrates a transient adsorbate event

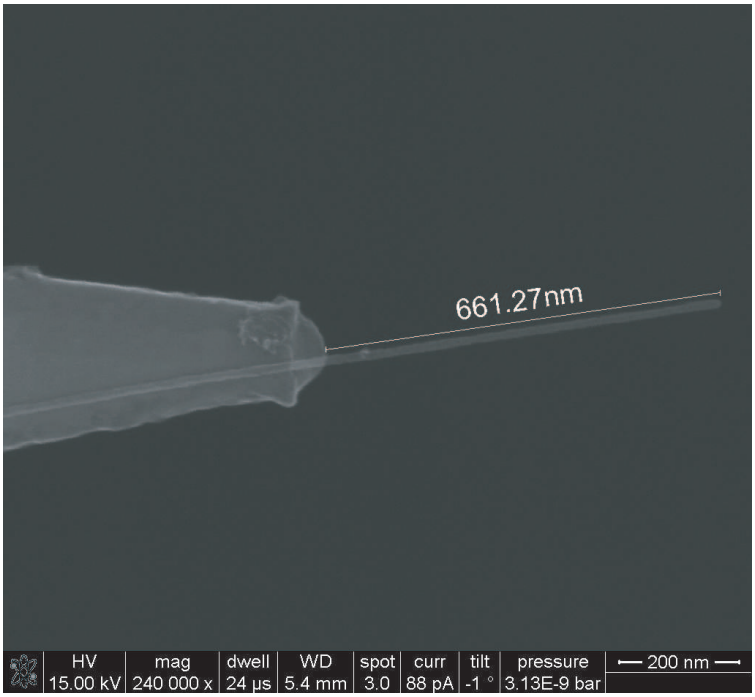

Figure 7.2: An individual MWCNT mounted on a tungsten needle.

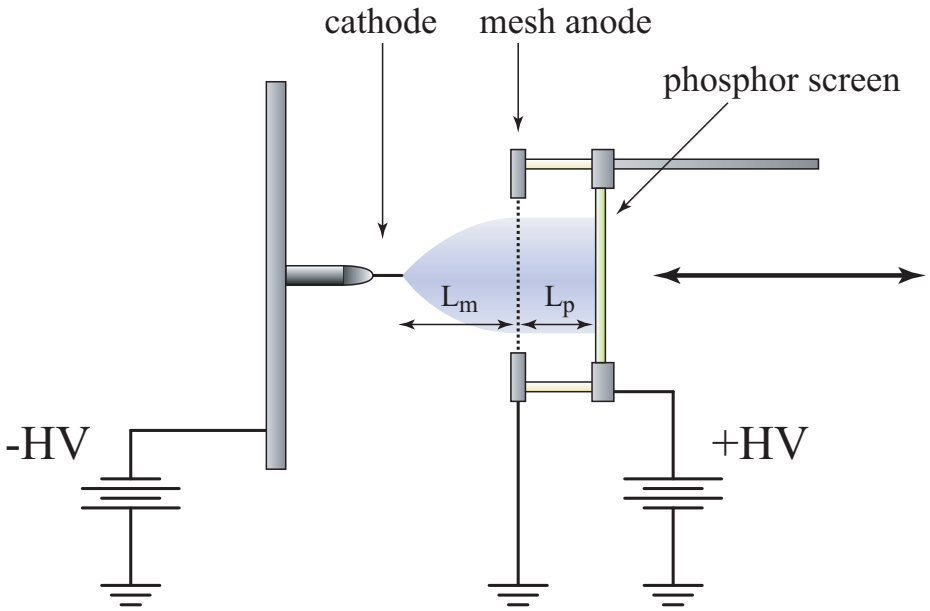

Figure 7.3: Diagram of the FEM apparatus used for these experiments. The addition of a mesh anode enables the application of a booster field between the phosphor and mesh. This allows observation of the emission pattern at any anode-cathode spacing/potential combination.

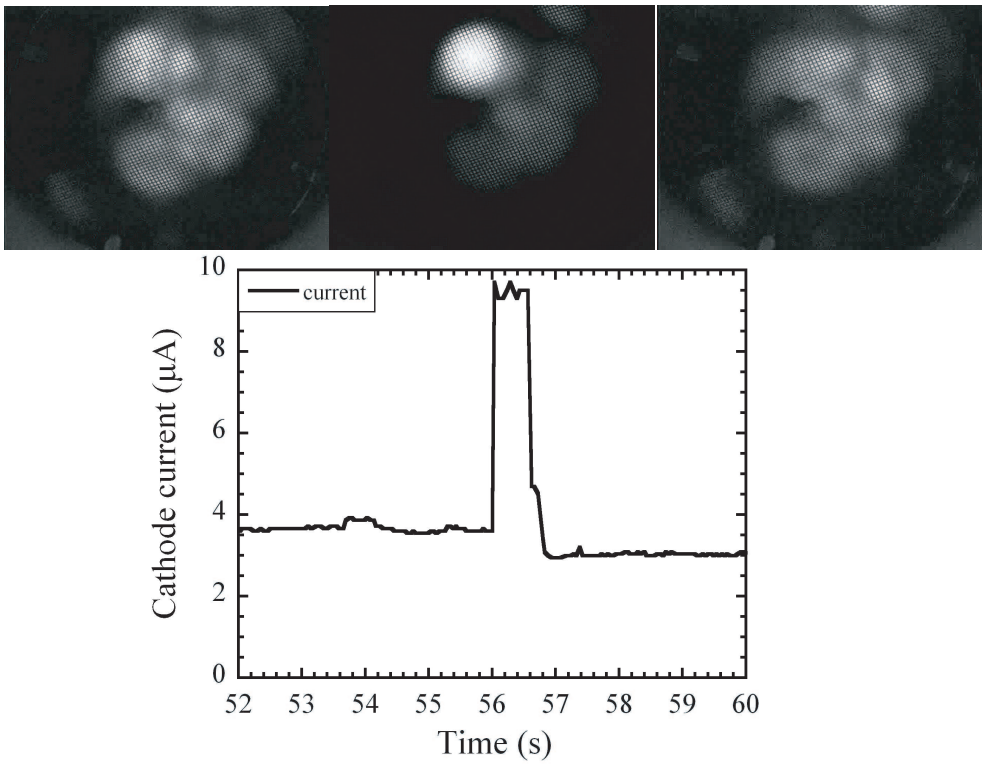

Figure 7.4: In these FEM micrographs, the underlying symmetry of the clean MWCNT is clearly seen in the form of bright pentagonal rings. Additionally a transient adsorbate event was observed which corresponded to a 6-μA increase in the emission current.

that resulted in a current enhancement of 6 μA. The phosphor image of this event and the operational parameters of the experiment can be used to estimate the brightness and quantum degeneracy of the resulting beamlet. For a symmetric beam the normalized transverse brightness is given by

$$B_N = m^2c^2\frac{d^4I}{dx^2dp_x^2}. \tag{7.3}$$

If we assume that the transverse momentum is constant, then the transverse-momentum spread can be estimated in terms of the observed spot size by

$$\Delta p_x = \frac{dm}{L_m\sqrt{\frac{m}{2qV_m}} + L_p\sqrt{\frac{m}{2qV_p}}} \tag{7.4}$$

where d is the measured spot diameter, L_m and L_p are the mesh-emitter and mesh-phosphor distances respectively, and V_m and V_p are the applied voltages at the mesh and phosphor relative to the cathode bias. The approximate parameters under which the data in Figure 7.4 were acquired are given in Table 7.1. In terms of these parameters the brightness is given

Table 7.1: Experimental parameters from Figure 7.4

L_m	1 cm
L_p	1 cm
V_m	360 V
V_m	1360 V
d	5 mm

by

$$B_N = \frac{c^2 I}{\Delta x^2} \frac{m}{2qd^2} \left(\frac{L_m}{\sqrt{V_m}} + \frac{L_p}{\sqrt{V_p}} \right)^2 , \tag{7.5}$$

where Δx is the emitter size. If the beamlet originates from a single adsorbed atom or small molecule, then $\Delta x \approx 10^{-10}$ m. For a beamlet current of 6 μA the brightness is estimated to be $B_N \approx 4 \times 10^{18}$ A/m^2-str. This estimate suggests that the observed beam is nearly quantum-degenerate. As seen in Figure 7.4, the effective lifetime of this source was less than one second. To make a long lifetime source, adsorbates with higher surface binding energies must be found.

VII.4 **Continuing Experimental and Theoretical Efforts**

There are two proposed methods for preferential deposition of adsorbates on the emitter tips: thermal evaporation and pulsed-laser ablation. Laser ablation has the advantage of being time gated. This helps to discriminate between residual gas and atoms emitted from the target during ablation. The atoms to be tested include cesium, strontium, yttrium, barium, magnesium, and gold. The energy analyzer discussed in Chapter 5 will be integrated with the system and will be used to search for signs of degeneracy such as anomalous spectral broadening at high currents. Deflection plates near the cathode and a phosphor on the front of the analyzer will facilitate spectral analysis of the emitted

beams from the clean CNT (pentagons) and from the adsorbed species independently. The measured energy distributions can be compared to the emitted distributions calculated by advanced density-functional theory techniques at Vanderbilt [80]. These calculations might be used to guide the experimental efforts by quickly estimating current enhancement, stability, lifetime and emitted energy spread for various atoms and molecules of interest. Once a mastery of the techniques for producing and preserving these bright sources has been developed, intensity interferometry measurements will be performed to measure the quantum degeneracy of these beams. Additionally, these same investigations and techniques will be applied to gated diamond emitters once they reach operational status.

CHAPTER VIII

CONCLUSIONS

This primary purpose of this thesis has been to discuss the recent developments of diamond field-emitter arrays and their integration with electron-beam-driven radiation sources. These sources include, but are not limited to, conventional free-electron lasers and compact FEL paradigms such as the Smith-Purcell or Cerenkov free-electron laser. Important questions exist related to the operation of DFEAs in the various injector systems used to drive these lasers. DFEAs are slated for near term integration into several different injector types at various institutions. In the work presented here, important emission properties of DFEAs such as spatial uniformity, transverse emittance, and emitted energy spread have been reported. Additionally, the 3-dimensional theory of the Smith-Purcell free-electron laser has been developed and experimental support for this theory has been reported. Also, preliminary results from a proposed quantum-degenerate electron-beam source have been given. In the folowing pages, the motivation, results, and conclusions for each chapter of this thesis are presented.

Chapter 1: Introduction The next major advancements in electron-beam-driven radiation sources are closely tied to the development of cathode and electron injector technologies. X-ray FEL devices depend on the capability to reliably produce high bunch charges while maintaining very high beam brightness. The demonstration of 100-kW and 1-MW class high-average-power FELs relies on the development of high-average-current injectors. Such an injector using present photocathode technology is complicated by the need for complex and unstable high-power cathode-drive-laser systems and the delicate nature of high-efficiency photocathodes. Compact THz FELs require the delivery of high current densities over large areas while maintaining a reasonably low emittance. DFEAs are in a unique position to provide cathode solutions for many of these important

problems. Of particular interest to this author is the use of DFEAs in the aforementioned compact THz FELs. The theory and design of such a device was presented in Chapter 6. Finally, the concept of quantum degeneracy in a free-electron ensemble is discussed. In most beams, the electron density in phase space is too dilute to observe the quantum effects of degeneracy. However, for the ultra-high-brightness beams produced by single-atom-electron sources, the degeneracy becomes significant and its effects may be readily observed. Chapter 7 discussed these concepts in more detail and preliminary results from a proposed degenerate-beam source were presented.

Chapter 2: Diamond Field-Emitter Arrays The development of DFEAs has spanned nearly two decades, however until now their primary application was to concepts such as vacuum microelectronics, high-power switching, and thermal-electric conversion. Through a fruitful collaboration with the diamond microelectronics group in the Vanderbilt University Department of Electrical and Computer Engineering, we have advanced the development of DFEAs as free-electron-beam sources. In this chapter we discussed the inverse-mold-transfer processes by which DFEAs are fabricated. These processes were detailed for both gated and ungated DFEAs as well as for diamond-coated Si devices. Vanderbilt is currently in collaboration with the Naval Postgraduate school to test DFEAs in both HV DC and SCRF injector systems. The DC tests will examine the lifetime and stability of DFEAs under the stress of high-energy ion back bombardment. Operation in a superconducting environment and strategies for proper time gating of the emission will be examined when the SCRF gun is completed.

Chapter 3: Emission Uniformity of DFEAs The discussions of this chapter centered on the fundamental challenge of producing spatially uniform emission from FEAs. Nonuniformity in an ensemble of field emitters is due primarily to the variability of each emitter's surface-contamination state and variations in the underlying morphology and composition from tip to tip. While certain techniques such as thermal annealing and

plasma exposure may be used to normalize the contamination states, normalization of tip morphology in large ensembles of emitters requires a self-limiting conditioning process. This process must discriminate based on a tip's emission current and surface electric field. Such a conditioning technique for DFEAs was discovered, characterized, and optimized in this work. High-current conditioning has successfully produced uniform emission from large numbers of tips while maintaining reasonable turn-on fields. Thus far, per-tip currents of 40 μA have been demonstrated. For high-density arrays (4-μm pitch), this corresponds to a current density of $\sim$ 250 A/cm^2. These tests were performed under conservative conditions and were not designed to drive the cathode to its failure limits. These limits will be tested in coming months with high-current operation at microsecond time scales. So far the primary limitation of DC operation has been back bombardment from sputtered anode material at high current densities. The tests in the DC gun at NPS should help determine the limits of DC operation in the absence of this particular back bombardment. Conditioning tests demonstrated that DFEAs were capable of high current operation in extremely poor environments for prolonged periods of time.

Chapter 4: Emittance and Brightness of DFEAs This chapter discussed the concepts of transverse emittance and transverse beam brightness, and techniques for determining these measures experimentally. These techniques included measurement and fitting of a focused beam envelope as well the standard pepperpot technique which is used to determine transverse-trace-space projections of the electron ensemble. The experimental arrangement for a pepperpot emittance measurement of DFEAs was given. The aperture mask was specially fabricated from an SOI wafer. This mask served as the primary anode in a close-diode arrangement with a 3$\times$24, 20-μm pitch DFEA. The measured divergence of the electron beam corresponds to a normalized transverse emittance of $\sim$ 10 mm·mrad for a uniform beam with transverse dimensions of 1 cm$\times$1 cm. This satisfies the

emittance requirements of IR HAPFELs. The experimental results are closely supported by simulations of the emitted beamlet from a single diamond microtip.

Chapter 5: Energy Spread from DFEAs The emitted energy spectrum from DFEAs can provide insight into the fundamental physics of their electron emission process. A high-resolution retardation energy analyzer was designed, constructed, and tested for the purpose of measuring this emission spectrum. The analyzer was simulated in SIMION and shown to be capable of mV resolution for kV beams. However, nonidealities in the actual analyzer such as mesh granularity and imperfect alignment of components produce an instrumental broadening that decreases the resolution to ~ 0.15 eV. This resolution function was determined by energy analysis of the beam emitted from a LaB_6 thermionic cathode. The resolution function is deconvolved from any measured spectra to mathematically improve the instrument resolution. After these fiducial measurements, the analyzer was used to measure the emitted spectrum from a DFEA. The array parameters were chosen to provide a high probability of current acceptance from a single emitter. Subsequent observations with the analyzer suggest that the accepted current did indeed originate from a single tip. Temporal modulations in the total current and emitted spectrum were observed, and were interpreted as the result of resonant tunneling through adsorbed species on the emitter surface. These fluctuations draw close analogy to those observed with carbon-nanotube field emitters. It is believed that 5-10 % of the emitted spectra contained the spectral signature of a clean emitter surface. This suposed clean spectrum has a FWHM of ~ 0.55 eV, and it was fit with a thermal-field emission model using reasonable parameters.

Chapter 6: The Smith-Purcell Free-Electron Laser: an Application of DFEAs The SPFEL and similar compact FELs have the potential to fill a very important source gap in the electromagnetic spectrum, the so-called THz gap. The development of compact, narrow-band, moderate power THz sources would serve as an important catalyst for new discoveries in material science, medical imaging, remote detection, and biomolecular

dynamics. In this chapter the 3-dimensional theory of small-signal SPFEL operation was developed for an infinitely wide grating. It was found that the evanescent modes of the grating are gain guided by the electron beam, resulting in a gain which depends on $I^{2/5}$ rather than the standard $I^{1/3}$ of 2-dimensional theories. The dilution effects of transverse diffraction in the optical beam lower the gain substantially. This makes lasing exceedingly difficult for the case of a narrow electron beam. One solution is to confine the optical mode in the transverse dimension with conductive grating sidewalls. The theory of this confined-mode SPFEL was developed, and subsequenty applied to collaborative experiments with Vermont Photonics. The first observation of higher-transverse-order evanescent modes was reported, and found to be in excellent agreement with the confined-mode theory. Lasing of an SPFEL on an evanescent mode of the grating has yet to be achieved. Finally, a design for a DFEA driven SPFEL was presented. Propagation of the electron beam through this compact device (~ 1 in^3) was simulated and the resulting beam profile was used to calculate the performance characteristics of the FEL interaction.

Chapter 7: Quantum-Degenerate Electron Beams and a Prospective Source In this chapter the intriguing concept of quantum degeneracy free-electron beam was discussed. The development of reliable and robust quantum-degenerate electron sources would mark an achievement similar to the development of the laser, which produces degenerate ensembles of photons. Widespread access to quantum-degenerate electron beams may open up new frontiers in imaging through techniques such as intensity interferometry and high-speed electron holography. Further applications might include the miniaturization of high-resolution electron microscopes, or advances in quantum computation. Thus far, we have demonstrated electron beams that are near the quantum-degenerate limit of beam brightness using MWCNTs with adsorbed gas molecules. However, these beams are only stable for seconds at a time. We are preparing to selectively deposit a variety of adatoms on the emitter surface in an effort to produce beams with longer operational lifetimes.

These efforts are being paralleled by collaborators performing calculations with advanced density-functional theory techniques. With the successful development of a stable source, we will estimate the degeneracy first through energy spread measurements, noise-spectrum measurements, or point-projection microscopy, and subsequently measure it directly with intensity interferometry.

Future Directions The results of this thesis suggest a number of directions for future work:

1. The electron-emission physics for DFEA emitters with and without adsorbed species should be subject to further experimental and theoretical investigations. These studies may provide insight on how to take advantage of adsorbate effects to improve DFEA emission properties. Such work may also have relevance to adsorbate effects with carbon-nanotube field emitters.

2. Of the various DFEA types, ungated arrays have reached the most mature state. However, the development of gated DFEAs is being actively pursued. The remaining challenges include the elimination of gate leakage and testing of the high-frequency response characteristics for these devices.

3. DFEAs will soon be integrated with various electron injector systems. The capability to properly time gate electron emission from ungated arrays must be established, and the lifetime of DFEAs in such environments must be examined.

4. Demonstration of functional gated and multi-gated devices will facilitate the development of compact, scanning-probe electron microscopes. Such devices focus the electron beam from a single emitter using multiple self-aligned-gate electrodes, and collect the secondary electrons scattered from a nearby sample. The sample may be scanned underneath the stationary beam with high precision piezo-electric

actuators. Additionally, gate electrodes with higher degrees of symmetry may be produced, such as sextupoles, for aberration correction.

5. The compact DFEA-SPFEL discussed in Chapter 6 should be developed. This device should be used to check the validity of the confined-mode SPFEL theory (also presented in Chapter 6). Once the source is functional, investigations in biomolecular dynamics and other fields of interest should be undertaken.

6. Development of carbon nanotube quantum-degenerate-electron-beam sources should continue. The next line of investigation will involve the use of certain adsorbates, such as strontium, gold, or cesium, for increasing the stability and lifetime of the source. Measurements of the emitted energy spread from these adsorbates may give indications of degeneracy, such as anomalous broadening of the spectrum. After these preliminary experiments, coincidence measurements should be performed to observe anti-bunching, thus providing an unmistakable degeneracy signature. Similar experiments may also be performed with gated diamond field emitters once they are operational.

7. Quantum-degenerate-electron-beam sources may find practical application in the fields of high-resolution electron microscopy and high-speed electron holography. Additionally, the intensity interferometry techniques used to measure quantum degeneracy may have application as a new imaging modality. These techniques should be investigated upon successful source development.

REFERENCES

[1] Kenneth J. Button. *Infrared and Millimeter Waves*. Academic, New York, 1979.

[2] V. P. Bolotin et al. Status of the Novosibirsk terahertz FEL. *Nuclear Instruments and Methods in Physics Research A*, **543**(81), 2005.

[3] L. F. DiMauro, J. Arthur, N. Berrah, J. Bozek, J. N. Galayda, and J. Hastings. Progress Report on the LCLS XFEL at SLAC. *Journal of Physics: Conference Series*, **88**(012058), 2007.

[4] E. Garate, P. Cook, R. Layman, and J. Walsh. Cerenkov maser operation at lower-mm wavelengths. *Journal of Applied Physics*, **58**(2), 1985.

[5] J. Urata, M. Goldstein, M. F. Kimmitt, A. Naumov, C. Platt, and J. E. Walsh. Superradiant Smith-Purcell Emission. *Phys. Rev. Lett.*, **80**(3), 1998.

[6] K. L. Jensen, D. W. Feldman, M. Virgo, and P. G. O'Shea. Measurement and analysis of thermal photoemission from a dispenser cathode. *Physical Review Special Topics - Accelerators and Beams*, **6**(083501), 2003.

[7] S. C. Leemann, A. Streun, and A. F. Wrulich. Beam characterization for the field-emitter-array cathode-based low-emittance gun . *Physical Review Special Topics - Accelerators and Beams*, **10**(071302), 2007.

[8] R. Ganter, R. Bakker, C. Gough, S. C. Leemann, M. Paraliev, M. Pedrozzi, F. Le Pimpec, V. Schlott, L. Rivkin, and A. Wrulich. Laser-Photofield Emission from Needle Cathodes for Low-Emittance Electron Beams. *Physical Review Letters*, **100**(064801), 2008.

[9] J. C. H. Spence, W. Qian, and M. P. Silverman. Electron source brightness and degeneracy from Fresnel fringes in field emission point projection microscopy. *Journal of Vacuum Science and Technology A*, **12**(2), 1994.

[10] M. P. Silverman. Distinctive Quantum Features of Electron Intensity Correlation Interferometry. *Nuovo Cimento B*, **97**(200), 1987.

[11] E. Zeitler. Coherence in scanning transmission microscopy. *Scanning Electron Microscopy*, (671-678), 1975.

[12] H. Kiesel, A. Renz, and F. Hasselbach. Observation of Hanbury Brown-Twiss anticorrelations for free electrons. *Nature*, **418**(392), 2002.

[13] C. A. Spindt. A Thin-Film Field-Emission Cathode. *Journal of Applied Physics*, **39**(3504), 1968.

[14] R. H. Fowler and L. Nordheim. Electron Emission in Intense Electric Fields. *Proceedings of the Royal Society of London A*, **119**(173), 1928.

[15] E. L. Murphy and R. H. Good. Thermionic Emission, Field Emission, and the Transition Region. *Physical Review*, **102**(1464), 1956.

[16] R. Stratton. Field Emission from Semiconductors. *Proceedings of the Physical Society B*, **68**(746), 1955.

[17] R. Stratton. Theory of Field Emission from Semiconductors. *Physical Review*, **125**(67), 1962.

[18] J. W. Gadzuk and E. W. Plummer. Field Emission Energy Distribution. *Reviews of Modern Physics*, **45**(487), 1973.

[19] J. W. Gadzuk. Single-atom point source for electrons: Field-emission resonance tunneling in scanning tunneling microscopy. *Physical Review B*, **47**(19), 1992.

[20] W. P. Kang, J. L. Davidson, M. Howell, B. Bhuva, D. L. Kinser, D. V. Kerns, Q. Li, and J. F. Xu. Micropatterned polycrystalline diamond field emitter vacuum diode arrays. *Journal of Vacuum Science and Technology B*, **14**(2068), 1996.

[21] J. Lewellen. private communication.

[22] J. W. Lewellen and J. Noonen. Field-emission cathode gating for rf electron guns. *Physical Review Special Topics - Acelerators and Beams*, **8**(033502), 2005.

[23] J. Lewellen. private communication.

[24] K.-N. Tu, J. W. Mayer, and L. C. Feldman. *Electronic Thin Film Science For Electrical Engineers and Material Scientist*. Macmillian, New York, 1992, (101).

[25] K. L. Jensen, P. Mukhopadhyay-Phillips, E. G. Zaidman, K. Nguyen, M. A. Kodis, L. Malsawma, and C. Hor. Electron emission from a single spindt-type field emitter: Comparison of theory with experiment. *Appl. Surf. Sci.*, **111**:204–212, 1997.

[26] P. R. Schwoebel, C. A. Spindt, and C. E. Holland. Spindt cathode tip processing to enhance emission stability and high-current performance. *J. Vac. Sci. Technol. B*, **21**(1):433–435, 2003.

[27] P. R. Schwoebel, C. A. Spindt, and C. E. Holland. High current, high current density field emitter array cathodes. *J. Vac. Sci. Technol. B*, **23**(2):691–693, 2005.

[28] A. Wisitsora-at, W. P. Kang, J. L. Davidson, M. Howell, and D. V. Kerns. Gated Diamond Field Emitter Array with Ultra Low Operating Voltage and High Emission Current. *Conference Digest - IEEE Device Research Conference*, pages 150–151, 1997.

[29] K. A Dean, T. P Burgin, and B. R. Chalamala. Evaporation of carbon nanotubes during electron field emission. *Appl. Phys. Lett.*, **79**(12):1873–1875, 2001.

[30] M. S. Wang, L.-M. Peng, J. Y. Wang, and Q. Chen. Electron Field Emission Characteristics and Field Evaporation of a Single Carbon Nanotube. *J. Phys. Chem. B*, **109**:110–113, 2005.

[31] M. Doytcheva, M. Kaiser, and N. de Jonge. In situ transmission electron microscopy investigation of the structural changes in carbon nanotubes during electron emission at high currents. *Nanotechnology*, **17**:3226–3233, 2006.

[32] Y. M. Wong. unpublished work.

[33] M. Reiser. *Theory and Design of Charged Particle Beams*. Wiley, New York, 1994.

[34] J. B. Rosenzweig. *Fundamentals of beam physics*. Oxford, New York, 2003.

[35] C. A. Brau. What Brightness Means. Proceedings of the ICFA Workshop: The Physics and Applications of High Brightness Electron Beams, 2002.

[36] T. Wade and N. Tolk. private communication.

[37] Y. Cui, Y. Zou, A. Valfells, M. Reiser, M. Walter, I. Haber, R. A. Kishek, S. Bernal, and P. G. O'Shea. Design and operation of a retarding field energy analyzer with variable focusing for space-charge-dominated electron beams . *Review of Scientific Instruments*, **75**(2736), 2004.

[38] R. Reifenberger, H. A. Goldberg, and M. J. G. Lee. Measurement of the total energy distribution in photo-induced field emission. *Surface Science*, **83**(599), 1979.

[39] N. D. Land, A. Yacoby, and Y. Imry. Theory of a single-atom point source for electrons. *Physical Review Letters*, **63**(1499), 1989.

[40] P. W. Hawkes and E. Kasper. *Principles of Electron Optics, Volume 2*. Academic, London, 1994.

[41] M. J. Fransen, Th. L. van Rooy, and P. Kruit. Field emission energy distributions from individual multiwalled carbon nanotubes. *Applied Surface Science*, **146**(312), 1999.

[42] O. Groning, O. M. Kottel, P. Groning, and L. Schlapbach. Field emitted electron energy distribution from nitrogen-containing diamondlike carbon. *Applied Physics Letters*, **71**(16), 1997.

[43] S. J. Smith and E. M. Purcell. Visible Light from Localized Surface Charges Moving across a Grating. *Phys. Rev.*, **92**(1069), 1953.

[44] G. T. di Francia. On the theory of some Cerenkovian effects. *Nuovo Cimento*, **16**(61), 1960.

[45] P. M. van den Berg. Smith-Purcell radiation from a line charge moving parallel to a reflection grating. *Journal of the Optical Society of America*, **63**(689), 1973.

[46] P. M. van den Berg. Smith-Purcell radiation from a point charge moving parallel to a reflection grating. *Journal of the Optical Society of America*, **63**(1588), 1973.

[47] O. Haeberle, P. Rullhusen, J.-M. Salome, and N. Maene. Calculations of Smith-Purcell radiation generated by electrons of 1100 MeV. *Physical Review E*, **49**(3340), 1994.

[48] L. Schaechter. *Beam-Wave Interaction in Periodic and Quasi-Periodic Structures*. Springer-Verlag, Berlin, 1996.

[49] Y. Shibata, S. Hasebe, K. Ishi, S. Ono, M. Ikezawa, T. Nakazato, M. Oyamada, S. Urasawa, T. Takahashi, T. Matsuyama, K. Kobayashi, and Y. Fujita. Coherent Smith-Purcell radiation in the millimeter-wave region from a short-bunch beam of relativistic electrons. *Physical Review E*, **57**(1061), 1998.

[50] A. S. Kesar, M. Hess, S. E. Korbly, and R. J. Temkin. Time- and frequency-domain models for Smith-Purcell radiation from a two-dimensional charge moving above a finite length grating. *Physical Review E*, **71**(016501), 2005.

[51] A. S. Kesar. Smith-Purcell radiation from a charge moving above a finite-length grating. *Physical Review Special Topics - Accelerators and Beams*, **8**(072801), 2005.

[52] H. L. Andrews, C. H. Boulware, C. A. Brau, and J. D. Jarvis. Superradiant emission of Smith-Purcell radiation. *Phys. Rev. ST Accel. Beams*, **8**(110702), 2005.

[53] D. Li, K. Imasaki, Z. Yang, G.-S. Park, S. Miyamoto, S. Amano, and T. Mochizuki. SmithPurcell Radiation with Three-Dimensional Simulation. *Japanese Journal of Applied Physics*, **46**(601), 2007.

[54] C. A. Brau. *Modern Problems in Classical Electrodynamics*. Oxford, New York, 2004, (490).

[55] P. M. van den Berg and T. H. Tan. Smith-Purcell radiation from a line charge moving parallel to a reflection grating with rectangular profile. *J. Opt. Soc. Am.*, **64**(325), 1974.

[56] O. H. Kapp, Y.-e Sun, K.-J Kim, and A. V. Crewe. Modification of a scanning electron microscope to produce Smith-Purcell radiation. *Rev. Sci. Instrum.*, **75**(11), 2004.

[57] A. Bakhtyari, J. E. Walsh, and J. H. Brownell. Amplified-spontaneous-emission power oscillation in a beam-wave interaction. *Phys. Rev. E*, **65**(066503), 2002.

[58] J. R. Pierce. Theory of the beam-type traveling-wave tube. Proceedings of the IRE, 1947. **35**.

[59] J. R. Pierce. *Traveling-Wave Tubes*. D. Van Nostrand Company, New York, 1950.

[60] P. Guenard, O. Doehler, B. Epsztein, and R. Warnecke. New oscillator tubes with wide electronic tuning range. *Comptes Rendus Acad. Sci. (Paris)*, **235**(p. 236), 1952.

[61] R. Kompfner and N. T. Williams. Backward-wave tubes. *Proc. IRE*, **41**(p. 1602), 1953.

[62] H. Heffner. Analysis of the Backward-Wave Traveling-Wave Tube. Technical Report Elec. Res. Lab. Rep. No. 48, Stanford University, Stanford, California, June 1952.

[63] H. L. Andrews and C. A. Brau. Gain of a Smith-Purcell free-electron laser. *Phys. Rev. ST Accel. Beams*, **7**(070701), 2004.

[64] H. L. Andrews, C. H. Boulware, C. A. Brau, and J. D. Jarvis. Dispersion and attenuation in a Smith-Purcell free-electron laser. *Phys. Rev. ST Accel. Beams*, **8**(050703), 2005.

[65] H. L. Andrews, C. H. Boulware, C. A. Brau, J. T. Donohue, J. Gardelle, and J. D. Jarvis. Effect of reflections and losses in Smith-Purcell free-electron lasers. *New J. Phys.*, **8**(289), 2006.

[66] V. Kumar and K.-J Kim. Analysis of Smith-Purcell free-electron lasers. *Phys. Rev. E*, **73**(026501), 2006.

[67] J. T. Donohue and J. Gardelle. Simulation of Smith-Purcell radiation using a particle-in-cell code. *Phys. Rev. ST Accel. Beams*, **8**(060702), 2005.

[68] D. Li, Z. Yang, K. Imasaki, and G.-S Park. Particle-in-cell simulation of coherent and superradiant Smith-Purcell radiation. *Phys. Rev. ST-AB*, **9**(040701), 2006.

[69] D. Li, K. Imasaki, X. Gao, Z. Yang, and G.-S Park. Reduce the start current of Smith-Purcell backward wave oscillator by sidewall grating. *Appl. Phys. Lett.*, **91**(221506), 2007.

[70] J. D. Jarvis and H. L. Andrews. Three-dimensional theory of the Smith-Purcell free-electron laser. Proceedings of the International FEL conference, Novosibirsk, Russia. 2007.

[71] J. D. Jarvis, H. L. Andrews, and C. A. Brau. Three-dimensional, small-signal theory of the Smith-Purcell free-electron laser. submitted to Physical Review Special Topics - Accelerators and Beams.

[72] H. L. Andrews, J. D. Jarvis, and C. A. Brau. Three-dimensional theory of the SmithPurcell free-electron laser with side walls. *Journal of Applied Physics*, **105**(024904), 2009.

[73] H. L. Andrews and C. A. Brau. Three-dimensional theory of the Cerenkov free-electron laser. *Journal of Applied Physics*, **101**(104904), 2007.

[74] G. F. Mkrtchian. Small signal gain of a Smith-Purcell free electron laser. *Physical Review Special Topics - Accelerators and Beams*, **10**(080701), 2007.

[75] J. D. Jackson. *Classical Electrodynamics, third edition*. Wiley, New York, 1999, (358).

[76] C. A. Brau. *Modern Problems in Classical Electrodynamics*. Oxford University Press, New York, 2004, (345).

[77] I. J. Owens and J. H. Brownell. Compact superradiant Cerenkov source. *Journal of Applied Physics*, **97**(104915), 2005.

[78] B. Choi. private communication.

[79] E. Heeres. private communication.

[80] K. Varga and J. Driscoll. unpublished work.